

Scholar@UPRM

Synthesis and characterization of calcium sulfide nanoparticles

| | |
|---------------|---|
| Item Type | Dissertation |
| Authors | Rivera Vázquez, Daniel |
| Download date | 2026-06-10 12:20:25 |
| Link to Item | https://hdl.handle.net/20.500.11801/3812 |

Synthesis and Characterization of Calcium Sulfide Nanoparticles

By

Daniel Rivera Vázquez

A dissertation submitted in partial fulfillment of the requirements for the degree of

DOCTOR OF PHILOSOPHY

in

Applied Chemistry

UNIVERSITY OF PUERTO RICO

MAYAGUEZ CAMPUS

2014

Approved by:

Mayra E. Cádiz, Ph.D
Member, Graduate Committee

Date

Alberto Santana, Ph.D
Member, Graduate Committee

Date

Oswald N.C. Uwakweh, Ph.D
Member, Graduate Committee

Date

Miguel E. Castro-Rosario, Ph.D
President, Graduate Committee

Date

Gustavo Gutiérrez, Ph.D
Representative of Graduate Studies

Date

Aidalú Joubert Castro, Ph.D
Chairperson of the Department

Date

Abstract

Calcium sulfide (CaS) nanoparticles are cadmium free fluorescent nanostructures with potential applications in nanomedicine and as a sensing material. We employed different methods for the synthesis of CaS nanoparticles, including (1) the reaction of calcium acetate ($\text{Ca}(\text{CH}_3\text{CO}_2)_2$) and sodium sulfide (Na_2S) in dimethyl sulfoxide (DMSO), (2) the reaction of $\text{Ca}(\text{CH}_3\text{CO}_2)_2$ and DMSO in a microwave and (3) dissolving bulk quantities of CaS in DMSO. UV-Vis spectroscopy was used to determine the optical properties of the CaS nanostructures. The absorption spectra of CaS prepared from these methods consists of a well-defined peak in the UV and a long wavelength tail that extends above 700 nm. Emission bands centered around 500 nm with a long wavelength tail that extends above 600 nm are observed upon excitation at 405 nm. Scanning tunneling microscopy (STM) was used for determining the average diameter of CaS nanostructures of (3.3 ± 0.7) nm. The direct and indirect band gaps are estimated to be (0.403 ± 0.003) eV and (4.135 ± 0.006) eV.

Configuration interaction singles (CIS) calculations were used to determine the electronic transition spectra of small CaS clusters. Unique to CaS nanostructures is the absorption of light at wavelengths longer than in the bulk material instead of the blue shift associated with quantum confinement effects in semiconductors. Indeed, the strong absorption bands in the visible region of the spectra of the CaS nanostructures do not have a counterpart in the gas or solid phases, with implications in the field of sensing using semiconducting nanoparticles. Density functional theory (DFT) calculations on small CaS clusters are used to establish the vibrational properties of calcium sulfide nanoclusters.

Naked CaS nanostructures are found to limit the survival rate and inhibit the growth rate of carcinoma cancer cell lines (ATCC CRL-2124). A single dose of a dispersion containing (3.3 ± 0.7) nm CaS nanoparticles (total calcium content of 3.8×10^{-8} moles) results in a sharp decrease in the density of live cells and a sharp increase in the number of dead cells 96 hours following the dose. No changes are observed in adenocarcinoma control cell lines. CaS do not have any effect on the survival and growth rate of normal fibroblasts as compared to control cell cultures of normal fibroblasts, which suggests that CaS nanostructures are cancer specific. The small size of the nanostructures allows them to have access to the normal and newly developed blood vessels-due to angiogenesis and elimination by the human body. The results encourage further

research to establish the mechanisms of action of CaS in cancer cell cultures and laboratory animals.

Resumen

Las nanopartículas de sulfuro de calcio (CaS) son nanoestructuras fluorescentes con posibles aplicaciones en el campo de la nanomedicina y como biosensores. Hemos empleado distintos métodos para la síntesis de nanopartículas de CaS que incluyen: (1) la reacción de acetato de calcio ($\text{Ca}(\text{CH}_3\text{CO}_2)_2$) con sulfuro de sodio (Na_2S) en sulfóxido de dimetilo (DMSO), (2) la reacción de $\text{Ca}(\text{CH}_3\text{CO}_2)_2$ y DMSO en un microondas y (3) disolviendo cantidades macroscópicas de CaS en DMSO. Se utilizó espectroscopía UV-Vis para determinar las propiedades ópticas de las nanoestructuras de CaS. Los espectros de absorción de CaS preparado utilizando los métodos descritos anteriormente consisten de un pico bien definido en la región del UV y una “cola” que se extiende a largos de onda mayores de 700 nm. Se observaron bandas de emisión centradas cerca de los 500 nm con una “cola” que se extiende a largos de onda mayores de 600 nm al excitar en 405 nm. Se utilizó microscopía de rastreo por tunelaje (STM, por sus siglas en inglés) para determinar el diámetro promedio de las nanoestructuras de CaS. Se estimaron las brechas energéticas directas e indirectas en (0.403 ± 0.003) eV y (4.135 ± 0.006) eV, respectivamente.

Se utilizaron cálculos utilizando interacción de configuración sencilla (CIS, por sus siglas en inglés) para determinar los espectros de transiciones electrónicas en pequeñas aglomeraciones. La absorción de luz a largos de ondas mayores a los del grueso del material, en lugar del desplazamiento hacia el azul asociado a efectos de confinamiento cuántico en semiconductores es único de las nanoestructuras de CaS. En efecto, las bandas de absorción en la región visible de los espectros de nanoestructuras de CaS no tienen contraparte en las fases gaseosas o sólidas. Se utilizaron, además, cálculos de teoría de funcional de densidad (DFT, por sus siglas en inglés) en pequeños agregados de CaS para establecer las propiedades vibracionales de los nanoagregados de sulfuro de calcio.

Hemos encontrado que nanoestructuras de CaS limitan la supervivencia e inhibe la razón de crecimiento de líneas celulares cancerosas de adenocarcinoma (ATCC CRL-2124). Una sola dosis de una dispersión que contiene nanopartículas con un diámetro de (3.3 ± 0.7) nm (contenido total de calcio 3.8×10^{-8} moles) resulta en una disminución pronunciada en la densidad de células vivas y un aumento agudo en el número de células muertas luego de 96 horas de la dosificación. No se observan cambios en las líneas celulares de adenocarcinoma control.

CaS no tiene efectos en la supervivencia y razón de crecimiento de fibroblastos normales en comparación con líneas celulares de adenocarcinoma tipo control, lo cual sugiere que las nanoestructuras de CaS son específicas a cáncer. El diminuto tamaño de las nanoestructuras les permite acceso a vasos sanguíneos normales y recién formados debido a angiogénesis y eliminación por el cuerpo humano. Estos resultados son alentadores para seguir investigación con el fin de establecer los mecanismos de acción de CaS en cultivos de células cancerígenas y en animales de laboratorio.

© 2014 Daniel Rivera Vázquez

I dedicate this work to a person that has always loved and supported me. This person has witnessed the ups and downs and has always fought beside me to make this possible. Her selflessness and pursuit of perfection has always been an inspiration for me to strive to become a better researcher as well as a better person. I dedicate this work to my loving wife, Yohaselly Santiago-Rodríguez, because without her, this work would not have been possible.

Acknowledgements

I wish to thank:

My loving wife Yohaselly Santiago-Rodríguez.

My loving parents, Iris Vázquez and Félix Quiñones; my brothers Félix and Leonel, my sister Denisse and her husband Alfredo; my niece “kikin” and my nephews “junior” and “naldi”. My grandparents Edith and Felix; thank you all for your love and support.

My lab partner and friend Miguel A. González

My friends and colleagues: Edmy, Madeline, Tamara, Ramonita, Darya, Bessie, Wanda, José and all others who, in one way or another, have helped me through my graduate studies.

My advisor Dr. Miguel E. Castro-Rosario and my thesis committee members: Dr. Mayra E. Cádiz, Dr. Alberto Santana and Dr. Oswald N.C. Uwakweh.

Dr. Edu B. Suárez for her mentoring during my internship at UPR- Ponce campus

Dr. Juan López-Garriga, for the use of lab facilities.

RISE-2-BEST program for their financial support and the many opportunities to advance my research to the next level.

Alfred P. Sloan foundation for their financial support.

TABLE OF CONTENTS

| Content | Page number |
|--|-------------|
| Abstract | ii |
| Resumen | iv |
| Acknowledgements | viii |
| Table of Contents | ix |
| Figure List | x |
| Table List | xiv |
| Scheme List | xv |
| Chapter I: Introduction | 1 |
| 1.1 References | 18 |
| Chapter II: Objectives | 21 |
| Chapter III: Synthesis and characterization of calcium sulfide nanoparticles: towards the development of cadmium free fluorescent nanostructures | 22 |
| 3.1 References | 36 |
| Chapter IV: Nucleation and growth process in calcium sulfide: towards the understanding of the stability of small aggregates | 39 |
| 4.1 References | 56 |
| Chapter V: Quantum Confinement Effects in Calcium Sulfide: The Role of Indirect Transitions in the Red Shift of the Band Edge in Semiconductor Nanoparticles | 57 |
| 5.1 References | 66 |
| Chapter VI: Effect of CaS nanostructures on the proliferation rate of human adenocarcinoma cells <i>in vitro</i> | 67 |
| 6.1 References | 93 |
| Chapter VII: Conclusions and Outlook | 97 |

Figure List

| Figure | | Page |
|--------|---|------|
| 1.1 | (a) Particle-in-a-box (PIB) one dimensional model, in which a hypothetical particle is confined between two barriers of infinite potential energy. In three dimensions, this model explains quantum confinement, where the electron can be excited within the particle to higher levels, but a physical barrier confines the electron. Solutions to the PIB model can be attained for particles with different shapes, for example (b) cubical model using Cartesian coordinates or spherical coordinates for a sphere shaped particle (c). | 2 |
| 1.2 | (left) model of an electronic transition of a “pure” material, from the valence into the conduction band, and subsequent relaxation process through the emission of energy of wavelength λ' . (Right) When imperfections are present, the excitation occurs from the valence into the conduction band, and electrons fall into the so called “trap states” involving the release of lower wavelength energies λ'' , λ''' and so on. | 4 |
| 1.3 | Schematic representation of CaS nanoparticle formation according to nucleation and growth theory. | 8 |
| 1.4 | Relative sizes of the most common cancer nanotechnologies. | 13 |
| 3.1 | The solid and dense dots represent the absorbance and fluorescence spectra, respectively, of (a) sample prepared by dissolving bulk CaS in DMSO, (b) a mixture of solutions of $\text{Ca}(\text{CH}_3\text{CO}_2)_2$ and Na_2S in DMSO and (c) the product of the microwave mediated reaction of $\text{Ca}(\text{CH}_3\text{CO}_2)_2$ with DMSO. | 28 |
| 3.2 | The left and right hand side represent selected STM images of independent measurements of $100 \times 100 \text{ nm}^2$ and $50 \times 50 \text{ nm}^2$ regions of a deposit of CaS on MoS_2 , respectively. The particle size distribution obtained from the analysis of three independent scans and height of a selected scan line are displayed on the bottom of the figure. | 30 |

| | | |
|-----|---|----|
| 3.3 | The absorption spectra of dispersions CaS prepared with the indicated initial warmed in the microwave on initial $\text{Ca}(\text{CH}_3\text{CO}_2)_2$ /DMSO mole ratio. The dependence of the onset of light absorption and a picture of the samples are indicated on the lower part of the figure. The numbers in the sample's picture corresponds to the initial $[\text{Ca}(\text{CH}_3\text{CO}_2)_2]/[\text{DMSO}]$ concentration ratio indicated from bottom to top in the figure. | 32 |
| 3.4 | The fluorescence spectra of various solutions of CaS prepared from the microwave mediated reaction between $\text{Ca}(\text{CH}_3\text{CO}_2)_2$ and DMSO as a function of the relative initial CaS concentration. The open and closed circles in the bottom panel of represent the dependence of the absorbance at 405 nm and the fluorescence peak area on the $[\text{CaS}]$ relative concentration, respectively. The insert is a plot of the fluorescence peak area as a function of the amount of light absorbed at 405 nm by each sample in the dilution sequence. | 33 |
| 4.1 | Absorption spectrum of $\text{Ca}(\text{CH}_3\text{CO}_2)_2$ in DMSO ratio of 10^{-3} to different exposure times of microwave radiation. | 42 |
| 4.2 | The upper and lower panel are the calculated absorptions spectra of CaS monomers in the gas phase and DMSO between 190 and 1500 nm, respectively. The insert is the absorption spectrum of a dispersion with a $\text{Ca}(\text{CH}_3\text{CO}_2)_2$ to DMSO ratio of 3×10^{-4} . | 47 |
| 4.3 | Energy level diagram of the occupied and empty orbitals of CaS. The π and σ orbitals are indicated on the right hand side of the figure. | 49 |
| 4.4 | Absorption spectra between 190 and 2000 nm of optimized $(\text{CaS})_n$, with $1 \leq n \leq 5$, clusters. | 51 |
| 4.5 | Results of theoretical calculation for a CaS clusters in the gas phase. (a) Cluster energy as a function of aggregate number for $(\text{CaS})_n$, on the insert we can see the binding energy for $(\text{CaS})_n$ as a function of aggregate number. (b) Change in energy as a function of aggregate number for $(\text{CaS})_n$. | 54 |
| 4.6 | Gibbs free energy to form calcium sulfide clusters by the stepwise addition of monomers as a function of aggregation number. The insert represents the Gibbs free energy change associated with a nucleation process as a function of phase or particle size. See text for details. | 56 |

| | | |
|-----|---|----|
| 5.1 | a) A representative $50 \times 50 \text{ nm}^2$ STM image of a CaS NP deposit with a $[\text{Ca}]/[\text{DMSO}]$ ratio of 1×10^{-4} is displayed on figure 1a. The particles are $(3.2 \pm 0.7) \text{ nm}$. (b) A clear solution (left side) is obtained when $\text{Ca}(\text{CH}_3\text{CO}_2)_2$ is dissolved in DMSO, and it turns into an orange dispersion when warmed in the microwave for a total of 75 seconds (right side).(c) Absorption spectrum of CaS solution. | 60 |
| 5.2 | Plots of $(\text{AE}_0)^{1/2}$ and $(\text{AE}_0)^2$ as a function of incident photon energy, deduced from the absorption spectrum of the dispersion prepared by dissolving solid CaS in 10 mL of DMSO at room temperature. | 63 |
| 5.3 | Optimized structure of a cube of CaS containing 4 monomers, with a “breathing” mode deformation. | 64 |
| 6.1 | (a) UV-visible spectra of CaS nanostructures prepared from the microwave mediated decomposition of DMSO in the presence of $\text{Ca}(\text{CH}_3\text{CO}_2)_2$. The Ca^{2+} to DMSO ratios are 2 and 6×10^{-4} . (b) Absorption and emission spectra of CaS prepared from the double ion exchange reaction in DMSO (top), dissolution of bulk CaS in DMSO (middle) and microwave decomposition of $\text{Ca}(\text{CH}_3\text{CO}_2)_2$ in DMSO (bottom). Representative STM images of CaS deposits prepared from the microwave mediated decomposition of DMSO in the presence of $\text{Ca}(\text{CH}_3\text{CO}_2)_2$ with Ca^{2+} to DMSO ratios of (c) 2 and (d) 6×10^{-4} . (e) CaS particle size distribution obtained from image (d). | 75 |
| 6.2 | Images of adenocarcinoma cells obtained (a) 24 hours after inoculation, (b) the control 96 hours after preparing the culture and (c) 96 hours after adding a single dose of 4.0×10^{-8} moles of Ca^{2+} in the form of CaS NP. Representative image of adenocarcinoma cells 48 hours following a CaS dose of 1.6×10^{-7} moles is indicated on the bottom of the figure. | 77 |
| 6.3 | The open squares and circles represent the dependence of carcinoma cell density fed with normal media and media mixed with 4.0×10^{-8} moles of Ca^{2+} in the form of CaS monomers and clusters, respectively, on time. | 79 |

- 6.4 The density of adenocarcinoma cells following a single dose of 4.0×10^{-8} moles of Ca^{2+} in the form of CaS NP (S_1 , S_2 , S_3) and controls (C_1 and C_2). The error bars represent the standard deviation of the measurements. The individual measurements performed are indicated in the insert on the upper right corner of each graph. 81
- 6.5 The gray bars in the upper and lower panel summarize the effect of a single dose of 3.8×10^{-8} moles of Ca^{2+} in the form of CaS NP on the density of carcinoma cells and the number of dead carcinoma cells, respectively, as a function of time. The light gray bars in the upper and lower panel represent the density of adenocarcinoma cells and number of dead carcinoma cells in cell cultures fed with media not containing the CaS nanostructures, respectively. The values reported represent the average of 15 measurements performed on different regions of three different flasks. The error bars represent the standard error of the measurements. The dark and light gray bars in the insert represent the dependence of the density of adenocarcinoma cells exposed to a second dose of 3.8×10^{-8} moles of Ca^{2+} in the form of CaS NP and exposed to one dose, respectively, on time. 84
- 6.6 The closed squares and circles represent the dependence of normal fibroblasts cell density fed with normal media and media mixed with 4.0×10^{-8} moles of Ca^{2+} in the form of CaS monomers and clusters, respectively. The insert in the right hand side of the lower panel represents the spectrum of the dispersion containing the CaS nanostructures used for the measurements. 85

Table List

| Table | | Page |
|-------|---|-------|
| 1.1 | Most common forms of nanotechnology employed on cancer research, basic description and their role in cancer therapeutics, sensing or drug delivery. | 12 |
| 4.1 | Results of the geometry optimization, energy, frequency, dipole moment and percent ionic character calculated for the gas phase monomer using several functional and basis set combinations. | 44 |
| 5.1 | Sum of the vibrational frequencies of all the modes found in the optimized structures of several CaS nanoclusters with aggregate number $1 \leq n \leq 5$. | 65 |
| 6.1 | Optimized structures and interaction energies of CaS with several functional groups of interest in a cell. The smaller CaS to functional group minimum distance and Ca-S bond length are also indicated on the table. | 87-89 |
| 6.2 | Values of α obtained from that best fit to the experimental measurements on the proliferation of adenocarcinoma cells and normal fibroblasts according to a power model in time. | 91 |
| 6.3 | Standard Gibbs energy (ΔG_f°) of formation of probable species containing calcium and sulfide in aqueous solution. | 92 |

Scheme List

| Scheme | | Page |
|--------|---|------|
| 1.1 | (a) Simplified scheme of extrinsic mechanism of apoptosis. Also known as cell surface or type I mechanism. Involves ① the activation of tumor necrosis factor (TNF) family receptors, ② activating caspases in the cell, which leads to ③ cell death by apoptosis. (b) Simplified scheme of Intrinsic mechanism. Also known as mitochondrial or type II mechanism. Involves ① the stimulation of the mitochondria to ② release cytochrome c into the cytoplasm, which triggers ③ the activation of caspases, leading to ④ cell death by apoptosis. ②' Inactivation of anti-apoptosis proteins by direct binding may also lead to apoptosis. | 16 |
| 3.1 | CaS nanostructures are prepared by various methods including (1) the reaction of $\text{Ca}(\text{CH}_3\text{CO}_2)_2$ and Na_2S in DMSO, (2) the reaction of $\text{Ca}(\text{CH}_3\text{CO}_2)_2$ and DMSO in a microwave and (3) dissolving bulk quantities of CaS in DMSO. The particles are found to emit light at 500 nm following excitation at 400 nm. | 25 |

Chapter I

Introduction

A nanostructure (NS) is defined by Kittel as “a solid confined in either two or three orthogonal directions, creating effectively one dimensional (1D) or zero dimensional (0D) structures”.¹ Some examples of 1D nanostructures are nanotubes and nanowires, and for 0D some examples include semiconducting nanocrystals (quantum dots) and nanoparticles. Both 1D and 0D materials have been studied for applications in many fields including sensors^{2,3} and for biomedical sciences⁴⁻⁶, photocatalysis, environmental and drug development among other areas. Indeed, the research of nanomaterials has yielded the knowledge and technology to develop tailored materials for specific needs.

In the field of biosensors, quantum dots have been researched extensively resulting in many advances in the field.^{7,8} A biosensor is defined as a device that uses a chemical or biological receptor for the detection of analytes in a sample.⁹ They play an important role in the study of biological systems because we can obtain information such as the selectivity, affinity, kinetics and thermodynamics of the reactions occurring in such systems. Quantum dots (QD) are, by definition, semiconducting nanoparticles with no dimension larger than 10 nm. They offer several advantages such as narrow wavelength emission and high intensity. In this scale, quantum mechanical behavior dominates the physical and chemical properties of the material. Specifically, the optical properties of the nanomaterial change as a function of their size. As the size of the nanoparticle decreases, the energy involved in electronic transition shift into higher levels and the number of oscillations decreases. This phenomenon is known as quantum

confinement and is responsible for several applications of nanoparticles such as luminescence-based biosensors and photovoltaic cell components.^{10,11}

To understand the quantum confinement effect, let us consider an electron confined to two barriers of infinite potential as shown in Figure 1.1. This is known as the particle in a box (PIB) model.

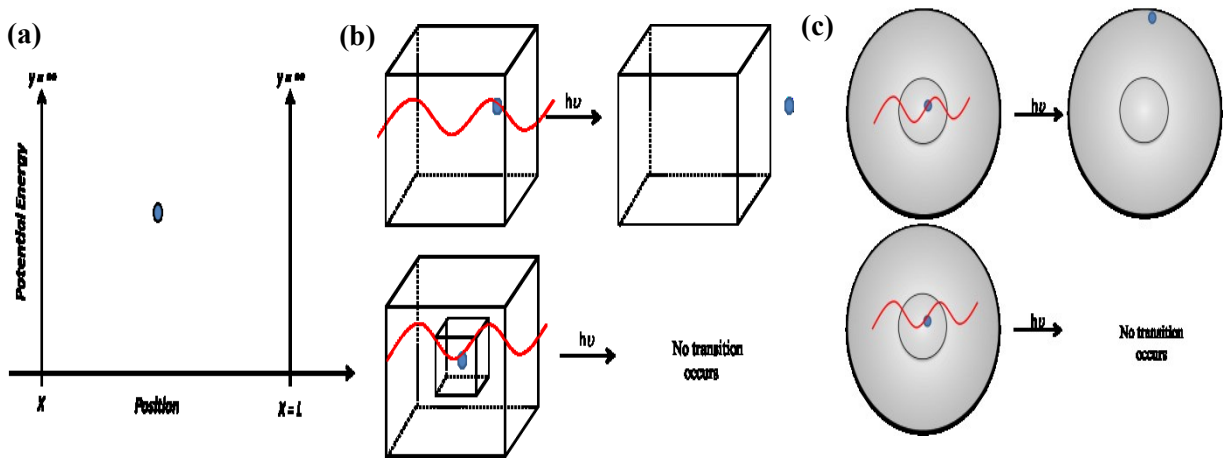


Figure 1.1: (a) Particle-in-a-box (PIB) one dimensional model, in which a hypothetical particle is confined between two barriers of infinite potential energy. In three dimensions, this model explains quantum confinement, where the electron can be excited within the particle to higher levels, but a physical barrier confines the electron. Solutions to the PIB model can be attained for particles with different shapes, for example (b) cubical model using Cartesian coordinates or spherical for a sphere shaped particle (c). It is important to note that quantum mechanical effects occur when the de Broglie wavelength of the electron is of the same order of magnitude as the wavelength of the particle itself. This occurs in 0D materials, resulting in the physical phenomena described above.

The solution of this model in one dimension results in discrete energy levels for the electron. This is a general result of quantum mechanics: confinement of an electron results in the formation of discrete energy levels. These discrete energy levels are not observed in a free electron because no restrictions are imposed on it. Nanostructures are generally formed experimentally in three dimensions, in which the PIB model also impose quantum confinement

effects and limits the number of electronic transitions. The model is described in this dissertation in further detail in chapter V. Quantum confinement effects have been used to explain several physical phenomena that occur in quantum dots, including shifts in light absorption and emission. The smaller number of atoms required to build up a nanostructure results in a reduction in the total number of electrons – as compared to bulk material – and a reduction in the number of electronic transitions in the UV-Vis and NIR region of the electromagnetic spectrum. Light absorption and emission by quantum dots of a given material is size dependent. Luminescent biosensors can be developed for several wavelengths with the same material synthesized at different sizes. This facilitates the use of this materials as biosensors and photovoltaic components. Fine tuning quantum dots to absorb and emit radiation of different wavelengths is accomplished by controlling the particle size, which in turn is a function of the experimental conditions employed.

Light emission results from the relaxation of excited electrons to levels of lower energy. In QD, this process results from relaxation of excited electrons from the conduction to the valence band. A second phenomenon which affects the wavelength at which relaxation processes occurs is when the materials has a non-uniform morphology or in the presence of impurities. Impurities in a semiconductor nanoparticle gives rise to new bonding states. These new states at which the electron relaxes are collectively known as “new trap states”. Trap states are also possible when a new molecule bonds with the material, presenting a new set of vacant orbitals for the excited electrons to fall into. This can be used as a qualitative parameter for the affinity of a semiconducting nanoparticle with an exogenous agent. The process is described in Figure 1.2.

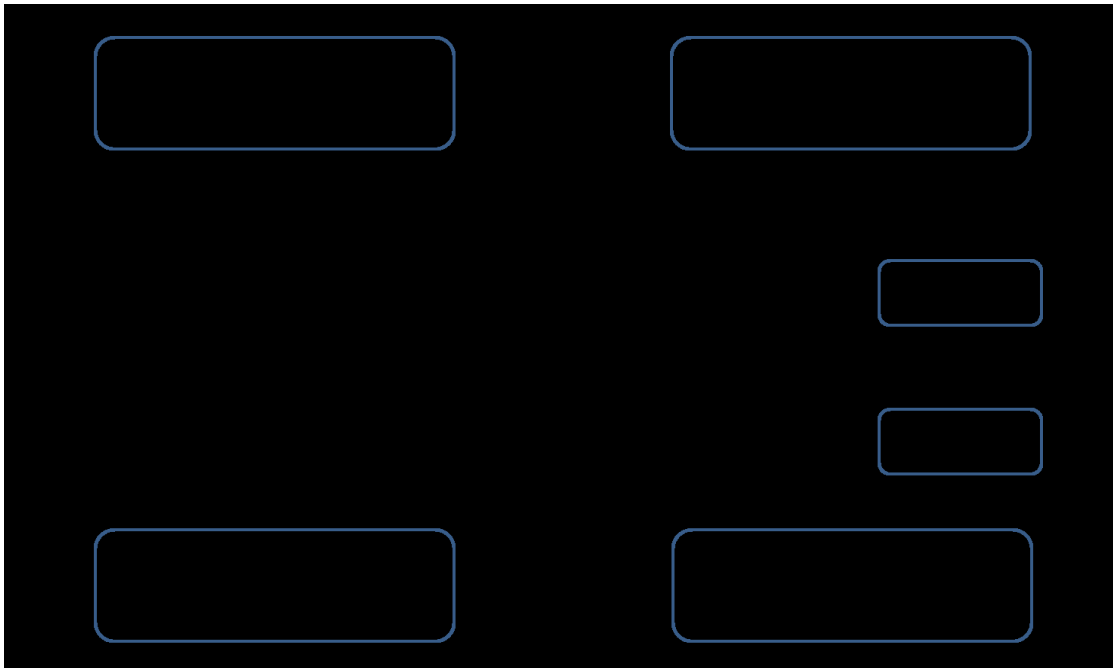


Figure 1.2: (left) model of an electronic transition of a “pure” material, from the valence into the conduction band, and subsequent relaxation process through the emission of energy of wavelength λ' . (Right) When imperfections are present, the excitation occurs from the valence into the conduction band, and electrons fall into the so called “trap states” involving the release of lower wavelength energies λ'' , λ''' and so on.

QD are commonly referred to as zero dimensional (0D) materials due to the small size required to reach and maintain quantum confinement effects. There are several commonly used methods for the synthesis of 0D materials, including sonochemical¹², chemical reactions and hydrothermal.^{4,8,13} In a review by Gosh several different conventional synthesis methods are explained and compared against each other in detailed, including the methods described above.¹⁴ The author also mentions the different classifications of quantum dots based on their composition. Some examples include core/shell nanostructures, inorganic, organic and rare earth based quantum dots. Other parameters which are very important to control are reaction temperature, pH and precursor concentration. However, there are several limitations, such as preparation time, purity of the quantum dots and the cost of preparation, for these methods which

hinder their effectiveness. Other non-conventional methods have gained popularity in the field of quantum dot synthesis. One such method is using microwave radiation.

Microwave assisted synthesis has been useful in creating fast, reproducible nanomaterials with high purity. This synthesis method offers the advantage that the energy input can be controlled. This is very important for the controlled synthesis of quantum dots, mainly because we would be controlling the rate of nucleation and growth, as will be explained later on. This in turn leads to the development of tailored materials of a desired size. Ferrer showed the advantage of using microwave radiation and created CdS nanoparticles of several different sizes, proportional to the energy applied to the system and initial reactant concentration.¹⁵ Microwave assisted synthesis of nanostructured materials has gained higher importance recently, as highlighted on a review by Zhu.¹⁶ He points to one of the key advantages that microwave synthesis offers over other conventional methods: it is completed in very short time periods. Where a wet method would take hours to complete, with microwave radiation the reaction time is reduced to minutes or even seconds.

The physical processes involved in nanostructure synthesis are important to understand the different approaches for nanoparticle synthesis. The process that governs the synthesis, that is to say, the size and morphology of the material, can be explained using nucleation and growth theory. Nucleation is defined as the process in which free precursor atoms or molecules rearrange themselves through a series of processes into a phase similar to the product and large enough to have the ability to grow in size irreversibly.¹⁷ This process is governed to a large extent by the difference chemical potential ($\Delta\mu$) of the molecule in solution (μ_s) and in the bulk of the crystal (μ_c), given by equation 1:

$$\Delta\mu = \mu_s - \mu_c$$

Equation 1.1

The difference in chemical potential can also be expressed as:

$$\Delta\mu = kT \ln[\textit{precursors}]_s$$

Equation 1.2

In equation 1.2, k represents the Boltzmann constant, T is the absolute temperature and $[\textit{precursors}]_s$ is the concentration of precursors in a supersaturated solution. This means that if the solution is unsaturated, dissolution occurs and there can be no formation of nuclei that can subsequently grow into nanoparticles. If, on the other hand, the solution is supersaturated, it leads to the nucleation and growth of the material. The energy necessary to form a cluster of n molecules is a difference in energy between in initial and final states, as shown by Becker and Döring in the 1930's.¹¹ This is important because it shows that there is an energy barrier that must be surpassed for the nucleation to take place, that is to say, for the precursors to aggregate into clusters, followed by the formation of stable nuclei and subsequent nanoparticles. This can be described mathematically by the following equation:

$$\Delta G = 4\pi r^2 \gamma + \frac{4}{3}\pi r^3 \Delta G_v$$

Equation 1.3

The first term in equation 1.3 represents the surface free energy, which is the surface area of the sphere (γ) times the area of the phase ($4\pi r^2$), and the second term is related to its energy, given by the free energy per unit volume ($\frac{4}{3}\pi r^3 \Delta G_v$) of the supersaturated solution minus the energy of the separate phase. This difference in free energy is the driving force for nucleation and growth. Equation 1.3 details a delicate balance between the surface energy which is always positive and the free energy per unit volume of the particle itself (ΔG_v), as described by Finney and Finke.¹² This means that the system reaches a maximum before the free energy term

dominates, leading to nucleation and growth. Once the nucleus reaches this critical radius, it will grow irreversibly to a macroscopic or bulk scale. This process can be described as homogeneous nucleation, if it occurs in the solution or heterogeneous nucleation if it occurs in at a pre-existing separate phase, such as the walls in a containers or a “seed” crystal. The process can be summarized as shown in Figure 1.3. The first steps in the process of nucleation and growth usually occur in the first few seconds after the supersaturated concentration of precursors is reached. This process is also known as spontaneous crystallization. On the other hand, nucleation and growth can also occur stepwise. In this process, the monomer is formed and forms a dimer, trimer, and so on until the crystal structure is formed. Control over this stepwise process may lead to the controlled synthesis of sub-nanometer scale nanomaterials. This is of special importance in the field of biomedical sciences where small nanostructures are needed for drug delivery, sensing and other applications in environments where traditional nanoparticles have limited use due to their size.

To study the kinetics and dynamics involved in this process, it is necessary to control the initial moment at which the reaction occurs and the flow rate of the reactants. The reaction must be monitored during the first milliseconds to capture the processes at which the reactants go through in order to reach cluster size and eventually grow to the nanoparticle scale. León studied the formation of Ag_2S by performing a kinetic study measuring the conductivity of the solution.²⁰ She found that the process involved multiple steps and that the entire process of nucleation, coalescence and growth into nanoparticles took less than 5 seconds. In a second study, she used a stopped flow mixer to measure the interactions during the first millisecond after mixing AgNO_3 and $(\text{NH}_4)_2\text{S}$, the precursor salts for the formation of Ag_2S .²¹ This study was important because it demonstrates through UV-vis spectroscopy and density functional theory

(DFT) calculations the formation of intermediate species and it records the process of nucleation and growth on a system.

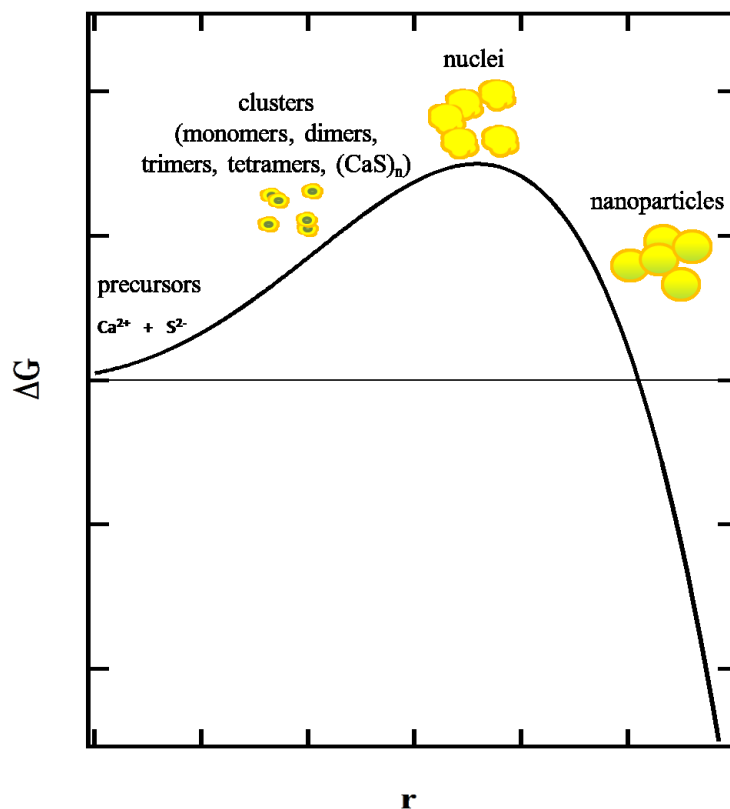


Figure 1.3: Schematic representation of CaS nanoparticle formation according to nucleation and growth theory.

In the field of biomedical sciences it is very important to control the size of quantum dots because there are several key factors that merits this degree of control. There is a need for the development of therapeutic agents whose size is too large and do not pass a threshold for renal clearing and cell diffusion, among other biological systems. In his review, Cho explains several limitations of using quantum dots for biomedical applications, including oversimplified models, inadequate applications, resulting in an overall limited predictive tool for the efficacy of the proposed materials.⁶ He described several characterization methods that differ in the results

because they are based on different physical phenomena. An example cited in his work is based on Au nanoparticles with high homogeneity and an average size of 15 nm. Using different techniques, including transmission electron microscopy (TEM), dynamic light scattering (DLS), a technique that consists of measuring the scattering effect of small particles with a monochromatic source of light, and nanoparticle tracking analysis (NTA), a technique that relates the rate of movement with temperature, viscosity of the liquid and nanoparticle size, results varied from 11 to 52 nm on average. This is very problematic when dealing with a biological system because the effective size of the nanoparticle is important for several purposes like drug delivery and for entering through a cell membrane, for example. Although he mentions several limiting factors, he also cites many other emerging technologies that are at the cutting edge of the field for biomedical applications for *in-vitro* and *in-vivo* settings.²² This work also describes 3 models for the cellular uptake and effectiveness of a nanoparticle for cellular uptake. The first model is a 2D cell model, in which a cell that grows adherent to a surface provides a 2D environment for the nanoparticles to interact. Although this is the most simple model described by Cho, it is also the one that he recommends for initial assessment of new materials with a biological system. The reason for this is because it is relatively simple to monitor cellular uptake using confocal microscopy. The second approach is using a 3D cell model. In this model, cells are exposed in 3D to nanoparticles, independent of concentration. This model also lacks the complexity that one finds on an actual biological system. The advantage is that it gives insights into the potential biological activity of the nanomaterial. The third approach is using biological activity assays. This model is the most complex, and costs more than the 2D and 3D cell model. The advantage is that it offers an approximate model that measure the activity that the nanomaterial has when interacting with a certain antigen. This model, although simple to

develop and very effective is recommended for use when success on the other two methods previously discussed is demonstrated.

A second key aspect in the development of biocompatible nanomaterials is the toxicity. One of the biggest shortcomings in using NS for biomedical applications is related to the toxicity of the materials being developed. Most first generation quantum dots were based on noble metals, such as gold and silver, and of toxic heavy metals such as cadmium and lead, elements known to be toxic in biological systems for many years. In biomedical sciences, there is a need for the improvement of biocompatible NS which can be used for different applications without toxicological effects. Different approaches have been developed and improved upon. One of the methods currently being developed consists of encapsulating the NS in a biocompatible “shell”, which either does not interact with the system under study or breaks down into pieces that can be expelled from the system with little to no adverse effects. This method is excellent for drug delivery, but has limitations because of the increased size of the shell- NS complex and because the physical properties of the nanoparticle, such as photoluminescence, may be compromised. Other physical properties that differ are not so well understood, such as its interactions in biological systems such as proteins and cells. Recently, however, there have been many important discoveries such as genetic targeted therapy²³ and the development of functionalized quantum dots for drug delivery.^{24,25}

Cancer is one of the most deadly diseases in the United States and the world. Such is the high human and economic cost of this disease that the USA has declared cancer research a top priority.²⁶ The National Institutes of Health (NIH) have an entire institute dedicated to this, the National Cancer Institute (NCI). Breast cancer is the second most common type overall and the most common in women, with a mortality rate of 17.6% and an incidence rate of around 122 per

100,000 in the United States.²⁷ Nanotechnology is playing an important role in the treatment of cancer and is currently being considered as one of the best alternatives for drug delivery, gene therapy and as a therapeutic in its own right or through functionalization, resulting in great benefit to cancer research and oncological medicine.²⁸ A comprehensive review on nanotechnologies used for cancer therapy by Misra, et. al provides insights into the stage at which this field is at this moment and the direction it is taking.²⁹ He discusses the most common forms and compositions of nanomaterials, which cover a vast array. The nanotechnologies employed can be classified as liposomes, nanoparticles, polymeric micelles, dendrimers, nanocantilevers, carbon nanotubes and quantum dots. The most common applications for these materials vary, with liposomes, dendrimers and polymeric micelles usually being employed as drug delivery vehicles, nanoparticles and quantum dots as therapeutic agents, functionalized carbon nanotubes as platforms for both therapeutic agents and drug delivery systems and nanocantilevers functionalized for single molecule detection. The results of a literature review on nanotechnology applications for cancer diagnosis and treatment are summarized on Table 1. One of the most obvious differences when comparing nanotechnologies developed is their size relative to one another. Liposomes lie on one end of the size spectrum, with a diameter measuring up to a few microns. Nanotubes and nanocantilevers have one dimension of comparable size, but the other 2 dimensions usually lie in the nanometer range. Nanoparticles, dendrimers and micelles have the same order of magnitude in size, ranging from 10 to a couple hundred nanometers in size. Quantum dots, on the other hand, lie on the extreme opposite to liposomes in the size spectrum, considered a 0D material with no dimension measuring more than 10 nm. Figure 1.4 offers a comparative visual for the most common nanotechnologies mentioned in this work. This makes quantum dots unique for biomedical applications, because

in this magnitude of size you get renal clearance (threshold value of ~5.5 nm)³⁰ and can penetrate a cell membrane (size range 2 – 8 nm).³¹ Although this is just one of many parameters that must be taken into account when designing a biocompatible material for applications in a complex biological matrix, nanoparticle diameter is important and must be designed taking into account the physiology of the system of interest.

Table 1.1: *Most common forms of nanotechnology employed on cancer research, basic description and their role in cancer therapeutics, sensing or drug delivery.*

| Nanotechnology | Physical description | Purpose | Comments |
|-------------------------------|---|---|--|
| Nanoparticles | Metal, metal oxides, cadmium sulfide | Therapeutic, imaging or sensing | Structures of the order of 100 nm |
| Polymeric micelles, Liposomes | Micelle structures | Encapsulation of active compound, drug delivery | Dimensions smaller than 100 nm; limited by toxicity; requires functionalization |
| Dendrimers | Highly organized, macromolecular structures | Encapsulation of active compound, drug delivery | Structures of the order of 100 nm |
| Nanocantilevers | Macromolecular structures, highly organized, 1D | Biomolecule detection | Size of the order of 100 nm |
| Carbon nanotubes | One dimensional nanostructures | Biomolecule detection, sensing | Difficult to employ <i>in vivo</i> ; single molecule detection; requires functionalization |
| Quantum dots | Semiconductor nanoparticles | Therapeutic, imaging, sensing | Length on the order of microns; requires functionalization |

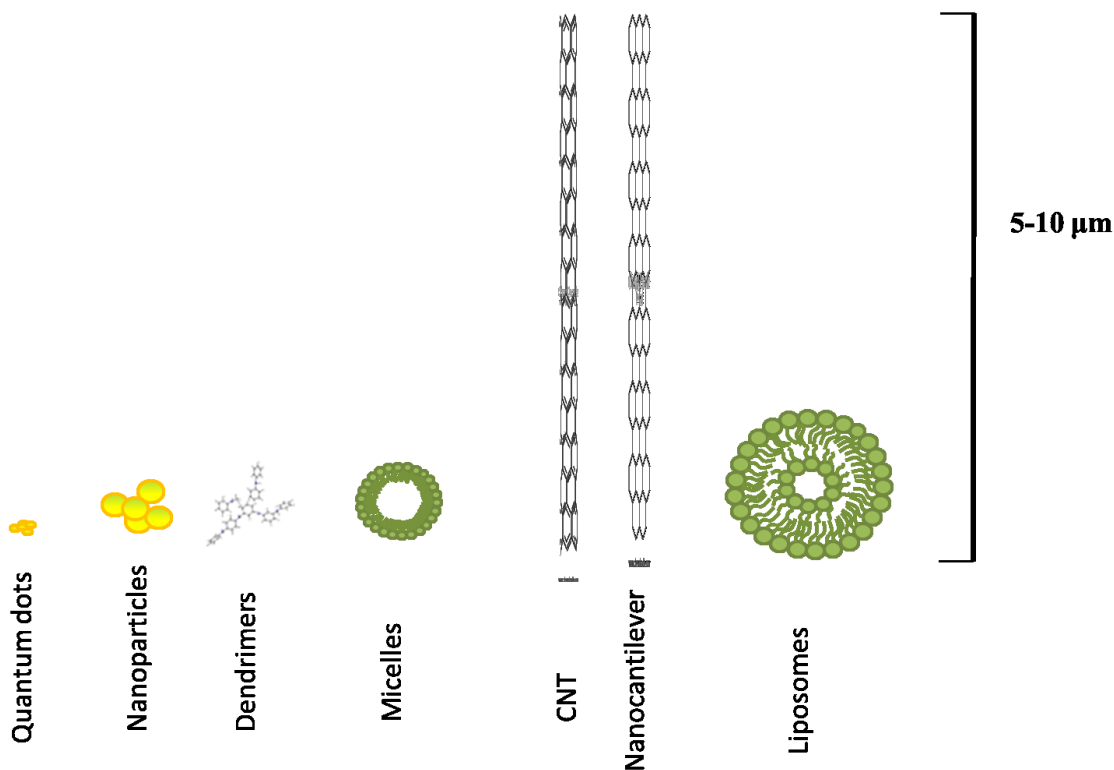


Figure 1.4: *Relative sizes of the most common cancer nanotechnologies*

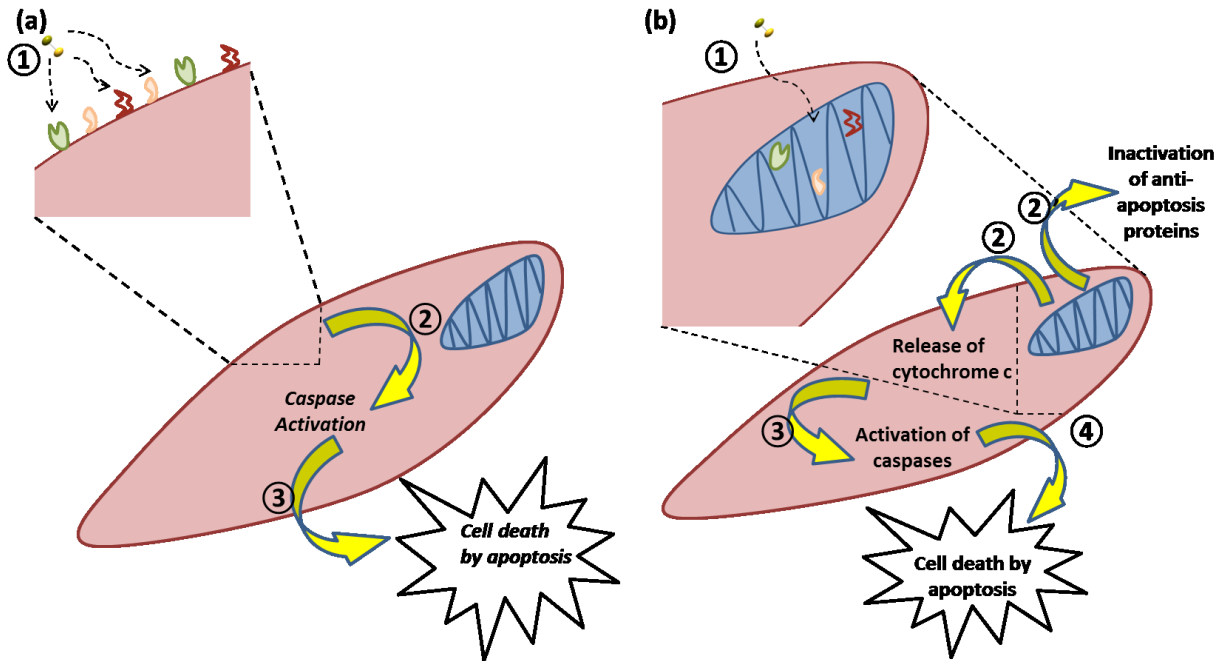
Another parameter explained in detail on a review by Wang, et. al, discusses several nanomaterials already available as cancer treatment agents.³² Among them, Doxil, which is a PEGylated liposome/doxor agent approved for ovarian cancer treatment since 1995. Endorem is a nanostructures agent composed of iron oxide nanoparticles coated with dextran, approved for liver/spleen imaging in Europe. A US analog, Feridex was approved by the US-FDA since 1996. Cyclodex, which is a cyclodextrin nanoparticle based agent, is currently in Phase I trials for the treatment of solid tumors. These are just a few examples of nanotechnologies being developed for detection and/or treatment of several types of cancer. A more comprehensive list of drugs undergoing trials or approved for cancer therapeutics can be found in the literature.^{33–35} Bertrand proposes the classification of nanotechnologies for cancer treatment based on several key factors of the nanostructure.³⁶ Among those, NP size, surface charge, chemical

composition, shape, hydrophobicity, as well as ligand size, orientation, density and charge. These factors are key in the engineering of nanostructured materials that can be used for cancer therapy without adverse or toxicological effects.

One of the main mechanisms believed to play a role in the treatment of cancer cells using quantum dots involves apoptosis. Apoptosis is a morphological phenomenon essential in regulating cell number in animals. It is characterized by the deformation and blebbing of the cell, chromatin condensation, nuclear fragmentation, and a number of other morphological processes that lead to controlled cellular self-destruction.³⁷ Apoptosis is an important process for all metazoan cells, because it serves as a means of getting rid of malfunctioning or damaged cells, and this keeps the total cell number in an organism regulated. One of the hallmarks of cancer is the dysregulation of this process, causing an increase of invasive and malignant cells. This is a “two-edged blade” for carcinoma cells, because by disrupting the mechanism of cell division and provoking apoptosis we may be able to develop novel cancer therapeutics. In order to accomplish this, first we must understand how apoptosis occur and how biocompatible nanomaterials can play a role in the treatment of cancer by triggering this mechanism of cell death in a controlled capacity, so that mostly cancer cells are affected by this therapy. We have performed an experiment for the determination of effects in the replication rate of adenocarcinoma cells in the presence of CaS nanostructures. The results suggest that CaS affects the replication rate of cancer cells without significantly affecting normal analogs used in the experiment. We believe apoptotic events are taking place and the presence of CaS is precipitating these events. Further discussion of the experiment can be found in chapter VI. The next step would be to determine how the CaS nanostructures affect adenocarcinoma cells without

significantly disrupting normal cells. To understand this, we need a better understanding of apoptotic processes.

Although apoptosis may occur through one of many pathways, there are two main mechanisms that have been elucidated. One of them occurs at the cell surface and involves tumor necrosis factor (TNF) family receptors, as shown in Figure 1.5a. The mechanism is known as extrinsic or type I mechanism because it occurs externally, on the surface of the cell. The second mechanism, shown in Figure 1.5b involves the stimuli of the mitochondria either through direct or indirect contact with a stimulating agent. It is known as mitochondrial or type II mechanism. This phenomenon provokes one of two possible processes: the first one is the inactivation of anti-apoptosis proteins by directly binding with another biomolecule which renders them unable to prevent apoptosis. The other possible pathway is to release cytochrome C into the cytoplasm, activating caspases in the cell. This in turn triggers the apoptotic event. In a review by Rizzuto, et. al, the role of Ca^{2+} in apoptotic processes is discussed in detail.³⁸ It is established that an increase in the cytosolic concentration of Ca^{2+} appear both in early and later stages of apoptosis. This is of importance because by knowing what triggers the apoptotic event, we can tailor new materials that can precipitate cell death in cancer cells without affecting normal ones.



Scheme 1.1: (a) Simplified scheme of extrinsic mechanism of apoptosis, also known as cell surface or type I mechanism. Involves ① the activation of tumor necrosis factor (TNF) family receptors, ② activating caspases in the cell, which lead to ③ cell death by apoptosis. (b) Simplified scheme of Intrinsic mechanism. Also known as mitochondrial or type II mechanism. Involves ① the stimulation of the mitochondria to ② release cytochrome c into the cytoplasm, which triggers ③ the activation of caspases, leading to ④ cell death by apoptosis. ②' Inactivation of anti-apoptosis proteins by direct binding may also lead to apoptosis.

In both the extrinsic and intrinsic pathways, the main reason for apoptosis in cells is the activation of caspases. Caspases is the short form of Cysteine Aspartyl-Specific Proteases. Proteases are enzymes responsible for catalyzing hydrolytic cleavage of peptides. There are 14 caspases known in humans and mice, most of which have been linked directly to apoptotic events.^{39,40} A subgroup, caspases -1, -4 and -5 are involved in the process of activating pro-inflammatory proteins. Although both pathways are seen as separate and independent of each other, at multiple levels they may cross, depending on the proteins specific to each cell type.

There are other mechanisms in which cancer tumors can be triggered or suppressed. One of the most important is through DNA damage⁴¹, which occurs because of an alteration in the p53 tumor suppressor protein. Damage to the p53 tumor suppressor protein has been known to trigger tumor development, whereas in cancer cells there has been suppression of the tumor.⁴² Sulfide signaling of caspases⁴³, or other cell type specific mechanisms are also, though not the most well studied, merit mentioning. Siddiqui and his group demonstrated using CuO nanoparticles of up to 22 nm can still enter the mitochondria and cause type II apoptosis for the case of hepatocarcinoma cells.⁴⁴ A second experiment was performed using E. Coli and S. Aureus to determine if there was antimicrobial activity in CaS nanostructures. The results were negative for antimicrobial activity, which further suggests the possibility of CaS entering the cell membrane in order to provoke apoptosis in carcinoma cells. Both bacteria used in the study have an average wall pore size of < 10 nm⁴⁵, which would pose a physical barrier for CaS nanostructures. This hypothesis still needs studies to be confirmed or discarded. However, the data obtained through these experiments have provided with the first insights into the interactions of CaS nanostructures with cells and bacteria. Understanding the interactions of small nanostructures with cells is very important because it can lead, aside from cancer therapy alternatives, to treat inflammations, genetic diseases and other ailments. One example is the work of Leyva and her group, in which they identify a series of small molecules and their potential for caspase -3 and -6 inhibition for treatment of Huntington's disease.⁴⁶

The main objective of this dissertation is to provide insights into the synthesis and characterization of next generation nano materials that are both biocompatible and economically viable. These types of nanoparticles are the cutting edge in many fields of science and technology, including the field of sensors and biomedical sciences. In this work we report on the

development of a calcium-based NS using several synthesis routes including microwave-assisted, double ion exchange and bulk sample dissolution. We explore the possibility of calcium based nanostructures having the potential of substituting heavy metal based nanomaterials for luminescent based sensors in chapter III. We present size dependent optical transitions resulting in tunable luminescence CaS nanoparticles by exciting at visible wavelength. In chapters IV and V, we explore the direct and indirect band gaps of CaS and study several $(\text{CaS})_n$ aggregates using DFT level of theory. The contribution of phonons to these transitions will also be discussed in these chapters. We also report, in chapter VI, the potential application of CaS NS for the treatment of breast cancer. A 2D cell model using adenocarcinoma mammary gland fibroblasts were exposed to CaS NS and the interaction between them led to the decline of the carcinoma fibroblast population. Exposure of normal or non-cancerous fibroblasts from breast cancer tissue to CaS NS did not affect significantly the population growth of the cells. Although further studies using a 3D cell model and bioavailability are required to confirm and improve upon our findings, we suggest this material as a convenient, non-heavy metal based nanomaterial that can be used as a therapeutic agent for breast cancer cells.

Lastly, in chapter VII we present the conclusions of our work and an outlook at the future venues of inquiry that have been opened by the results presented here.

1.1 References:

- (1) Charles Kittel. *Introduction to Solid State Physics*; 8th ed.; John Wiley & Sons, 2005.
- (2) Zhang, Y.; Wang, T.-H. Quantum Dot Enabled Molecular Sensing and Diagnostics. *Theranostics* **2012**, *2*, 631–654.
- (3) Chen, O.; Zhao, J.; Chauhan, V. P.; Cui, J.; Wong, C.; Harris, D. K.; Wei, H.; Han, H.-S.; Fukumura, D.; Jain, R. K. Compact High-Quality CdSe–CdS Core–shell Nanocrystals with Narrow Emission Linewidths and Suppressed Blinking. *Nat Mater* **2013**, *12*, 445–451.
- (4) Shao, L.; Gao, Y.; Yan, F. Semiconductor Quantum Dots for Biomedical Applications. *Sensors* **2011**, *11*, 11736–11751.
- (5) Zhang, C.-Y.; Yeh, H.-C.; Kuroki, M. T.; Wang, T.-H. Single-Quantum-Dot-Based DNA Nanosensor. *Nat Mater* **2005**, *4*, 826–831.
- (6) Cho, E. J.; Holback, H.; Liu, K. C.; Abouelmagd, S. A.; Park, J.; Yeo, Y. Nanoparticle Characterization: State of the Art, Challenges, and Emerging Technologies. *Mol. Pharmaceutics* **2013**, *10*, 2093–2110.
- (7) Hines, D. A.; Kamat, P. V. Recent Advances in Quantum Dot Surface Chemistry. *ACS Appl. Mater. Interfaces* **2014**, *6*, 3041–3057.
- (8) Panneerselvam, A.; Green, M. Recent Advances in Quantum Dot Synthesis. In *Nanoscience: Volume 1: Nanostructures through Chemistry*; 2012.
- (9) Cooper, M. A. *Label-Free Biosensors: Techniques and Applications*; 1st ed.; Cambridge University Press: 32 Ave. of the Americas, New York, NY 10013-2473, USA, 2009.
- (10) Chuang, C.-H. M.; Brown, P. R.; Bulović, V.; Bawendi, M. G. Improved Performance and Stability in Quantum Dot Solar Cells through Band Alignment Engineering. *Nat Mater* **2014**, *13*, 796–801.
- (11) Lan, X.; Masala, S.; Sargent, E. H. Charge-Extraction Strategies for Colloidal Quantum Dot Photovoltaics. *Nat Mater* **2014**, *13*, 233–240.
- (12) Darroudi, M.; Khorsand Zak, A.; Muhamad, M. R.; Huang, N. M.; Hakimi, M. Green Synthesis of Colloidal Silver Nanoparticles by Sonochemical Method. *Materials Letters* **2012**, *66*, 117–120.
- (13) Gai, S.; Li, C.; Yang, P.; Lin, J. Recent Progress in Rare Earth Micro/Nanocrystals: Soft Chemical Synthesis, Luminescent Properties, and Biomedical Applications. *Chem. Rev.* **2014**, *114*, 2343–2389.
- (14) Ghosh Chaudhuri, R.; Paria, S. Core/Shell Nanoparticles: Classes, Properties, Synthesis Mechanisms, Characterization, and Applications. *Chem. Rev.* **2012**, *112*, 2373–2433.
- (15) Ferrer, E.; Nater, S.; Rivera, D.; Colon, J. M.; Zayas, F.; Gonzalez, M.; Castro, M. E. Turning “on” and “off” Nucleation and Growth: Microwave Assisted Synthesis of CdS Clusters and Nanoparticles. *Materials Research Bulletin* **2012**, *47*, 3835–3843.
- (16) Zhu, Y.-J.; Chen, F. Microwave-Assisted Preparation of Inorganic Nanostructures in Liquid Phase. *Chem. Rev.* **2014**, *114*, 6462–6555.
- (17) Thanh, N. T. K.; Maclean, N.; Mahiddine, S. Mechanisms of Nucleation and Growth of Nanoparticles in Solution. *Chem. Rev.* **2014**, *114*, 7610–7630.
- (18) Becker, R.; Döring, W. Kinetische Behandlung Der Keimbildung in Übersättigten Dämpfern. *Ann. Phys. (Leipzig)* **1935**, *24*, 719–752.

- (19) Finney, E. E.; Finke, R. G. Nanocluster Nucleation and Growth Kinetic and Mechanistic Studies: A Review Emphasizing Transition-Metal Nanoclusters. *Journal of Colloid and Interface Science* **2008**, *317*, 351–374.
- (20) Madeline S. León-Velázquez; Marissa Morales; Roberto Irizarry; Miguel E. Castro. Conduction in Colloidal Systems: A Kinetic Study of Ag₂S Semiconductor Nanoparticle Formation. In *Nanoparticles: Synthesis, Stabilization, Passivation, and Functionalization*; ACS Symposium Series; American Chemical Society, **2008**; Vol. 996, pp. 203–213.
- (21) León-Velázquez, M. S.; Irizarry, R.; Castro-Rosario, M. E. Nucleation and Growth of Silver Sulfide Nanoparticles. *J. Phys. Chem. C* **2010**, *114*, 5839–5849.
- (22) Rizvi, S. B.; Ghaderi, S.; Keshtgar, M.; Seifalian, A. M.; Muhammed, M. Semiconductor Quantum Dots as Fluorescent Probes for *in Vitro* and *in Vivo* Bio-Molecular and Cellular Imaging. *Nano Reviews* **2010**, *1*.
- (23) Li, S.; Liu, Z.; Ji, F.; Xiao, Z.; Wang, M.; Peng, Y.; Zhang, Y.; Liu, L.; Liang, Z.; Li, F. Delivery of Quantum Dot-siRNA Nanoplexes in SK-N-SH Cells for BACE1 Gene Silencing and Intracellular Imaging. *Mol Ther Nucleic Acids* **2012**, *1*, e20.
- (24) Bagalkot, V.; Zhang, L.; Levy-Nissenbaum, E.; Jon, S.; Kantoff, P. W.; Langer, R.; Farokhzad, O. C. Quantum Dot–Aptamer Conjugates for Synchronous Cancer Imaging, Therapy, and Sensing of Drug Delivery Based on Bi-Fluorescence Resonance Energy Transfer. *Nano Lett.* **2007**, *7*, 3065–3070.
- (25) Probst, C. E.; Zrazhevskiy, P.; Bagalkot, V.; Gao, X. Quantum Dots as a Platform for Nanoparticle Drug Delivery Vehicle Design. *Adv. Drug Deliv. Rev.* **2013**, *65*, 703–718.
- (26) NCI Research Priorities and Budget <http://www.cancer.gov/researchandfunding/priorities> (accessed Sep 23, 2014).
- (27) Cancer - United States Cancer Statistics (USCS) Data - 2011 Top Ten Cancers <http://apps.nccd.cdc.gov/uscs/toptencancers.aspx> (accessed Sep 25, 2014).
- (28) Cancer Nanotechnology Plan <http://nano.cancer.gov/about/plan/> (accessed Sep 25, 2014).
- (29) Misra, R.; Acharya, S.; Sahoo, S. K. Cancer Nanotechnology: Application of Nanotechnology in Cancer Therapy. *Drug Discov. Today* **2010**, *15*, 842–850.
- (30) Choi, H. S.; Liu, W.; Misra, P.; Tanaka, E.; Zimmer, J. P.; Ipe, B. I.; Bawendi, M. G.; Frangioni, J. V. Renal Clearance of Nanoparticles. *Nat Biotechnol* **2007**, *25*, 1165–1170.
- (31) Van Lehn, R. C.; Atukorale, P. U.; Carney, R. P.; Yang, Y.-S.; Stellacci, F.; Irvine, D. J.; Alexander-Katz, A. Effect of Particle Diameter and Surface Composition on the Spontaneous Fusion of Monolayer-Protected Gold Nanoparticles with Lipid Bilayers. *Nano Lett.* **2013**, *13*, 4060–4067.
- (32) Wang, R.; Billone, P. S.; Mullett, W. M. Nanomedicine in Action: An Overview of Cancer Nanomedicine on the Market and in Clinical Trials. *Journal of Nanomaterials* **2013**.
- (33) Shapira, A.; Livney, Y. D.; Broxterman, H. J.; Assaraf, Y. G. Nanomedicine for Targeted Cancer Therapy: Towards the Overcoming of Drug Resistance. *Drug Resistance Updates* **2011**, *14*, 150–163.
- (34) Parhi, P.; Mohanty, C.; Sahoo, S. K. Nanotechnology-Based Combinational Drug Delivery: An Emerging Approach for Cancer Therapy. *Drug Discovery Today* **2012**, *17*, 1044–1052.
- (35) Hu, C.-M. J.; Aryal, S.; Zhang, L. Nanoparticle-Assisted Combination Therapies for Effective Cancer Treatment. *Ther Deliv* **2010**, *1*, 323–334.

- (36) Bertrand, N.; Wu, J.; Xu, X.; Kamaly, N.; Farokhzad, O. C. Cancer Nanotechnology: The Impact of Passive and Active Targeting in the Era of Modern Cancer Biology. *Advanced Drug Delivery Reviews* **2014**, *66*, 2–25.
- (37) Reed, J. C.; Green, D. R. *Apoptosis : Physiology and Pathology*; Cambridge University Press, **2011**.
- (38) Rizzuto, R.; Pinton, P.; Ferrari, D.; Chami, M.; Szabadkai, G.; Magalhães, P. J.; Di Virgilio, F.; Pozzan, T. Calcium and Apoptosis: Facts and Hypotheses. *Oncogene* **2003**, *22*, 8619–8627.
- (39) Thornberry, N. A.; Lazebnik, Y. Caspases: Enemies within. *Science* **1998**, *281*, 1312–1316.
- (40) Shi, Y. Caspase Activation, Inhibition, and Reactivation: A Mechanistic View. *Protein Science* **2004**, 1979–1987.
- (41) Elmore, S. Apoptosis: A Review of Programmed Cell Death. *Toxicol Pathol* **2007**, *35*, 495–516.
- (42) Selim, M. E.; Hendi, A. A. Gold Nanoparticles Induce Apoptosis in MCF-7 Human Breast Cancer Cells. *Asian Pac. J. Cancer Prev.* **2012**, *13*, 1617–1620.
- (43) Markova, J.; Hudecova, S.; Soltysova, A.; Sirova, M.; Csaderova, L.; Lencesova, L.; Ondrias, K.; Krizanova, O. Sodium/calcium Exchanger Is Upregulated by Sulfide Signaling, Forms Complex with the $\beta 1$ and $\beta 3$ but Not $\beta 2$ Adrenergic Receptors, and Induces Apoptosis. *Pflugers Arch.* **2014**, *466*, 1329–1342.
- (44) Siddiqui, M. A.; Alhadlaq, H. A.; Ahmad, J.; Al-Khedhairy, A. A.; Musarrat, J.; Ahamed, M. Copper Oxide Nanoparticles Induced Mitochondria Mediated Apoptosis in Human Hepatocarcinoma Cells. *PLoS ONE* **2013**, *8*, e69534.
- (45) Turner, R. D.; Hurd, A. F.; Cadby, A.; Hobbs, J. K.; Foster, S. J. Cell Wall Elongation Mode in Gram-Negative Bacteria Is Determined by Peptidoglycan Architecture. *Nat Commun* **2013**, *4*, 1496.
- (46) Leyva, M. J.; DeGiacomo, F.; Kaltenbach, L. S.; Holcomb, J.; Zhang, N.; Gafni, J.; Park, H.; Lo, D. C.; Salvesen, G. S.; Ellerby, L. M.; *et al.* Identification and Evaluation of Novel Small Molecule Pan-Caspase Inhibitors in Huntington’s Disease Models. *Chem Biol* **2010**, *17*, 1189–1200.

Chapter II

Objectives

The objectives of this dissertation are the following:

1. To develop a heavy metal-free quantum dot that can be used as an alternative, biocompatible and “green” option to several, fully developed nanomaterials based on heavy metals such as cadmium and lead.
2. To study the physical and chemical properties of calcium sulfide (CaS) nanostructures and compare different synthesis routes for the development of this nanomaterial.
3. To study the vibrational and optical transitions of CaS nanostructures to understand the relationship between aggregate number and direct/indirect band gap.
4. To employ CaS nanostructures as a potential biomedical tool in the treatment of breast cancer by studying the interaction of carcinoma fibroblasts and their healthy analog with CaS.

Chapter III

Synthesis and characterization of calcium sulfide nanoparticles: towards the development of cadmium free fluorescent nanostructures

1. Introduction

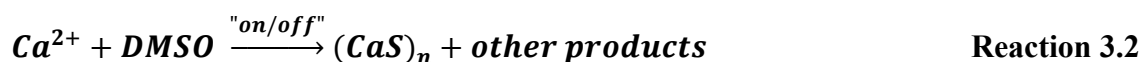
Major limitations in the application of nanotechnologies in clinical practices include toxicology,¹⁻³ lack of biodegradability,⁴⁻⁷ and size to facilitate elimination by the body.⁸⁻¹² Compared to many popular nanomaterials- including the noble metals and magnetic nanoparticles- calcium based nanostructures are promising bio compatible inorganic materials. Calcium is the most abundant mineral in the human body.¹³ It plays major roles in bones, extracellular fluid, protein structures and cell communication, among others.¹⁴ Sulfur, on the other hand, is present in the human body mostly in organic compounds like proteins.¹⁵ Thus, CaS nanostructures have the potential to play an important role as cadmium-free nanoscaled semiconductors with applications in bioimaging,¹⁶⁻²² and in vivo labeling,²³⁻²⁵ and sensing,²⁶⁻³⁰ and for drug delivery systems.³¹⁻³⁴ In addition, CaS is proposed as a biocompatible source of H₂S,^{35,36} and sulfur oxides in chemical fertilizers,³⁷ and components in photovoltaic cells.²⁶ Thus, the chemical and physical properties of calcium sulfide (CaS) nanostructures are of interest due to the wide number of applications that are foreseen for environmentally friendly fluorescent nanostructures.

We report on the synthesis and optical properties of CaS nanostructures. We found that CaS nanostructures prepared by the various methods- illustrated in scheme 1-, including (1) the reaction of Ca(CH₃CO₂)₂ and Na₂S in DMSO, (2) the reaction of Ca(CH₃CO₂)₂ and DMSO in a microwave and (3) dissolving bulk quantities of CaS in DMSO have similar absorption and

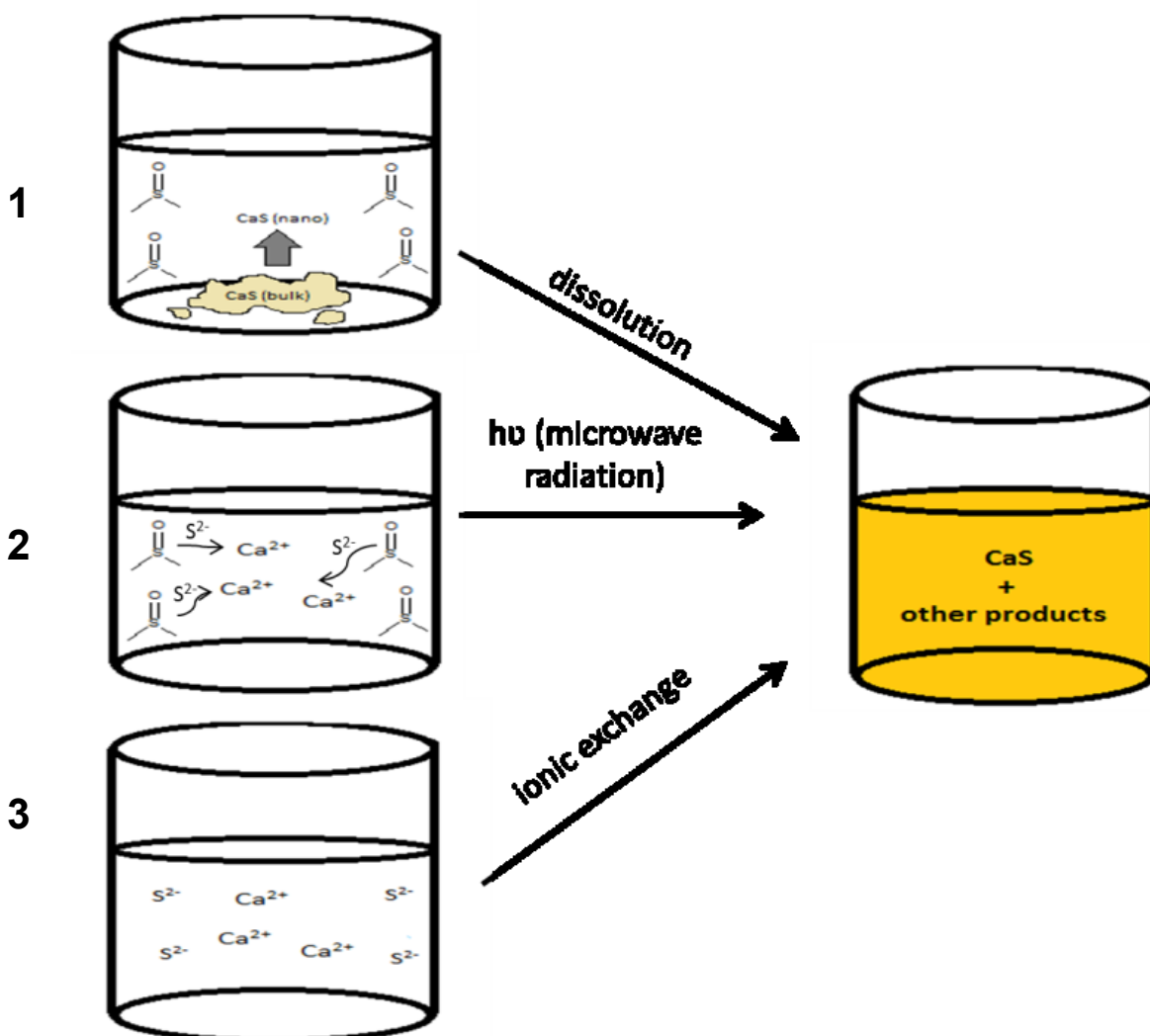
emission spectra. Metathesis, or double ion exchange reaction between Ca^{2+} and S^{2-} ions results in the spontaneous formation of a colored solution. Indeed, approximately 8 kJ/mol are released in the reaction:



The molecular level energy associated with the use of microwaves to heat up chemical reactions, on the other hand, offers the unique advantage to stop the decomposition of DMSO and turn “on” and “off” the CaS synthesis process according to the following process:



Finally, dissolving bulk quantities of CaS powder in DMSO results in dispersions that are free of counter ions like CH_3CO_2^- and Na^+ . The absorption spectra of CaS prepared from these methods consists of a well-defined peak in the UV and a long wavelength tail that extends above 700 nm. Emission bands centered at 400 and 500 nm with a long wavelength tail that extends above 600 nm are observed upon excitation at 310 and 405 nm, respectively. STM measurements reveal the formation of CaS nanoparticles with an average diameter (3.2 ± 0.7) nm. No counterpart is found in the optical properties of the nanostructures with the absorption spectra of CaS in gas phase and bulk material in the solid state. A model involving indirect transitions is proposed to explain the strong absorption features of the nanostructures in the visible and near IR regions.



Scheme 3.1: CaS nanostructures are prepared by various methods including (1) the reaction of $\text{Ca}(\text{CH}_3\text{CO}_2)_2$ and Na_2S in DMSO, (2) the reaction of $\text{Ca}(\text{CH}_3\text{CO}_2)_2$ and DMSO in a microwave and (3) dissolving bulk quantities of CaS in DMSO. The particles are found to emit light at 500 nm following excitation at 405 nm.

EXPERIMENTAL PROCEDURE

Calcium acetate ($\text{Ca}(\text{CH}_3\text{CO}_2)_2$, Fisher Scientific, CAS no. 62-54-4) was used as the source of calcium ions in the chemical processes reported here. Sodium sulfide (CAS no. 1313-82-2) was used without further purification as the source of sulfur for the ion exchange synthesis of CaS.

The desired amount of the reactants employed was measured using a Metler Toledo AT 20 microbalance. The reactants were dissolved in DMSO and sonicated for 15 minutes prior to mixing in a vial, where the resulting dispersion was stored for further measurements. CaS was also prepared from the reaction of $\text{Ca}(\text{CH}_3\text{CO}_2)_2$ and DMSO in a microwave. A solution containing calcium acetate in DMSO was prepared. This solution was heated in cycles of 5-seconds “on” and 15-seconds “off” in a microwave oven. This process was repeated for up to 15 intervals, for a total of 75 seconds of exposure to microwave radiation. CaS was also dissolved with DMSO in a vial. UV-Vis absorption spectroscopy measurements were performed using a PC 2000 Ocean Optics UV-Vis spectrograph. Emission spectroscopy measurements were performed using a Shimadzu Spectrofluorophotometer RF-5301PC (Kyoto, Japan) using a high pressure mercury arc lamp or an E3 laser (Wicked Laser, USA) operating at 405 nm and an OP spectrometer. STM measurements were performed in Nanosurf Easyscan E-STM a using a 0.25 mm $\text{Pt}_{0.8}\text{Ir}_{0.2}$ wire and a bias voltage -0.25 V.

3. Results

3.1 UV-Vis absorption and fluorescence measurements

The solid and dense dots in figure 3.1 represent the absorbance and fluorescence spectra, respectively, of (a) sample prepared by dissolving 7×10^{-5} moles of CaS in DMSO, (b) a mixture of solutions of $\text{Ca}(\text{CH}_3\text{COO})_2$ and Na_2S in DMSO and (c) the product of the microwave mediated reaction of $\text{Ca}(\text{CH}_3\text{COO})_2$ with DMSO. The absorbance spectra are dominated by a long wavelength tail that extends from the UV to over 800 nm. The fluorescence spectra were obtained with a 405 nm excitation. The fluorescence spectra are dominated by a strong band centered around 500 nm and a long wavelength tail that extends above 650 nm. The structure of

the fluorescence spectra is consistent with the fluorescence spectrum of CaS thin films³⁸ and nanocrystals.³⁹

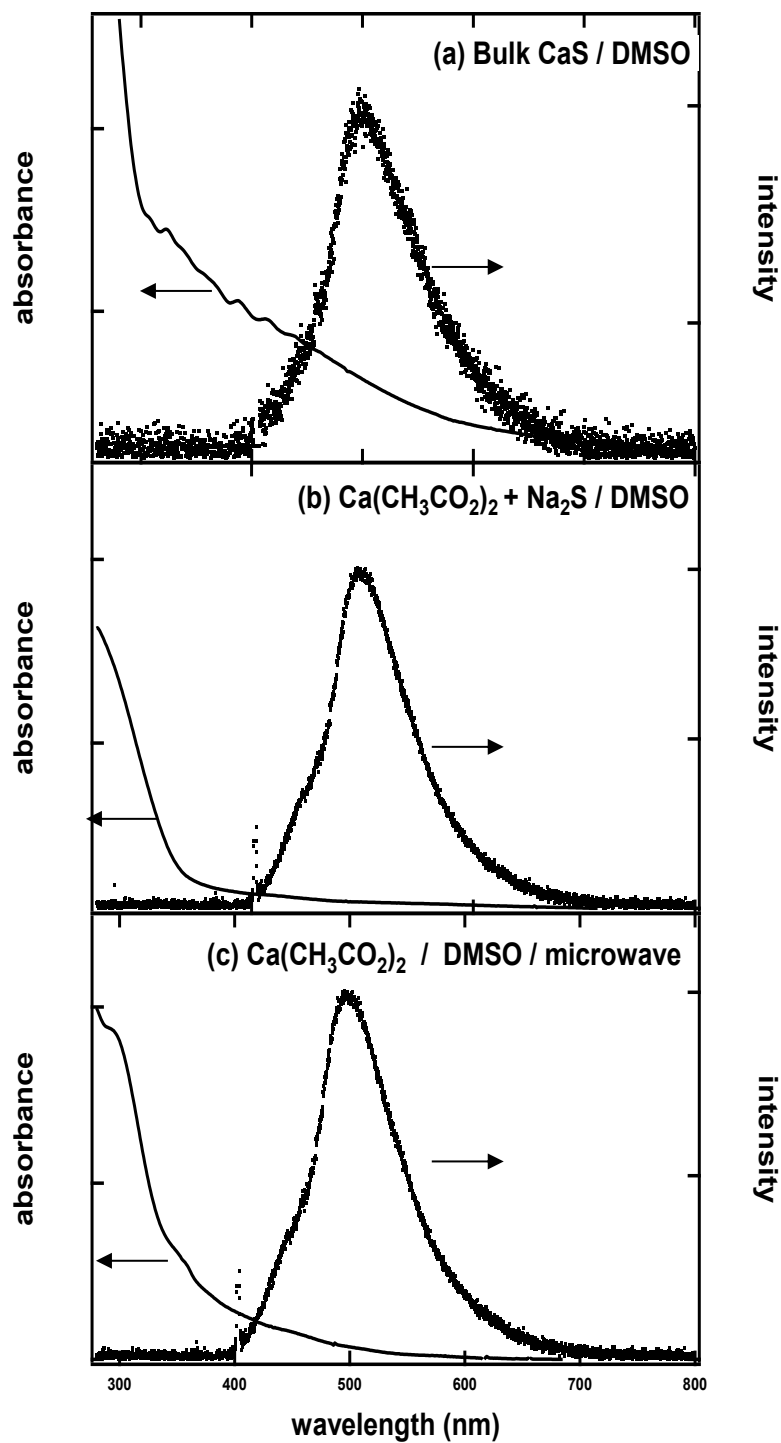


Figure 3.1: The solid and dense dots represent the absorbance and fluorescence spectra, respectively, of (a) sample prepared by dissolving bulk CaS in DMSO, (b) a mixture of solutions of $\text{Ca}(\text{CH}_3\text{CO}_2)_2$ and Na_2S in DMSO and (c) the product of the microwave mediated reaction of $\text{Ca}(\text{CH}_3\text{CO}_2)_2$ with DMSO.

Interestingly, the absorption and fluorescence spectra of the CaS prepared is nearly independent of the method employed for the preparation. This is significant, particularly in the case of the dispersion prepared by dissolving bulk CaS in DMSO. If the dissolution of bulk CaS in DMSO involves free Ca^{2+} and S^{2-} ions, then one would have expected to obtain a clear solution, similar to the ones obtained with free Ca^{2+} and S^{2-} ions in DMSO. Instead, a colored solution with the absorption and emission spectrum indicated in figure 3.1 was always obtained when bulk CaS was dissolved in DMSO. This led us to conclude that CaS nanostructures are formed in the dispersion of bulk CaS in DMSO. These structures were characterized with STM measurements.

3.2 STM measurements.

Selected STM images of regions of a deposit of CaS on MoS_2 are illustrated on figure 3.2. The $100 \times 100 \text{ nm}^2$ image on the left hand side contains a step that is about 3.5 nm in height followed by a region that is densely packed with CaS nanoparticles. The average roughness observed in this region corresponds to $(1.5 \pm 0.2) \text{ nm}$, measured in different regions of two independent $100 \times 100 \text{ nm}^2$ scans. This value is about 0.5 nm higher than on the substrate. The STM image on the right hand side, on the other hand, corresponds to an independent $50 \times 50 \text{ nm}^2$ scan of the indicated area. No specific overall order can be established, although certain degree of order can be spotted in certain regions of the image. The particle size distribution obtained from the analysis of three independent scans is displayed on the bottom of the figure. The particles range in size from 1.6 to 5.2 nm with a peak at 3 nm. The average particle size is $(3.2 \pm 0.7) \text{ nm}$, where the uncertainty corresponds to one standard deviation (1σ).

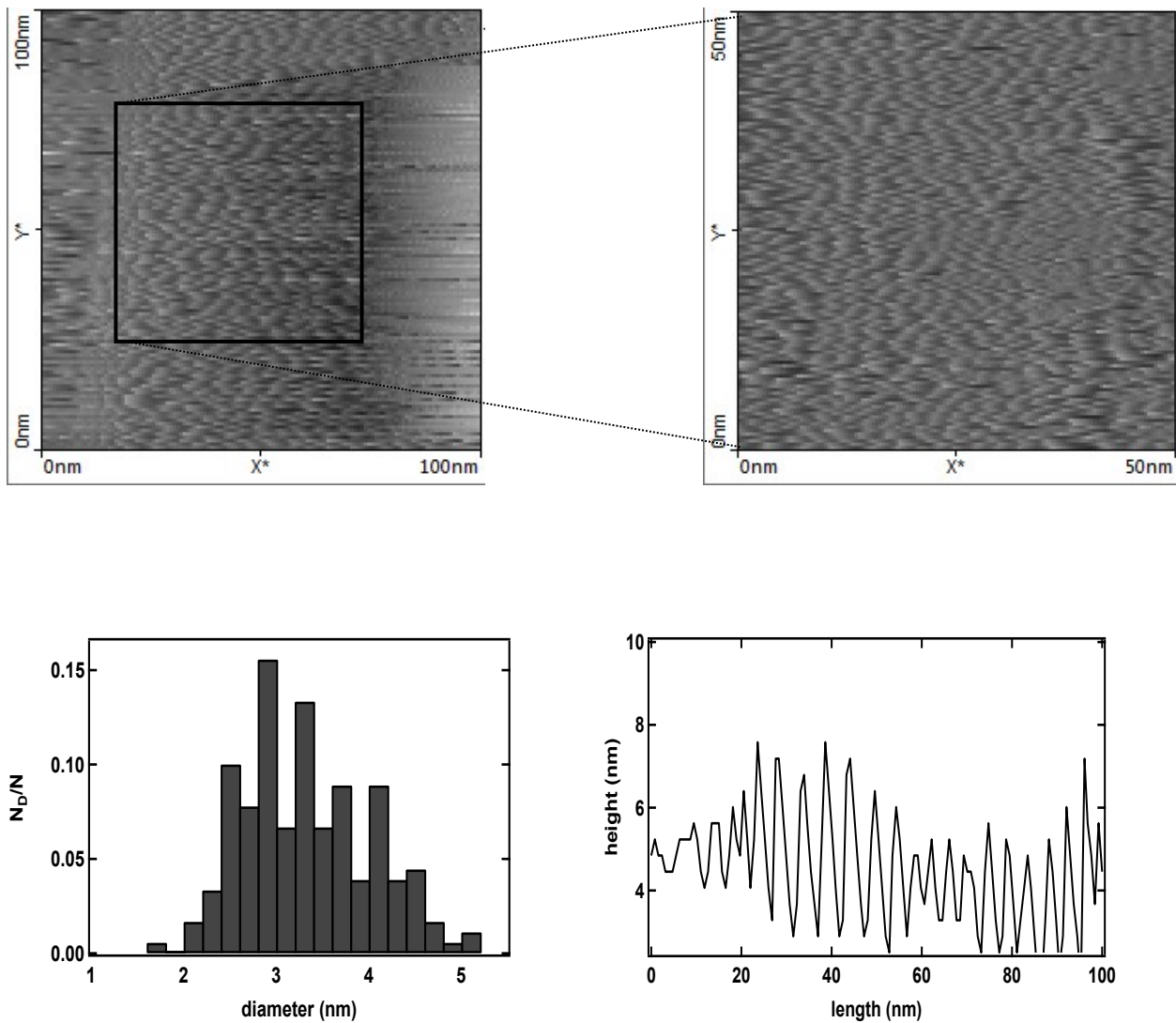


Figure 3.2: The left and right hand side represent selected STM images of independent measurements of $100 \times 100 \text{ nm}^2$ and $50 \times 50 \text{ nm}^2$ regions of a deposit of CaS on MoS_2 , respectively. The particle size distribution obtained from the analysis of three independent scans and height of a selected scan line are displayed on the bottom of the figure.

3.3 Effect of initial calcium concentration.

3.3.1 Absorption measurements as a function of initial calcium concentration.

The dependence of the absorption spectra of dispersions of $\text{Ca}(\text{CH}_3\text{CO}_2)_2$ and DMSO warmed in the microwave on initial calcium concentration are displayed on Figure 3.3. The dispersions

of $\text{Ca}(\text{CH}_3\text{CO}_2)_2$ and DMSO were warmed in the microwave for 75 seconds and allowed to cool to room temperature prior to the measurements. An image of the resulting dispersion, labeled 0 to 5, is also displayed on the bottom panel of Figure 3.4. The numbers employed corresponds to various initial $\text{Ca}(\text{CH}_3\text{CO}_2)_2$ to DMSO concentration ratios indicated in the figure caption. The dependence of the onset of light absorption is a function of initial $[\text{Ca}(\text{CH}_3\text{CO}_2)_2]/[\text{DMSO}]$ ratio is illustrated on the bottom part of the figure. The spectrum of DMSO and $\text{Ca}(\text{CH}_3\text{CO}_2)_2$ exhibits little absorption below 300 nm and is transparent in the visible. The spectrum that corresponds to an initial $[\text{Ca}(\text{CH}_3\text{CO}_2)_2]/[\text{DMSO}]$ ratio of 3×10^{-4} has a well-defined absorption peak centered at 340 nm. The peak red-shifts upon increasing the initial $[\text{Ca}(\text{CH}_3\text{CO}_2)_2]/[\text{DMSO}]$ ratio to 6×10^{-4} . There is a significant change in the appearance of the absorption spectrum when a $[\text{Ca}(\text{CH}_3\text{CO}_2)_2]/[\text{DMSO}]$ ratio of 12×10^{-4} is reached. The spectrum has a broad absorption band below 300 nm followed by a gradual and well defined decrease in absorbance that starts at about 460 nm and extends above 600 nm. The absorbance between 300 and 400 nm and the onset of light absorption shifts slightly toward longer wavelengths with increasing the $[\text{Ca}(\text{CH}_3\text{CO}_2)_2]/[\text{DMSO}]$ ratio.

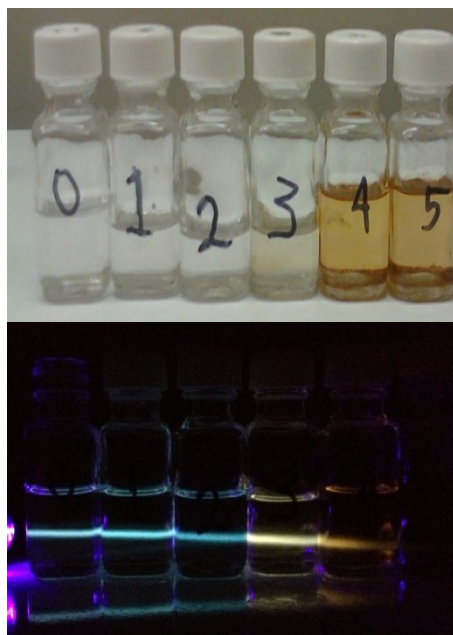
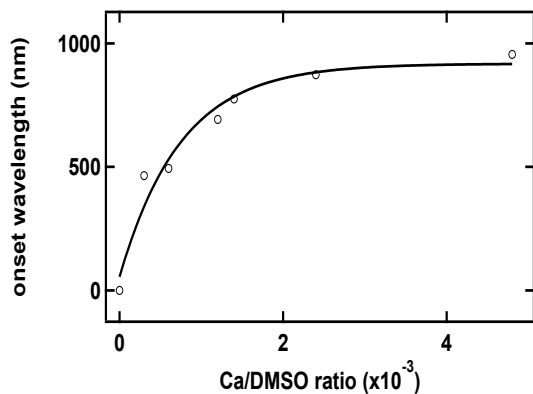
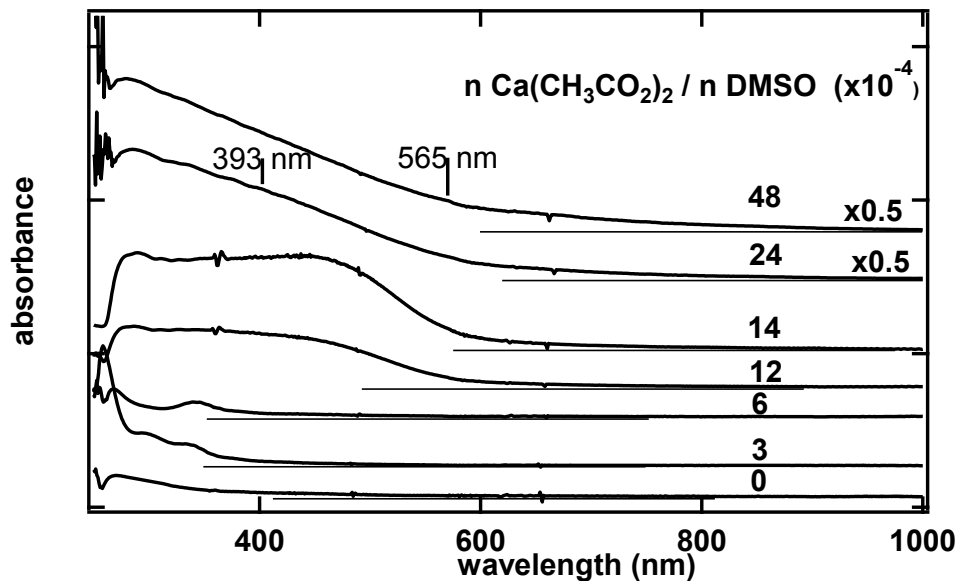


Figure 3.3: The absorption spectra of dispersions CaS prepared with the indicated initial warmed in the microwave on initial $\text{Ca}(\text{CH}_3\text{CO}_2)_2$ /DMSO mole ratio. The dependence of the onset of light absorption and a picture of the samples are indicated on the lower part of the figure. The numbers in the sample's picture corresponds to the initial $[\text{Ca}(\text{CH}_3\text{CO}_2)_2]/[\text{DMSO}]$ concentration ratio indicated from bottom to top in the figure.

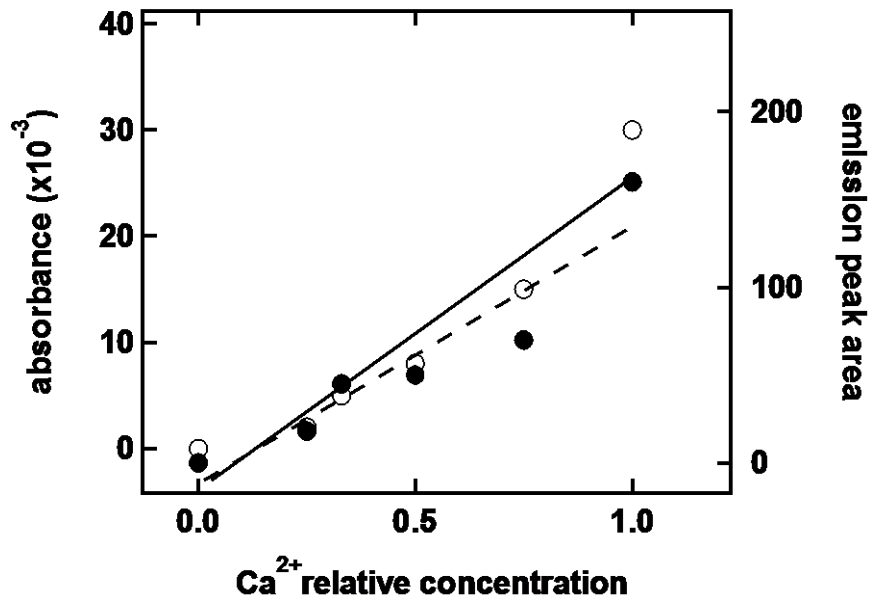
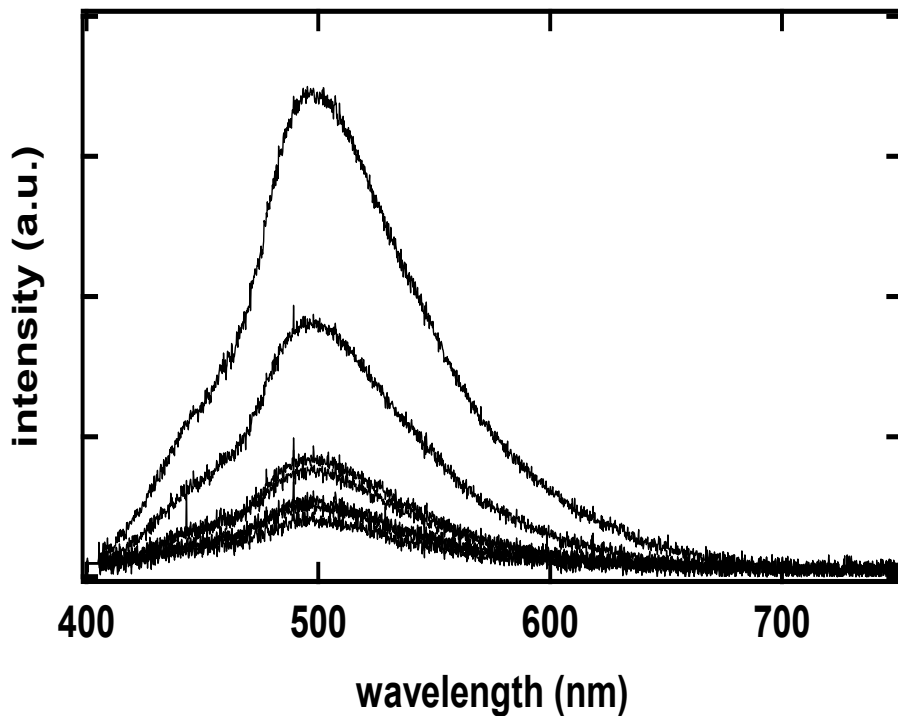


Figure 3.4: The fluorescence spectra of various solutions of CaS prepared from the microwave mediated reaction between $\text{Ca}(\text{CH}_3\text{CO}_2)_2$ and DMSO as a function of the relative initial CaS concentration. The open and closed circles in the bottom panel represent the dependence of the absorbance at 405 nm and the fluorescence peak area on the $[\text{CaS}]$ relative concentration, respectively. The insert is a plot of the fluorescence peak area as a function of the amount of light absorbed at 405 nm by each sample in the dilution sequence.

3.3.2 Fluorescence measurements as a function of calcium sulfide concentration.

Figure 3.4 summarizes the fluorescence spectra of various solutions of CaS prepared from the microwave mediated reaction between $\text{Ca}(\text{CH}_3\text{CO}_2)_2$ and DMSO as a function of the relative CaS concentration. The CaS concentration was varied by diluting the solution that results from the microwave mediated reaction between $\text{Ca}(\text{CH}_3\text{CO}_2)_2$ and DMSO with an initial $[\text{Ca}(\text{CH}_3\text{CO}_2)_2]/[\text{DMSO}]$ ratio of 0.0001. The open and closed circles in the bottom panel of Figure 3.4 represent the dependence of the absorbance at 405 nm and the fluorescence peak area on the $[\text{CaS}]$ relative concentration, respectively. The absorbance at 405 nm and fluorescence peak area increase linearly with the $[\text{CaS}]$. The insert in the same figure is a plot of the fluorescence peak area as a function of the amount of light absorbed at 405 nm by each sample in the dilution sequence displayed on the same figure. A quantum yield of (0.16 ± 0.02) is obtained from a comparison of the slope of the dependence of the fluorescence peak area with the amount of light absorbed by the CaS prepared from the microwave mediated reaction between $\text{Ca}(\text{CH}_3\text{COO})_2$ and DMSO with the corresponding slope obtained for rhodamine 6 G.⁴⁰

4. Discussion

Semiconducting nanocrystals, also known as quantum dots, display physical and chemical properties that differ from their bulk counterparts. Quantum confinement effects are shown to vary proportionally with size. This is because, when the size of the nanoparticle decreases, the number of electronic states diminishes and the quantum oscillations are stronger, but spread over fewer levels. Also, because of their semiconducting nature in this scale, quantum dots exhibit an onset on the UV-Vis absorption spectrum which is directly proportional to the nanoparticle size. We can see in Figure 3.3 the red shift of the absorption onset as a function of Ca / DMSO ratio.

The solution also changed color from a very light yellow to an intense orange and the emission wavelength when excited at 405 nm also shows this red shift associated with quantum confinement. Other important factor affecting the nanoparticle emission wavelength is the presence of “trap states”. Trap states appear when there is a relaxation process that involves less energy, such as an electron vacancy between the valence and conduction band. They can appear when a material is doped with a second type of atom or molecule, resulting in a controlled red shift in emission, and also when coordinated or bonded to an exogenous species, leading to a potential application in sensing of specific target molecules. A third possibility arises when we consider the imperfections of the material. An imperfection can occur in a permanent context, when we consider defects such as steps and different cuts in the crystal structure that can lead to a small shift in the band gap of the material. Another type of imperfection can arise when we consider the contributions from the phonon modes. Vibrations in a nanoparticle play an important role in the indirect band gap of a material. This happens when the valence to conduction band transition involves not only a photon of frequency, but also a phonon. Indirect band gaps, then, depend on the morphology of a material as well as the electronic structure. This possibility is being studied in this work and will be presented in more detail in chapters IV and V.

Conclusions

The optical properties of CaS nanoparticles prepared by various methods, including (1) the reaction of $\text{Ca}(\text{CH}_3\text{CO}_2)_2$ and Na_2S in DMSO, (2) the reaction of $\text{Ca}(\text{CH}_3\text{CO}_2)_2$ and DMSO in a microwave and (3) dissolving bulk quantities of CaS in DMSO are found to be similar. The absorption spectra of CaS prepared from these methods consists of a well defined peak in the UV and a long wavelength tail that extends above 700 nm. Emission bands centered at 400 and 500

nm with a long wavelength tail that extends above 600 nm are observed upon excitation at 310 and 405 nm, respectively. STM measurements reveal the formation of CaS nanoparticles with an average diameter of (3.2 ± 0.7) nm. Light absorption by the particles is proposed to have significant contributions from indirect transitions and/or point defects, and will be discussed in more detail in chapter V.

3.1 References:

- (1) Ye, L.; Yong, K.-T.; Liu, L.; Roy, I.; Hu, R.; Zhu, J.; Cai, H.; Law, W.-C.; Liu, J.; Wang, K.; et al. A Pilot Study in Non-human Primates Shows No Adverse Response to Intravenous Injection of Quantum Dots. *Nature Nanotechnology* **2012**, *7*, 453–458.
- (2) Valizadeh, A.; Mikaeili, H.; Samiei, M.; Farkhani, S. M.; Zarghami, N.; Kouhi, M.; Akbarzadeh, A.; Davaran, S. Quantum Dots: Synthesis, Bioapplications, and Toxicity. *Nanoscale Res Lett* **2012**, *7*, 1–14.
- (3) Hardman, R. A Toxicologic Review of Quantum Dots: Toxicity Depends on Physicochemical and Environmental Factors. *Environ. Health Perspect.* **2006**, *114*, 165–172.
- (4) Roberts, J. R.; Antonini, J. M.; Porter, D. W.; Chapman, R. S.; Scabilloni, J. F.; Young, S.-H.; Schwegler-Berry, D.; Castranova, V.; Mercer, R. R. Lung Toxicity and Biodistribution of Cd/Se-ZnS Quantum Dots with Different Surface Functional Groups after Pulmonary Exposure in Rats. *Particle and Fibre Toxicology* **2013**, *10*, 5.
- (5) Kümmerer, K.; Menz, J.; Schubert, T.; Thielemans, W. Biodegradability of Organic Nanoparticles in the Aqueous Environment. *Chemosphere* **2011**, *82*, 1387–1392.
- (6) Chuev, M.; Cherepanov, V.; Nikitin, M. P.; Polikarpov, M. Biodegradation of Nanoparticles in a Body from Mössbauer and Magnetization Measurements. *Solid State Phenomena* **2012**, *190*, 725–728.
- (7) Chan, W.; Shiao, N. Cytotoxic Effect of CdSe Quantum Dots on Mouse Embryonic Development. *Acta Pharmacol Sin* **2008**, *29*, 259–266.
- (8) Choi, H. S.; Liu, W.; Misra, P.; Tanaka, E.; Zimmer, J. P.; Ipe, B. I.; Bawendi, M. G.; Frangioni, J. V. Renal Clearance of Nanoparticles. *Nat Biotechnol* **2007**, *25*, 1165–1170.
- (9) Li, S.-D.; Huang, L. Pharmacokinetics and Biodistribution of Nanoparticles. *Mol. Pharm.* **2008**, *5*, 496–504.
- (10) Ruiz, A.; Hernández, Y.; Cabal, C.; González, E.; Veintemillas-Verdaguer, S.; Martínez, E.; Morales, M. P. Biodistribution and Pharmacokinetics of Uniform Magnetite Nanoparticles Chemically Modified with Polyethylene Glycol. *Nanoscale* **2013**.
- (11) Yang, Z.; Leon, J.; Martin, M.; Harder, J. W.; Zhang, R.; Liang, D.; Lu, W.; Tian, M.; Gelovani, J. G.; Qiao, A.; et al. Pharmacokinetics and Biodistribution of Near-infrared Fluorescence Polymeric Nanoparticles. *Nanotechnology* **2009**, *20*, 165101.
- (12) Arvizo, R. R.; Miranda, O. R.; Moyano, D. F.; Walden, C. A.; Giri, K.; Bhattacharya, R.; Robertson, J. D.; Rotello, V. M.; Reid, J. M.; Mukherjee, P. Modulating Pharmacokinetics, Tumor Uptake and Biodistribution by Engineered Nanoparticles. *PLoS ONE* **2011**, *6*, e24374.
- (13) Calcium — QuickFacts <http://ods.od.nih.gov/factsheets/Calcium-QuickFacts/> (accessed Oct 10, 2013).
- (14) Calcium in diet: MedlinePlus Medical Encyclopedia <http://www.nlm.nih.gov/medlineplus/ency/article/002412.htm> (accessed Oct 10, 2013).
- (15) Parcell, S. Sulfur in Human Nutrition and Applications in Medicine. *Altern Med Rev* **2002**, *7*, 22–44.
- (16) Arya, H.; Kaul, Z.; Wadhwa, R.; Taira, K.; Hirano, T.; Kaul, S. C. Quantum Dots in Bioimaging: Revolution by the Small. *Biochem. Biophys. Res. Commun.* **2005**, *329*, 1173–1177.

- (17) Hutter, E.; Maysinger, D. Gold Nanoparticles and Quantum Dots for Bioimaging. *Microsc. Res. Tech.***2011**, *74*, 592–604.
- (18) Hutter, E.; Maysinger, D. Gold-nanoparticle-based Biosensors for Detection of Enzyme Activity. *Trends Pharmacol. Sci.***2013**, *34*, 497–507.
- (19) Zrazhevskiy, P.; Sena, M.; Gao, X. Designing Multifunctional Quantum Dots for Bioimaging, Detection, and Drug Delivery. *Chem Soc Rev***2010**, *39*, 4326–4354.
- (20) Zrazhevskiy, P.; Gao, X. Quantum Dot Imaging Platform for Single-cell Molecular Profiling. *Nat Commun***2013**, *4*, 1619.
- (21) Zhang, Y.; Kaji, N.; Tokeshi, M.; Baba, Y. Nanobiotechnology: Quantum Dots in Bioimaging. *Expert Rev Proteomics***2007**, *4*, 565–572.
- (22) Martínez Maestro, L.; Jacinto, C.; Rocha, U.; Carmen Iglesias-de la Cruz, M.; Sanz-Rodríguez, F.; Juarranz, A.; García Solé, J.; Jaque, D. Optimum Quantum Dot Size for Highly Efficient Fluorescence Bioimaging. *Journal of Applied Physics***2012**, *111*, 023513.
- (23) Kirchner, C.; Liedl, T.; Kudera, S.; Pellegrino, T.; Muñoz Javier, A.; Gaub, H. E.; Stölzle, S.; Fertig, N.; Parak, W. J. Cytotoxicity of Colloidal CdSe and CdSe/ZnS Nanoparticles. *Nano Lett.***2005**, *5*, 331–338.
- (24) Resch-Genger, U.; Grabolle, M.; Cavaliere-Jaricot, S.; Nitschke, R.; Nann, T. Quantum Dots Versus Organic Dyes as Fluorescent Labels. *Nat. Methods***2008**, *5*, 763–775.
- (25) Giraud, G.; Schulze, H.; Bachmann, T. T.; Campbell, C. J.; Mount, A. R.; Ghazal, P.; Khondoker, M. R.; Ross, A. J.; Ember, S. W. J.; Ciani, I.; et al. Fluorescence Lifetime Imaging of Quantum Dot Labeled DNA Microarrays. *International Journal of Molecular Sciences***2009**, *10*, 1930–1941.
- (26) Tang, J.; Kemp, K. W.; Hoogland, S.; Jeong, K. S.; Liu, H.; Levina, L.; Furukawa, M.; Wang, X.; Debnath, R.; Cha, D.; et al. Colloidal-quantum-dot Photovoltaics Using Atomic-ligand Passivation. *Nat Mater***2011**, *10*, 765–771.
- (27) Williams, G.; Kamat, P. V. Graphene–Semiconductor Nanocomposites: Excited-State Interactions Between ZnO Nanoparticles and Graphene Oxide †. *Langmuir***2009**, *25*, 13869–13873.
- (28) Rizvi, S. B.; Yildirimer, L.; Ghaderi, S.; Ramesh, B.; Seifalian, A. M.; Keshtgar, M. A Novel POSS-coated Quantum Dot for Biological Application. *Int J Nanomedicine***2012**, *7*, 3915–3927.
- (29) Ghaderi, S.; Ramesh, B.; Seifalian, A. M. Synthesis of Mercaptosuccinic acid/MercaptoPolyhedral Oligomeric Silsesquioxane Coated Cadmium Telluride Quantum Dots in Cell Labeling Applications. *J Nanosci Nanotechnol***2012**, *12*, 4928–4935.
- (30) Ghaderi, S.; Ramesh, B.; Seifalian, A. M. Fluorescence Nanoparticles “Quantum Dots” as Drug Delivery System and Their Toxicity: a Review. *J Drug Target***2011**, *19*, 475–486.
- (31) Obonyo, O.; Fisher, E.; Edwards, M.; Douroumis, D. Quantum Dots Synthesis and Biological Applications as Imaging and Drug Delivery Systems. *Crit. Rev. Biotechnol.***2010**, *30*, 283–301.
- (32) Qi, L.; Gao, X. Emerging Application of Quantum Dots for Drug Delivery and Therapy. *Expert Opin Drug Deliv***2008**, *5*, 263–267.
- (33) Korthout, K.; Smet, P. F.; Poelman, D. Rare Earth Doped Core-shell Particles as Phosphor for Warm-white Light-emitting Diodes. *Applied Physics Letters***2011**, *98*, 261919.
- (34) *Inorganic Phosphors*. CRC Press. **2004**.

- (35) Caliendo, G.; Cirino, G.; Santagada, V.; Wallace, J. L. Synthesis and Biological Effects of Hydrogen Sulfide (H₂S): Development of H₂S-releasing Drugs as Pharmaceuticals. *J. Med. Chem.* **2010**, *53*, 6275–6286.
- (36) Li, Y.-F.; Xiao, C.-S.; Hui, R.-T. Calcium Sulfide (CaS), a Donor of Hydrogen Sulfide (H₂S): A New Antihypertensive Drug? *Medical Hypotheses* **2009**, *73*, 445–447.
- (37) Zhang, X.; Song, X.; Sun, Z.; Li, P.; Yu, J. Density Functional Theory Study on the Mechanism of Calcium Sulfate Reductive Decomposition by Methane. *Fuel* **2013**, *110*, 204–211.
- (38) Nnabuchi, M. N.; Okeke, C. E. Characterization of Optimized Grown Calcium Sulphide Thin Films and Their Possible Applications in Solar Energy. *PJST* **2004**, 72–82.
- (39) Wang, C.; Tang, K.; Yang, Q.; An, C.; Hai, B.; Shen, G.; Qian, Y. Blue-light Emission of Nanocrystalline CaS and SrS Synthesized via a Solvothermal Route. *Chemical Physics Letters* **2002**, *351*, 385–390.
- (40) Crosby, G. A.; Demas, J. N. Measurement of Photoluminescence Quantum Yields. Review. *J. Phys. Chem.* **1971**, *75*, 991–1024.

Chapter IV:

Nucleation and growth process in calcium sulfide: towards the understanding of the stability of small aggregates

1. Introduction

In this chapter we report theoretical calculations on the light absorption and light emission properties of $(\text{CaS})_n$ nanoclusters. The calculated spectra were then compared against experimental values obtained by the synthesis of CaS nanostructures using microwave irradiation using calcium acetate and DMSO as the source of calcium and sulfur, respectively. UV-Vis spectra calculated using configuration interaction singles (CIS) method for $(\text{CaS})_n$ clusters with $1 \leq n \leq 5$ were compared with the experimental values obtained. Vibrational data from the CaS were calculated using several functional/basis set combinations, compared against one another and against experimental data obtained and reported in the literature. Results on optimized structures of $(\text{CaS})_n$ clusters in the gas phase and in DMSO are also presented. We found that stepwise formation of $(\text{CaS})_2$ and $(\text{CaS})_3$ is energetically favored in the gas phase. A significant energy barrier is found in the addition of monomers to the dimer in DMSO. $(\text{CaS})_2$ is the most likely cluster predicted to exist in DMSO at the early stages of nucleation.

2. Discussion

2.1 Absorption and emission spectra of CaS nanostructures.

Colored dispersions are formed when transparent solutions of $\text{Ca}(\text{CH}_3\text{CO}_2)_2$ in DMSO are exposed to microwave radiation, as established in the previous chapter in Figure 3.3b and 3.3 c.

The absorption spectra of CaS dispersions as a function of the initial $\text{Ca}(\text{CH}_3\text{CO}_2)_2$ to DMSO mole ratios are illustrated on Figure 3.3a. The absorption spectra have a well-defined band in the UV and long wavelength absorption features that extends to the near IR. The absorption edge depends on the initial $\text{Ca}(\text{CH}_3\text{CO}_2)_2$ in DMSO ratio and ranges from the UV to as high as 750 nm in the near IR.

The changes in the absorption spectra experienced by a solution with a $\text{Ca}(\text{CH}_3\text{CO}_2)_2$ in DMSO ratio of 10^{-3} to different exposure times of microwave radiation are displayed on Figure 4.1. The spectrum of the dispersion prepared by exposure to microwave radiation by 20 seconds is dominated by a band centered at 275 nm. Further increase in microwave exposure time results in an increase in the intensity of this band and absorption at longer wavelengths. There is no significant change in the spectra following exposure to microwave radiation by 40 seconds. The spectrum of the dispersion that results from exposing the solution to microwave radiation for 80 seconds is dominated by absorption that starts in the UV and extends to above 600 nm.

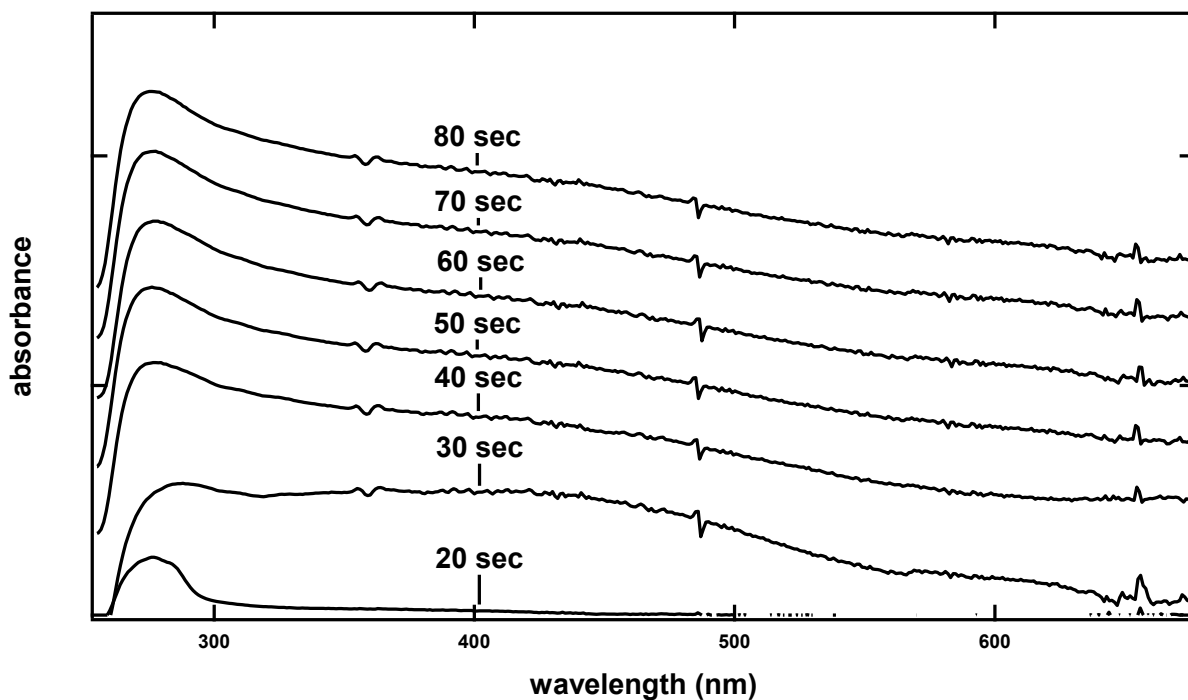


Figure 4.1: Absorption spectrum of $\text{Ca}(\text{CH}_3\text{CO}_2)_2$ in DMSO mole ratio of 10^{-3} to different exposure times of microwave radiation.

The emission spectra of a CaS dispersion in DMSO is presented in figure 3.4. The emissions spectra are obtained following excitation at 405 nm. The emission spectrum of the dispersion with a 3×10^{-4} $\text{Ca}(\text{CH}_3\text{CO}_2)_2$ to DMSO ratio has a well defined band centered at 497 nm and extends to 750 nm in the emission spectrum. A quantum yield of 16 % is determined from a plot of the emission peak area as a function of the absorbance at 405 nm.

3.2 Theoretical calculations for CaS

3.2.1 Theoretical calculations of CaS monomers.

Table 4.1 summarizes the results of calculations on the CaS monomer at various levels of density functional theory (DFT). Ca-S is a linear molecule with a $\text{C}_{\infty\text{v}}$ point group symmetry.

Bond lengths ranged from 2.27846 Å at the LSDA/DGDZVP functional/basis set to 2.64759 Å at the B3LYP/LANL2MB level of theory. Solid CaS has a face centered cubic cell of calcium ions inserted in a face centered cubic cell of sulfur. The lattice parameter is 5.689 Å and the Ca-S distance is 2.85 Å.¹ A bond length of 2.38626 Å in gas phase CaS has been reported from rotational spectroscopy measurements.² Thus the calculated Ca-S distances are between 80 and 93 % of the known Ca-S distance in solid calcium sulfide and within 90 to 95 % from the gas phase value. The range of vibrational frequencies calculated is from 340 to 490 cm⁻¹, which are within 75 to 90 % of the experimental value of 430 cm⁻¹ in the gas phase.³

Table 4.1: Results of the geometry optimization, formation energy from the respective atoms (ΔE_a), formation energy from the respective Ca^{2+} and S^{2-} ions (ΔE_i), frequency, Ca-S bond length of optimized monomer, dipole moment and percent ionic character calculated for the gas phase monomer using several functional and basis set combinations.

| Functional / Basis set | Energy (hartrees) | ΔE_a (hartrees) | ΔE_i (hartrees) | frequency (cm^{-1}) | bond length (\AA) | calcium charge | Dipole moment (D) | % ionic character |
|------------------------|-------------------|-------------------------|-------------------------|--------------------------------|------------------------------|----------------|-------------------|-------------------|
| B3LYP / DGDZVP | -1075.698219 | -0.18739229 | -0.94417475 | 470.075 | 2.32185 | 0.637 | 10.1647 | 74 |
| B3LYP / 6311G | -1075.778099 | -0.13255007 | -0.84012773 | 341.615 | 2.58633 | 0.946 | 11.3279 | 83 |
| B3LYP / LANL2DZ | -46.64111339 | -0.11570448 | -0.92899262 | 352.743 | 2.60947 | 0.743 | 9.6856 | 71 |
| B3LYP / LANL2MB | -46.62627239 | -0.10168505 | -1.07319081 | 340.125 | 2.64759 | 0.62 | 7.9656 | 58 |
| B3PW91 / DGDZVP | -1075.582842 | -0.20035876 | -0.9350466 | 482.168 | 2.30429 | 0.677 | 10.6357 | 78 |
| LSDA / DGDZVP | -1073.227823 | - | -0.9780947 | 490.238 | 2.27846 | 0.57 | 9.4291 | 69 |
| PBEPBE / DGDZVP | -1075.27923 | - | -0.95936584 | 468.785 | 2.3129 | 0.608 | 9.5794 | 70 |

The ionic or polar covalent bond and a pure covalent bond is always the basis of argument. The electronegativities of calcium and sulfur, according to the Pauling scale of electronegativities, are 1.00 and 2.58, respectively. The difference in electronegativities between calcium and sulfur is consistent with a covalent polar bond. A reasonable measure of the percent of ionic character can be obtained by comparing the electronegativities of the elements involved according to:

$$\% \text{ ionic character} = (1 - e^{-0.25*(X_a - X_b)^2}) * 100 \quad \text{Equation 4.3}$$

Where X_a and X_b represent the electronegativities of the elements that are involved in the bond. The use of the electronegativities of calcium and sulfur in Equation 4.3 gives a 46 % ionic character and a 54 % covalent character for the Ca-S bond. The percent of ionic character can also be estimated from a comparison of the dipole moment (μ) in a bond and the dipole moment of the corresponding interatomic distance times the charge (eR) if it was completely ionic:

$$\% \text{ ionic character} = \left(\frac{\mu}{eR}\right) * 100 \quad \text{Equation 4.4}$$

The percent of ionic character calculated with Equation 4.4 using the dipole moments determined theoretically for different functional/basis set combinations are indicated in the last column of Table 4.1. For the calculation of the eR factor in the denominator, we have used the Ca-S bond length of 2.38626 Å which corresponds to a dipole moment of 13.6527 D for a CaS with a 100 % ionic bond character. The percent of ionic character ranges from 58 at the B3LYP/LANL2MB to 83 for B3LYP/6311G levels of theory. Thus the percent of ionic character obtained using B3LYP/LANL2MB are in closer agreement with the percent ionic character predicted by Equation 4.3 based on the difference in electronegativity between calcium and sulfur.

2.2.2 Experimental and theoretical absorption spectra of CaS monomers.

The simulated absorption spectrum of the CaS monomer in the gas phase is illustrated in figure 4.2. The absorption spectrum of CaS was obtained at the CIS/DGDZVP level of theory. The absorption and emission spectra of CaS monomers in the gas phase have been determined experimentally. The ground state of the CaS monomer in the gas phase is $X^1\Sigma^+$. Emission measurements place the $B^1\Sigma^+$ excited electronic state between 1.6 and 2.0 eV (774 to 614 nm) above the $X^1\Sigma^+$ ground state.^{2,3} The existence of additional excited states, $G^1\Pi$ and $F^1\Pi$ and $F^3\Pi$, have been established by independent emission measurements.⁴ These states are between 2.9 and 3.0 eV (413 to 427 nm) above the ground electronic state. The $A^1\Pi$ state, on the other hand, has been estimated to be about 16260 cm^{-1} below the $G^1\Pi$ state from fluorescence measurements, about 7470 cm^{-1} or 0.93 eV (1333 nm) above the $X^1\Sigma^+$ ground state. Thus there are a number of electronic transitions that have been observed in gas phase of CaS over a wide range of wavelengths from the ultraviolet to the near IR region.⁵⁻⁷

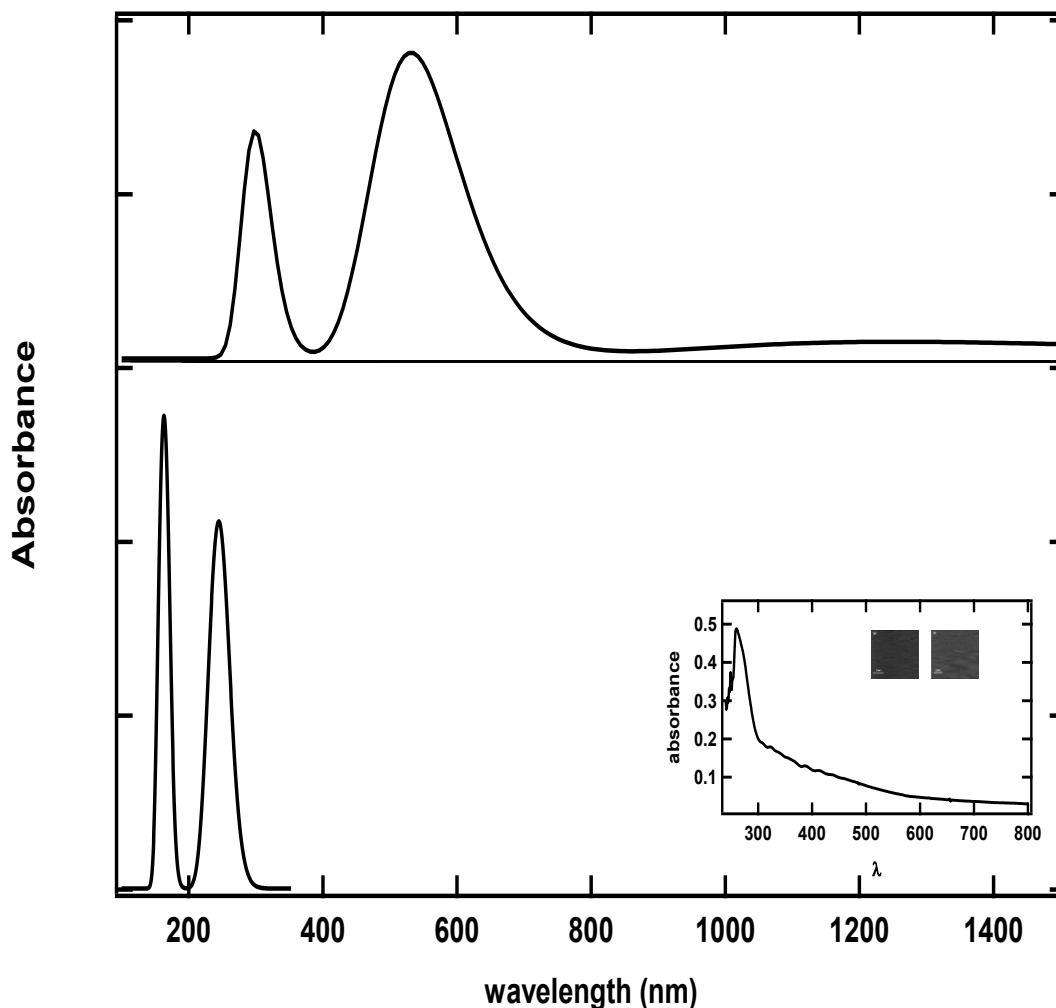


Figure 4.2: The upper and lower panel are the calculated absorptions spectra of CaS monomers in the gas phase and in DMSO between 190 and 1500 nm, respectively. The insert is the absorption spectrum of a dispersion with a $\text{Ca}(\text{CH}_3\text{CO}_2)_2$ to DMSO ratio of 3×10^{-4} .

The electronic transitions calculated are in close agreement with the observed transitions CaS monomers in the gas phase reported above. The calculated spectrum of calcium sulfide monomers, using B3LYP/DGDZVP, is dominated by strong bands centered at 302 nm and 537 nm and a weaker band at 1262 nm. The calcium sulfide HOMO is a doubly degenerate π orbital with a strong contribution from the sulfur $3p$ orbitals perpendicular to the molecular axis and a

smaller contribution from the calcium $3d$ orbital. The LUMO is a σ hybrid orbital dominated by the calcium $4s$. The HOMO to LUMO transition is predicted to occur at approximately 1262 nm. The energy level diagram is shown in Figure 4.3. The transitions in the visible region of the spectrum are predicted to result from electrons excited from the HOMO to high level empty $3d$ orbitals localized in the calcium as well as from the sulfur $3s$ to the LUMO. These transitions result in a broad band centered at 532 nm. The transitions in the UV region, on the other hand, result from excitations from the double degenerate HOMO to empty calcium $3d$ orbitals. These transitions are expected to occur between 253 and 393 nm with a peak at 302 nm. The HOMO to LUMO transitions occur at much shorter wavelengths in the highly symmetric $(\text{CaS})_2$ and $(\text{CaS})_3$ clusters. In the $(\text{CaS})_4$ and $(\text{CaS})_5$ clusters the lowest energy HOMO to LUMO transitions are predicted to occur in the near IR. This is an important prediction since materials with optical properties in the near IR are expected to have important applications for *in vivo* labeling measurements where the interference with light absorption and emission by body fluids can be minimized.^{8,9}

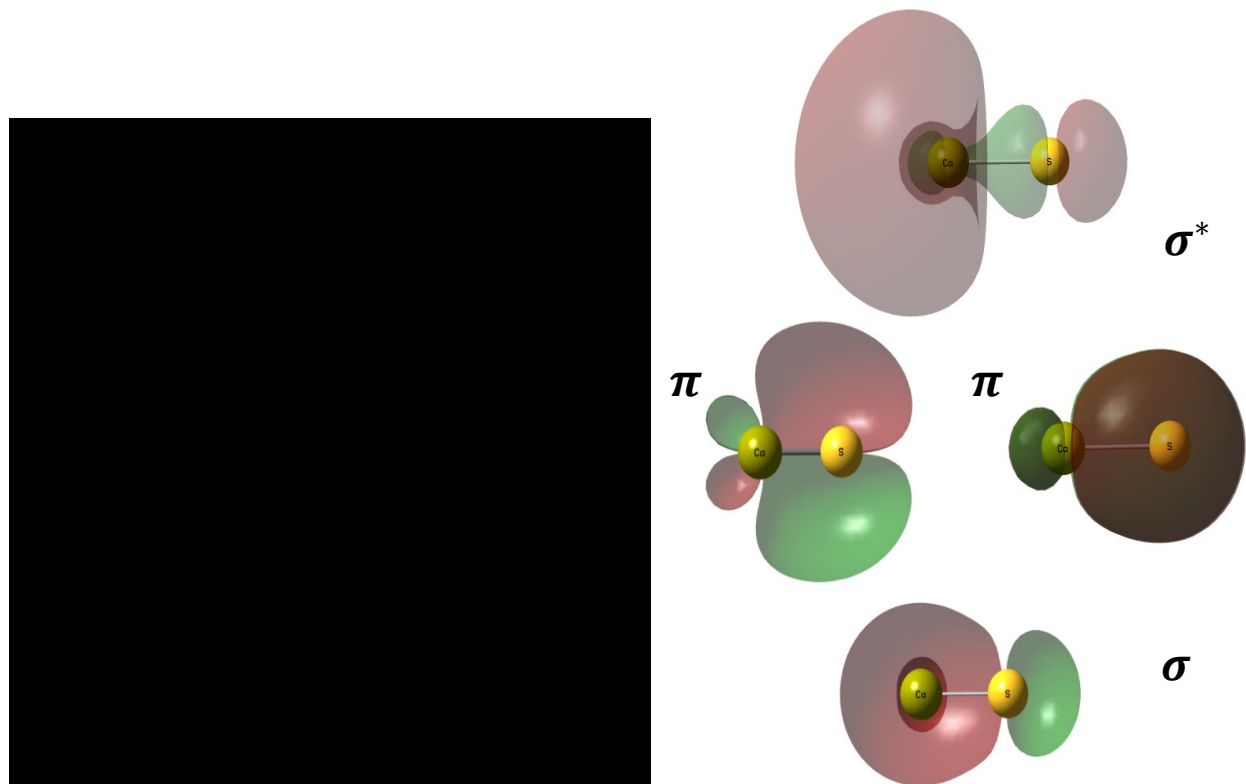


Figure 4.3: Energy level diagram of the occupied and empty orbitals of CaS. The doubly degenerate π and the σ orbitals are indicated on the right hand side of the figure.

We have also studied the effect of the DMSO in the emission spectra of CaS monomers. The emission spectrum of CaS in DMSO is displayed in Figure 3.1. The spectrum is dominated by transitions at 190 nm and 270 nm. The dielectric constant of the DMSO has the effect of removing all light absorption in the visible and near IR regions of the electromagnetic spectrum. The experimental spectrum of CaS obtained with a $\text{Ca}(\text{CH}_3\text{CO}_2)_2$ to DMSO ratio of 3×10^{-4} is displayed as an insert in Figure 4.2. The spectrum is dominated by a single band at 270 nm and long wavelength tail that extends to the visible. The band at 270 nm is predicted to result from HOMO to LUMO transitions in CaS monomers in DMSO. Our UV-visible detector can not reach deeper in the UV which limits the observation of the band at 200 nm predicted by theory.

The long wavelength tail to the visible results from heterogeneities in the dispersion that results in the formation of structures with larger number of $(\text{CaS})_n$ units.

3.2.3 Experimental determination of absorption and emission spectra for $(\text{CaS})_n$

The absorption spectra predicted for $(\text{CaS})_n$ clusters in the gas phase with aggregate number ranging from $n=1$ to $n=5$ is summarized on Figure 4.4. We have included the predicted absorption spectra of the monomer discussed earlier for reference. Absorption bands at 334 nm, 537 nm and 1262 nm are predicted for the monomer in the gas phase. The calculations predict transitions below 500 nm for the dimer ($n = 2$), trimer ($n = 3$) and tetramer ($n = 4$). Transitions that extends to near 2000 nm are predicted for two isomers of the clusters with $n = 5$. Thus absorption at longer wavelengths are expected for structures with aggregation number larger than 5. Assuming that DMSO would have a similar effect on clusters with $n = 5$ as with the monomers, we expect larger clusters to have relevant optical transitions in the UV and visible range.



Figure 4.4: Absorption spectra between 190 and 2000 nm of optimized $(CaS)_n$, with $1 \leq n \leq 5$, clusters.

3.2.4 Energy considerations in the formation of CaS clusters

The physical processes involved in nanostructure synthesis are important to understand the different approaches for nanoparticle synthesis. The process that governs the synthesis, that is to say, the size and morphology of the material, are usually explained using nucleation and growth theory. Nucleation is the process that results in the formation of a new phase or structure by self assembly or self organization. In the nucleation process free precursor atoms or molecules or

ions re-arrange themselves through a series of processes into a phase similar to the product and large enough to have the ability to grow in size irreversibly.¹⁰ This process is governed to a large extent by the difference in chemical potential ($\Delta\mu$) of the molecule in solution (μ_s) and in the bulk of the crystal (μ_c), given by equation 1.1:

$$\Delta\mu = \mu_s - \mu_c$$

Equation 1.1

The difference in chemical potential can also be expressed as:

$$\Delta\mu = kT \ln[\textit{precursors}]_s$$

Equation 1.2

A more detailed description of the classical nucleation and growth process can be found in chapter I. The formation of CaS quantum dots can be explained using nucleation and growth theory. The precursors to the formation of monomer units are the S^{2-} ions, supplied by the microwave mediated decomposition of DMSO, and Ca^{2+} ions.¹¹ The formation of CdS clusters has been observed in the synthesis of CdS nanoparticles in a microwave-assisted reaction. In that case, it was proposed that the formation of the nanoparticles occurs by the stepwise addition of monomer units and coupling of clusters. Here, we establish that the formation of CaS monomers is energetically possible under the conditions of our experiments. We assume that formation is initiated by the reaction of Ca^{2+} and S^{2-} ions to form CaS monomers. Formation of a dimer $(CaS)_2$, is then thought to occur by coupling two monomer units. Such process requires that the cluster formed to be more stable than the precursor. The dependence of the cluster energy on aggregation number is displayed on Figure 4.5 a. Cluster energies are calculated at the B3LYP/DGDZVP level of theory. The cluster energy decreases at a rate of about -2820.4

(kJ/mol) per aggregation number (n). The formation of clusters can be thought to occur by coupling a CaS monomer to the dominant structure in dispersion according to:



The binding energy is defined as:

$$E_B = -\frac{E_n}{n} + E_1 \quad \text{Equation 4.1}$$

where E_1 and E_n represent the energy of the first aggregate (monomer) and at the n^{th} aggregate number, respectively. These values were calculated using the cluster energies discussed above. The results are presented on figure 4.5b. These results suggest an increase in binding energy with increasing cluster size: the higher the binding energy the more stable the structure is. A maximum value is reached when $n = 3$, with a decrease in energy for $n = 4$. This suggests that the monomers and clusters with $n = 2$ and 3 will most likely be the dominant species in this system in the early stages of the nucleation process, because there is an energy barrier for $n = 4$ and 5 clusters. Figure 4.5c shows the change in total energy as a function of aggregate size. The change in total energy is calculated as:

$$\Delta E = E_n - E_{n-1} \quad \text{Equation 4.2}$$

A minimum is reached for the $n = 2$ aggregate, with a slightly less negative change in energy for the trimer and a dramatic increase for the $n = 4$ and $n = 5$ cases.

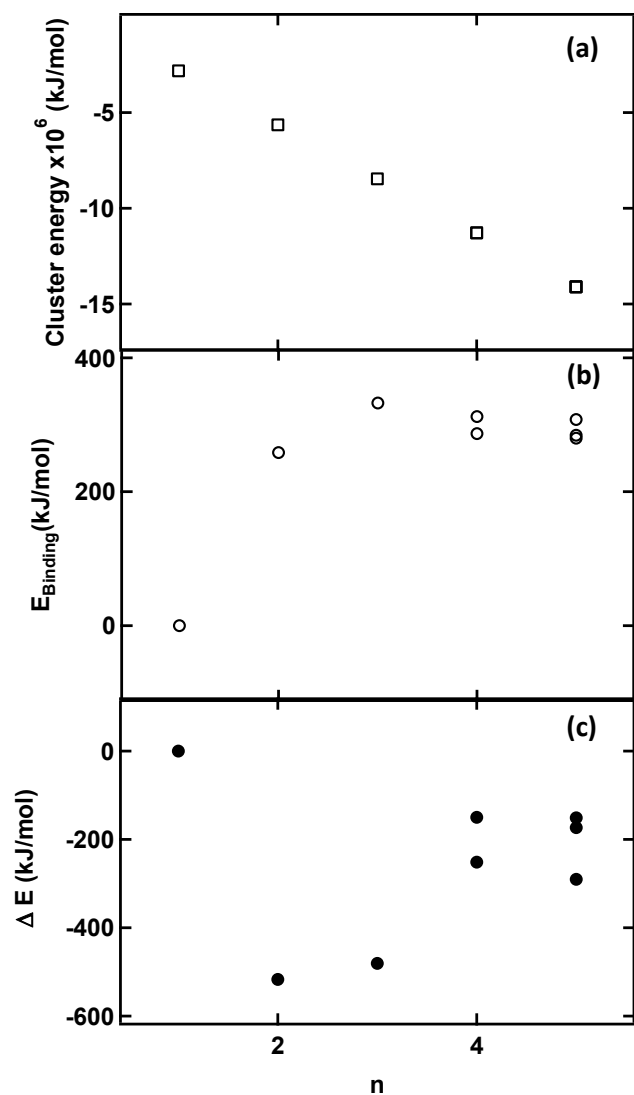


Figure 4.5: Results of theoretical calculation for a CaS clusters in the gas phase. (a) Cluster energy as a function of aggregate number for $(CaS)_n$, on the insert we can see the binding energy for $(CaS)_n$ as a function of aggregate number. (b) Change in energy as a function of aggregate number for $(CaS)_n$.

The discussion presented in the previous paragraphs uses calculations performed on gas phase monomers and clusters. Actually, the nucleation process takes place in solution, where the new phase formed is solvated and stabilized by the solvent. The nucleation in a process governed by Equation 1.3 and the balance of surface free energy of the new phase where the clusters are

trapped is an important factor to consider. It is reasonable that, in the presence of an excess of solvent molecules, the surface free energy of the new phase that trap the small clusters remains nearly the same. Under this assumption, then the energy of coupling clusters becomes an important term to consider.

Results of the energy change of CaS clusters with aggregation number n between 1 and 4 in the DMSO dielectric are summarized on figure 4.6. The calculation predicts an energy barrier to form the trimer from the addition of monomer units to the dimer. This is an important effect of the solvent: it can trap clusters of specific size by limiting its ability to polymerize through the addition of monomer units. Coupling of two dimers to form a tetramer is possible but energetically uphill. Thus the calculations predict that dimers are the most likely calcium and sulfide containing nanostructure at the early stages of nucleation.

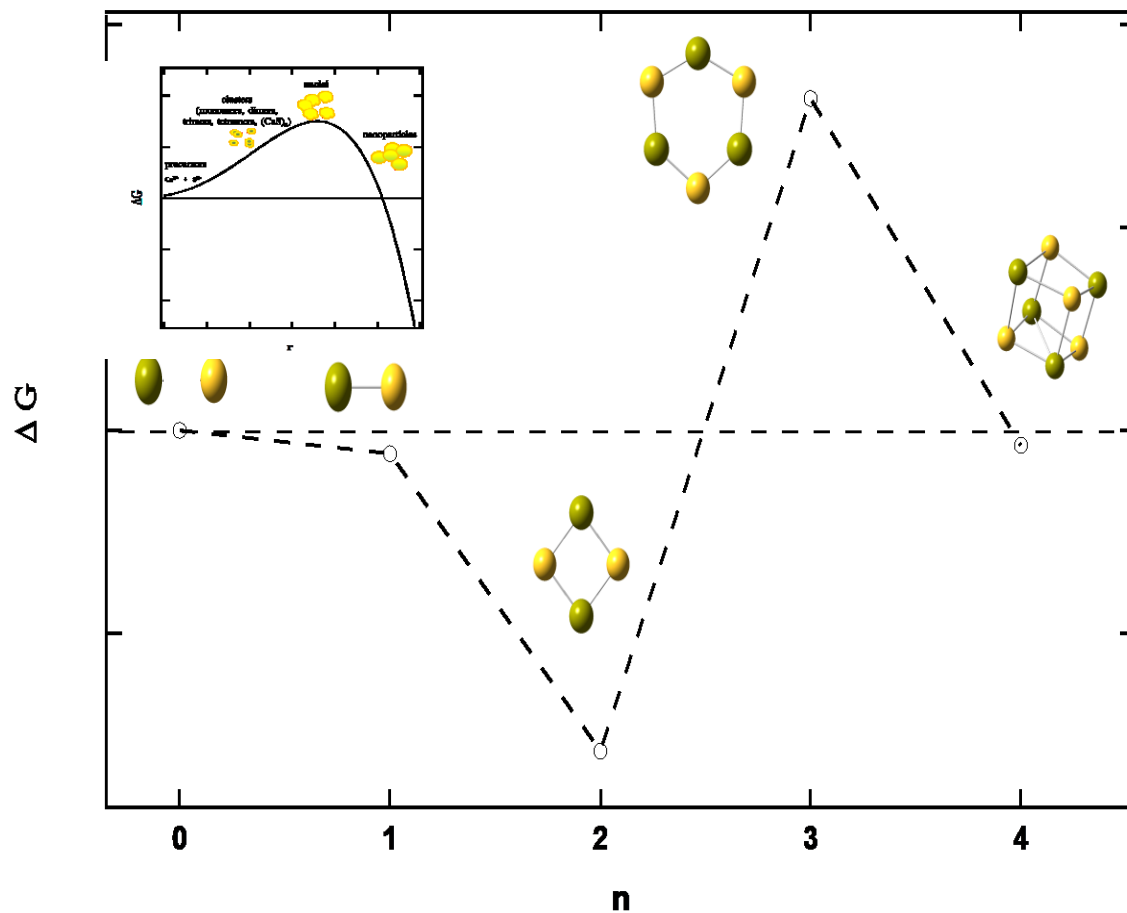


Figure 4.6: Gibbs free energy to form calcium sulfide clusters by the stepwise addition of monomers as a function of aggregation number. The insert represents the Gibbs free energy change associated with a nucleation process as a function of phase or particle size. See text for details.

4.1 References:

- (1) Lide, D. R. *CRC Handbook of Chemistry and Physics*; 89th ed.; 2009.
- (2) Takano, S.; Yamamoto, S.; Saito, S. Millimeter Wave Spectra of MgS and CaS. *Chemical Physics Letters* **1989**, *159*, 563–566.
- (3) Jarman, C. N.; Hailey, R. A.; Bernath, P. F. A Laser Study of the Blue Electronic Transitions of CaS. *The Journal of Chemical Physics* **1992**, *96*, 5571.
- (4) Melville, T. C.; Coxon, J. A. High-Resolution Laser Spectroscopy of CaS: Deperturbation Analysis of the $A1\Sigma^+ - X1\Sigma^+$ Transition†. *J. Phys. Chem. A* **2002**, *106*, 8271–8275.
- (5) Wang, C.; Tang, K.; Yang, Q.; An, C.; Hai, B.; Shen, G.; Qian, Y. Blue-Light Emission of Nanocrystalline CaS and SrS Synthesized via a Solvothermal Route. *Chemical Physics Letters* **2002**, *351*, 385–390.
- (6) Gruzintsev, A. N.; Volkov, V. T.; Pronin, A. N. Investigation of Luminescence Centers of Unactivated CaS Films. *Journal of Crystal Growth* **1992**, *117*, 975–978.
- (7) Sinel'nikov, B. M.; Kargin, N. I.; Savel'ev, V. A.; Danilov, V. P. Thin-Film Electroluminescent Emitters Based on Calcium Sulfide Doped with Cerium. *J Appl Spectrosc* **1995**, *62*, 552–554.
- (8) Bannas, P.; Well, L.; Lenz, A.; Rissiek, B.; Haag, F.; Schmid, J.; Hochgräfe, K.; Trepel, M.; Adam, G.; Ittrich, H.; *et al.* In Vivo near-Infrared Fluorescence Targeting of T Cells: Comparison of Nanobodies and Conventional Monoclonal Antibodies. *Contrast Media Mol. Imaging* **2014**, *9*, 135–142.
- (9) Rolfe, P. In Vivo near-Infrared Spectroscopy. *Annu Rev Biomed Eng* **2000**, *2*, 715–754.
- (10) Thanh, N. T. K.; Maclean, N.; Mahiddine, S. Mechanisms of Nucleation and Growth of Nanoparticles in Solution. *Chem. Rev.* **2014**, *114*, 7610–7630.
- (11) Ferrer, E.; Nater, S.; Rivera, D.; Colon, J. M.; Zayas, F.; Gonzalez, M.; Castro, M. E. Turning “on” and “off” Nucleation and Growth: Microwave Assisted Synthesis of CdS Clusters and Nanoparticles. *Materials Research Bulletin* **2012**, *47*, 3835–3843.

Chapter V

Quantum Confinement Effects in Calcium Sulfide: The Role of Indirect Transitions in the Red Shift of the Band Edge in Semiconductor Nanoparticles

1. Introduction

The chemical and physical properties of calcium sulfide (CaS) are of interest due to its applications as a controlled source of hydrogen sulfide (H₂S) in the human body^{1,2} as well as cadmium-free fluorescent nanomaterials for applications in bioimaging³, labeling⁴, sensing⁵, photovoltaic components⁶ and for drug delivery systems.⁷ Calcium sulfide can be produced cost-effectively in large scales. Despite its importance and potential applications, the spectroscopic properties of CaS are not well established. On a review done by Smet, et al.⁸ the potential of CaS as a luminescent material and proposed as cathodo-, photo- and luminescent material for LED applications is established. CaS has been prepared as a phosphorescent material and doped with rare earth metals, among other metals for narrow wavelength emission.⁹ Although this provides for an efficient method of preparing phosphorescence-based sensing materials, the cost of preparing these materials is elevated. Also, there is a lack of understanding of CaS without doping as a luminescent material in its own right. Absorption properties are also not being studied as well as emission spectra concerning doped CaS. In this work we report on experimental and theoretical calculations on the light absorption properties of (CaS)_n nanoclusters. Light absorption by the CaS prepared from the reaction of Ca(CH₃CO₂)₂ in DMSO exhibits a broad absorption band that extends from the UV to above 1000 nm. A strong emission band at 500 nm ($\phi = 0.16$) with a long wavelength tail that extends above 600 nm is observed in

the emission spectrum of the CaS excited at 405 nm. The optical properties of $(\text{CaS})_n$ nanoclusters are found to be sensitive to the nanocluster size. Absorption features that extend from the ultraviolet to the visible range are observed in the monomer as well as the tetramer. Light absorption is predicted to extend to the near IR in clusters with $n = 5$. Vibrational data from the CaS aggregates is calculated using several levels of theory and compared with one another and experimental data reported in the literature.

2. Experiment

Calcium acetate (CAS no. 62-54-4, Fisher Scientific) was used as the source of calcium ions in the chemical process reported here. CaS was prepared from the reaction of $\text{Ca}(\text{CH}_3\text{CO}_2)_2$ and DMSO in a microwave. A solution containing calcium acetate in DMSO (CAS no. 67-68-5) in a vial was prepared. This solution was heated using a microwave in a process described by Ferrer.¹⁰ UV-Vis absorption spectroscopy measurements were performed using a PC 2000 Ocean Optics UV-Vis spectrograph. STM measurements were performed in nanosurf easyscan E-STM a using a 0.25 mm $\text{Pt}_{0.8}\text{Ir}_{0.2}$ wire and a bias voltage -0.25 V. Theoretical calculations on optimized structures were performed with the Gaussian 03 package using Gauss View 5.0 in a Windows PC environment.¹¹

3. Discussion

3.1 Experimental determination of electronic spectra for $(\text{CaS})_n$

A representative $50 \times 50 \text{ nm}^2$ STM image of a CaS nanoparticle deposit with a $[\text{Ca}]/[\text{DMSO}]$ ratio of 1×10^{-4} is displayed on figure 5.1a. The particles have an average diameter of (3.2 ± 0.7) nm. A clear solution is obtained when $\text{Ca}(\text{CH}_3\text{CO}_2)_2$ is dissolved in DMSO. The initial $[\text{Ca}]/[\text{DMSO}]$ ratio is 3×10^{-4} . The solution turns into an orange dispersion when warmed in the

microwave for a total of 75 seconds (figure 5.1b). The corresponding optical absorption spectrum is displayed on figure 5.1c. The dispersion has a well-defined absorption band that ranges from 280 nm to over 600 nm. The absorption is nearly constant at 0.3 units between 300 and 580 nm, typical of semiconductor materials. The fundamental band gap in solid CaS, on the other hand, is 4.43 eV.¹² The fundamental band gap is an indirect transition from the Γ to X states. The direct gaps at the Γ and X points are 5.80 and 5.34 eV, respectively. We can identify the fundamental band gap (4.43 eV) at about 283 nm in the spectrum displayed on figure 5.1b. Absorption at the longer wavelengths is of interest because it broadens the applications of this material.¹³

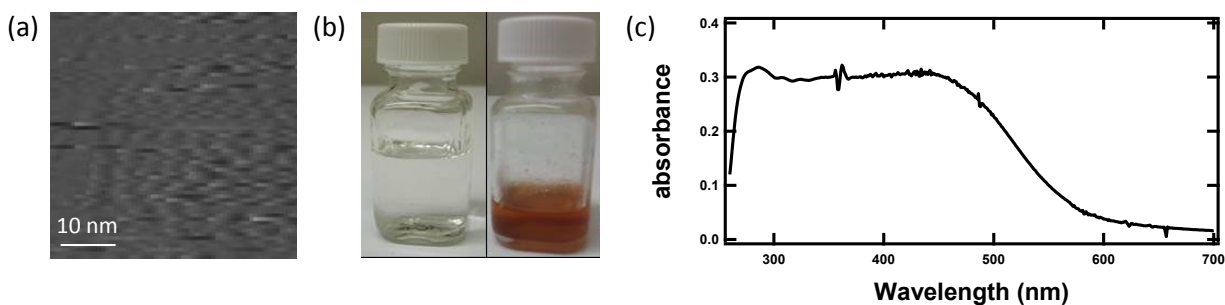


Figure 5.1: (a) A representative $50 \times 50 \text{ nm}^2$ STM image of a CaS NP deposit with a $[\text{Ca}]/[\text{DMSO}]$ ratio of 1×10^{-4} is displayed on figure 1a. The particles are $(3.2 \pm 0.7) \text{ nm}$. (b) A clear solution (left side) is obtained when $\text{Ca}(\text{CH}_3\text{CO}_2)_2$ is dissolved in DMSO, and it turns into an orange dispersion when warmed in the microwave for a total of 75 seconds (right side). (c) Absorption spectrum of CaS solution.

There are several models to correlate the direct band gap of a semiconductor particle with its diameter.¹⁴ Brus has elaborated a model for the dependence of band gap energy and particle size in spherical quantum dots (QD):

$$E_{gap\ QD} = \Delta E_{gap\ bulk} + \frac{\hbar^2}{8R^2} * \left(\frac{1}{m_e} + \frac{1}{m_h} \right) - 1.8 \frac{c^2}{4\pi\epsilon_0\epsilon R} \quad \text{Equation 5.1}$$

where $E_{gap\ QD}$ represents the band gap in the quantum dot, m_e and m_h are the electron and hole masses, respectively, $\Delta E_{(gap\ bulk)}$ represents the band gap in the bulk material, \hbar and ϵ_0 are Planck's constant and the permittivity of vacuum, ϵ is the dielectric constant of the solid. and R is the gas constant.¹⁵ The term in the middle of equation 5.1 is the particle-in-a-box correction for the exciton and the last term is the contribution of the electron-hole Coulombic attraction. Traditionally the second term dominates as the particle size falls below the exciton Bohr radius, making the nanoparticle band gap larger than in the bulk material. We are not aware of any measurements of the effective electron-hole mass of CaS, although it is known for a few other semiconductor nanoparticles. Furthermore, knowledge of the effective mass is of little use to the case of CaS, which has indirect, in addition to direct, band gaps. An approach to describe quantum confinement effects in indirect band gap semiconductor nanostructures has been the subject of a few studies.¹⁶ Even tensile strain has been found to induce a transition from direct to indirect semiconductor in germanium quantum dots and self-assembled quantum dots.¹⁷ Attempts to accommodate experimental observations into a single model may be a difficult task due to the dependence of band structure on particle size and morphology as well as on vibrational frequency and phonon dispersion characteristics. The absorptivity coefficient (A) in indirect semiconductors is related to the band gap ($\Delta E_{(gap\ bulk)}$) and phonon energy (E_{phonon}) according to:

$$(AE_0)^{\frac{1}{2}} \propto E_0 - \Delta E_{(gap\ bulk)} \pm E_{phonon} \quad \text{Equation 5.2}$$

where E_0 represents the incident photon energy and the plus (+) or minus (-) sign holds in the case of light absorption or emission by the phonon, respectively. In the case of direct transitions, on the other hand, the absorptivity is related to the band gap according to:

$$(AE_0)^2 \propto E_0 - \Delta E_{(gap\ bulk)} \quad \text{Equation 5.3}$$

where A , E_0 , and $\Delta E_{(gap\ bulk)}$ were defined above. Experimentally, indirect and direct band gap energies are determined by considering the energy at which the absorptivity coefficient (A) falls to zero. Rigorously, the intercept in the coordinate axis of plots of $(AE_0)^{1/2}$ or $(AE_0)^2$ as a function of incident photon energy (E_0) represents the indirect or direct band gap energy, respectively. The indirect band gap in CaS is located at lower energies than the direct band gap. As a result, indirect band gaps are easier to locate in the optical absorption spectrum. The upper and lower side panels in figure 5.2 represent plots of $(AE_0)^2$ and $(AE_0)^{1/2}$ as a function of incident photon energy. The values of $(AE_0)^2$ and $(AE_0)^{1/2}$ are deduced from the absorption spectrum of the dispersion prepared by dissolving solid CaS in DMSO at room temperature. This solution is free of Na^+ and $CH_3CO_2^-$ ions that are present in dispersions prepared from the reaction of Na_2S and $Ca(CH_3CO_2)_2$ or DMSO and $Ca(CH_3CO_2)_2$ in a microwave. The indirect band gap energy is obtained from the initial rise in $(AE_0)^{1/2}$ as a function of energy. We estimate indirect and direct band gaps of (0.403 ± 0.003) eV and (4.135 ± 0.006) eV from the plots of $(AE_0)^{1/2}$ and $(AE_0)^2$ as a function of incident photon energy displayed on figure 5.2.

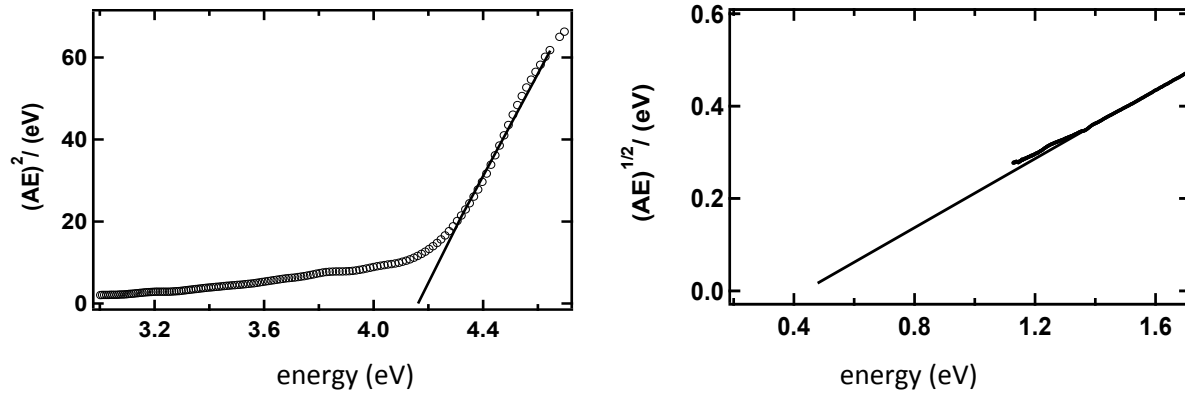


Figure 5.2: Plots of $(AE_0)^{1/2}$ and $(AE_0)^2$ as a function of incident photon energy, deduced from the absorption spectrum of the dispersion prepared by dissolving solid CaS in DMSO at room temperature.

The absorption of energy by a phonon has the effect of reducing the observed onset of light absorption by an amount of $(E_{\text{phonon}} - \Delta E_{(\text{gap bulk})})$. This difference, however, ignores quantum size effects of the phonon. The dispersion of the phonon frequency (ω) is a periodic function between $-\pi/a < k < \pi/a$, where k and a are the wave vector and the unit cell length. Changes in the bond lengths and lattice parameters will result in changes in the phonon frequency and energy (E_{phonon}) that will be reflected in the indirect band gap. Indeed, changes in the lattice parameters of nanoparticles resulting from microstrain are known to cause shifts in the optical branch of several semiconductor nanoparticles.¹⁸ The optimized structure of a cube of CaS containing 4 monomer units is displayed on Figure 5.3. There are 18 vibrational modes in this cluster. The “breathing” mode of the cube is an asymmetric deformation mode that exhibits the largest displacement of the Ca^{2+} and S^{2-} ions with respect to the equilibrium positions. The largest displacements are found along the X and Y axis. Assuming that the cube is an adequate

representation of the CaS cell, one would expect this mode to have the strongest contribution to indirect band gap contributions in the CaS NP.

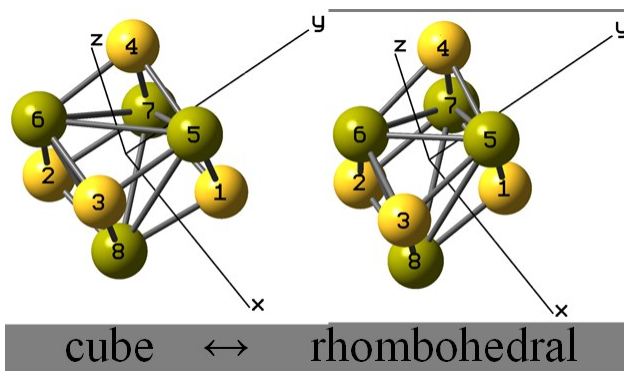


Figure 5.3: Optimized structure of a cube of CaS containing 4 monomers, with a “breathing” mode deformation.

Table 5.1 summarizes the sum of the vibrational frequencies of all the modes found in the optimized structures of several CaS nanoclusters. The sum of the vibrational frequencies increases with the number of monomer units in the cluster until it saturates between 0.516216 and 0.555329 eV. The average value of the sum of the frequencies among these clusters is 0.549397 eV. This value will reduce the band gap from 4.43 eV to 3.88 eV or 320 nm. The difference between the prediction by equations 2 and 3 with the experimental data may result from solvent effects not taken into account in our calculations or defects on the semiconductor NP, in particular, the formation of non-stoichiometric nanostructures. Solvent effect can have the effect of suppressing electronic transitions because of the change in electron density in the materials when interacting with the solvent. Defects in the materials might change the band gap because it changes the electron-hole concentration of the material, causing a shift in the valence and conduction bands.


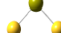



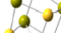
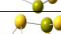
| n | sum of frequencies | |
|---|--------------------|----------|
| | nm | eV |
| 1  | 21275.38 | 0.058283 |
| 2  | 6097.748 | 0.203354 |
| 3  | 4023.358 | 0.3082 |
| 4  | 2402.096 | 0.516216 |
| 5  | 2134.153 | 0.581027 |
| 5  | 2275.168 | 0.545015 |
| 5  | 2232.911 | 0.555329 |

Table 5.1: *Sum of the vibrational frequencies of all the modes found in the optimized structures of several CaS nanoclusters with aggregate number $1 \leq n \leq 5$.*

An alternative explanation for the observed light absorption in the visible is the formation of defects in the nanostructures. Indeed, cation and anion vacancies are known to play an important role in the thermo luminescence of polycrystalline CaS.¹² Observed glow peaks have been attributed to the presence of “hole” traps as well as electron traps due to intrinsic point defects in CaS. The existence of electron traps or donors-at a depth of 0.3 eV from the bottom of the conduction band- as well as shallow hole traps or acceptors- at a depth of 1.0 eV from the top of the valence band- have been proposed to account for the observed glow curves in CaS. The average particle size is 3.2 nm. The particle size range reported here is 1.6 to 5.2 nm with a distribution of (3.2 ± 0.7) nm, where the uncertainty represents one standard deviation. It is difficult to spot point defects in a sample with the particle size range and broad particle size distribution reported here. Thus our measurements cannot allow us to distinguish the role of defects to the optical properties of the CaS nanostructures reported here.

Conclusions

The optical properties of CaS nanoparticles prepared by the reaction of $\text{Ca}(\text{CH}_3\text{CO}_2)_2$ and DMSO in a microwave have been determined by UV-Vis spectroscopy and compared with theoretical calculations. The absorption spectra of CaS prepared experimentally from this method consists of a well-defined peak in the UV and a long wavelength tail that extends above 700 nm. Emission bands centered at 500 nm with a long wavelength tail that extends above 600 nm is observed upon excitation at 405 nm. STM measurements reveal the formation of CaS nanoparticles with an average diameter of (3.2 ± 0.7) nm. Light absorption by the CaS structures is proposed to have significant contributions from indirect transitions and/or point defects. From the vibrational transitions we found that the Ca-S bond length calculated using DFT/B3LYP/DGDZVP level of theory is in closer agreement with experimental values found in the literature for gas phase CaS.

5.1 References

- (1) G. Caliendo, G. Cirino, V. Santagada, and J.L. Wallace, *J. Med. Chem.* **53**, 6275 (2010).
- (2) Y.-F. Li, C.-S. Xiao, and R.-T. Hui, *Medical Hypotheses* **73**, 445 (2009).
- (3) E. Hutter and D. Maysinger, *Microsc. Res. Tech.* **74**, 592 (2011).
- (4) U. Resch-Genger, M. Grabolle, S. Cavaliere-Jaricot, R. Nitschke, and T. Nann, *Nat. Methods* **5**, 763 (2008).
- (5) R. Freeman and I. Willner, *Chem. Soc. Rev.* **41**, 4067 (2012).
- (6) P.V. Kamat, *J. Phys. Chem. C* **112**, 18737 (2008)
- (7) R. De Angelis, M. Casalboni, F. Hatami, A. Ugur, W.T. Masselink, and P. Proposito, *Sensors and Actuators B: Chemical* **162**, 149 (2012).
- (8) P.F. Smet, I. Moreels, Z. Hens, and D. Poelman, *Materials* **3**, 2834 (2010).
- (9) W. M. Yen and M. J. Weber, *Inorganic Phosphors* (2004).
- (10) E. Ferrer, et al. *Materials Research Bulletin* **47**, 3835 (2012).
- (11) M. J. Frisch, et al. Gaussian 03 (Gaussian, Inc., Wallingford, CT, 2003)., *Gaussian 03, Revision B.03*, (n.d.).
- (12) C. Wang, K. Tang, Q. Yang, C. An, B. Hai, G. Shen, and Y. Qian, *Chemical Physics Letters* **351**, 385 (2002).
- (13) D. Rivera-Vazquez, N. Carrasco, L. Maldonado, E. Suarez, C. Poventud, C. Marrero and M. Castro. *The FASEB Journal* **28 (1)** 780.9 (2014).
- (14) C.J. Murphy and J.L. Coffey, *Applied Spectroscopy* **56**, 16 (2002).
- (15) L.E. Brus, *The Journal of Chemical Physics* **80**, 4403 (1984).
- (16) J.P. Reithmaier, *Semicond. Sci. Technol.* **23**, 123001 (2008).
- (17) J.-W. Luo, A. Franceschetti, and A. Zunger, *Phys. Rev. B* **78**, 035306 (2008).
- (18) M. Grujić-Brojčin, et al. *Acta Physica Polonica A* **116**, 51 (2009).

Chapter VI

Effect of CaS nanostructures on the proliferation rate of human adenocarcinoma cells *in vitro*

1. Introduction

Advances in the development of structured nanomaterials have a positive impact in the development of cancer treatments as well as *in vitro* detection and *in vivo* imaging.¹⁻⁴ Engineering nanostructured materials for cancer therapy requires careful consideration of nanostructure shape and dimensions, surface charge, chemical composition, shape, hydrophobicity, as well as ligand size, orientation, density and charge.⁵ These factors are important and relevant to the toxicology, specificity and clearance of the therapeutic agent in the human body. Representative nanotechnology applications for cancer diagnosis and treatment are summarized on Table 1.1. Nanotechnologies employed include: liposomes, nanoparticles, polymeric micelles, dendrimers, nanocantilevers, carbon nanotubes and quantum dots. The most common applications for these materials vary, with liposomes, dendrimers and polymeric micelles usually being employed as encapsulating agents and drug delivery vehicles, nanoparticles and quantum dots as therapeutic agents, functionalized carbon nanotubes as platforms for both therapeutic agents and drug delivery systems. Functionalized nanocantilevers have tremendous potential for single molecule detection *in vitro*.

Metastasis accounts for nearly 90 % of cancer deaths. Structures with sizes that range from a few Angstrom up to 5.5 nm are small enough to enter the smallest vasculature in healthy humans and new vasculature developed by angiogenesis and target metastatic cells that spread primary cancer tumors into the circulating system. Structures in that size range are adequate for renal clearance (threshold value of ~5.5 nm) ⁶ and can penetrate a cell membrane in the size range 2 – 8 nm. ⁷ Figure 1.4 illustrates the relative dimensions of several of the current nanotechnologies that have been subject of research in recent years. Current developments in nanotechnology that rely on functionalization to target specific cells and/or tissue results in structures with hydrodynamic radii that are too large to fulfill this size requirement. Structures in the size range of a few micrometers, like liposomes, and functionalized metal and metal oxide nanoparticles with molecular recognition capabilities, results in structures with hydrodynamic radii significantly higher than 5.5 nm. Such structures, while increasing the residence time of a target drug in the human body, can present a clearance problem by the kidneys and may have limited direct action in metastatic cells. Nanostructures that meet these small size requirements must have a chemical composition biocompatible with the human body to reduce toxicity while acting on metastatic cells. In this regard, naked CaS quantum dots have potential applications as target cell cancer and metastasis therapy agents.

CaS is a homeopathic remedy known as *Hepar sulphuris*. It is used as a remedy in alternative medicine to treat colds, coughs, sore throats, croup, abscesses, earaches, inflamed cuts and wounds, asthma, arthritis, emphysema, herpes, constipation, conjunctivitis, *Candida albicans* infections, syphilis, sinusitis, and skin infections. ⁸ However, the effect of CaS nanostructures on the growth and survival rate of cancer cells is unknown. This is surprising given the fact that it finds wide use as alternative medicine for the symptoms listed above. Compared to many

popular nanomaterials- including the noble metals and magnetic nanoparticles- calcium and sulfur based nanostructures are promising bio compatible inorganic materials. Calcium is the most abundant mineral in the human body.⁹ It plays major roles in bones, intracellular and extracellular fluid, protein structures and cell communication, among others. Sulfides, on the other hand, are present in the human body mostly in organic compounds like proteins and genetic material and it is now postulated as a novel neuromodulator/transmitter in the H₂S form.¹⁰⁻¹² Fluorescent CaS nanostructures have the potential to play an important role as cadmium-free nanostructures with applications in bioimaging,¹³⁻¹⁹ and *in vivo* labeling,²⁰⁻²² and sensing.²³⁻²⁷

The use of calcium sulfide (CaS) nanostructures and clusters with sizes smaller than 5.5 nm as target cell cancer therapy are of genuine interest due to its potential use in metastasis with light secondary effects. We report in this communication results with the use of naked CaS nanostructures on the proliferation rate of adenocarcinoma cancer cells (ATCC CRL-2124) and normal fibroblasts. The CaS nanostructures are prepared from the microwave mediated decomposition of dimethyl sulfoxide (DMSO) in the presence of calcium acetate Ca(CH₃CO₂)₂. A colored solution containing CaS nanostructures in the size range of a few Angstrom to about 5 nanometers are formed when DMSO is decomposed in the presence of Ca(CH₃CO₂)₂. The absorption spectra of the CaS is dominated by strong bands in the UV as well as absorption in the visible. We found that a single dose of CaS nanostructures does not affect the survival and growth rate of normal fibroblasts and inhibits the proliferation rate of carcinoma cells *in vitro*. CaS is predicted by theoretical calculations at the DFT/B3LYP/6-311G level of theory to interact with the thiol (R-SH), alcoholic (R-OH), amino (R-NH₂), carboxylic acid (R-COOH), ammonium (R-NH₃⁺) and carboxylate (R-COO⁻) functional groups. None of these interactions are predicted to result in the dissociation of CaS. Thermodynamic considerations are consistent

with the dissociation of CaS into Ca^{2+} ions and H_2S in acidic media, both of which are known to cause programmed cell death. Passive uptake and their pH are proposed to result in selectivity of CaS to inhibit cancer cell proliferation with no effect on normal fibroblast cells. The results encourage further research with other cell lines *in vitro* as well as with animals to advance the nanotechnology into clinical use.

2. Materials and Methods.

2.1 Synthesis of CaS clusters and nanostructures: microwave decomposition of dimethyl sulfoxide in the presence of calcium ions

CaS was prepared from (a) saturated solutions of calcium sulfide mineral, $\text{CaS}_{(s)}$, in DMSO, (b) from the reaction of sodium sulfide (Na_2S) with calcium acetate ($\text{Ca}(\text{CH}_3\text{CO}_2)_2$) in DMSO and (c) the microwave mediated decomposition of DMSO in the presence of $\text{Ca}(\text{CH}_3\text{CO}_2)_2$. The process for the synthesis of CaS nanostructures is explained in further detail in chapter III.

2.2 Characterization of CaS monomers, clusters and nanostructures

Experimental determination of the UV-Vis absorption spectroscopy measurements is performed using a PC 2000 Ocean Optics UV-Vis spectrometer. STM measurements were performed in Nanosurf Easyscan E-STM using a 0.25 mm $\text{Pt}_{0.8}\text{Ir}_{0.2}$ wire. Fluorescence spectroscopy measurements were performed in a homemade set up. The 405 nm line from a Wicked Laser E3 laser was employed as the excitation source. Emission measurements were performed in a 1 mL quartz cuvette with the Ocean Optics PC 2000 spectrometer. A research grade fiber optic was used to couple the spectrometer to the sample holder containing the cuvette. All emission measurements were performed at an angle of 90° with respect to the incident laser line.

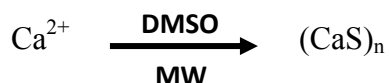
2.3 Cell culture

The carcinoma cell line used in this study (CRL-2124, atcc, USA) was a fibroblast type from a 31 year old Caucasian female. The healthy cell line used in this study (CRL-2522, atcc, USA) was a fibroblast type from a newborn male. Both cell types were adherent cell culture type. All cell culture experiments were performed in a clean room with a level 2 biosafety hazard. The feeding media used is composed of Eagle's Minimum Essential Medium (EMEM) (ATTC 30-2003), mixed with a final concentration of 10% Fetal Bovine Serum (ATCC 30-2020). The cells were grown using T-75 cell flasks incubated in a Forma Series II 3110 water jacketed CO₂ incubator (Thermo Fisher, USA) at 5% CO₂, 37 °C and 95% humidity. Microscope images were taken using an inverted microscope and recorded using a 10MP MU1000 digital camera (Amscope, Irvine, CA). Cell counting, both for sub cultivated cells and dead cells found in cell growth media, was performed using a TC-10 automated cell counter (Biorad, USA).

3. Results

3.1 STM and UV Visible absorption spectra of CaS structures.

We have shown that the molecular level heating associated with the use of microwave radiation offers the unique advantage to stop the decomposition of DMSO and turn “on” and “off” the supply of sulfide necessary for the metal-sulfide synthesis process.²⁸ The approach offers the unique advantage to stop the supply of sulfide ions at different stages of the chemical processes that result in the formation of metal sulfide precursors that participate in the nucleation and growth process. In the case of CaS, the process can be described according to the following process:



Equation 6.1

with $n = 1$ (monomers), 2, (dimers) and so on until nanoparticles are formed. Exposure of diluted solutions of Ca^{2+} ions in DMSO to microwave radiation for short periods of time (less than 70 seconds) results in the formation of CaS monomers and clusters, as revealed by the lack of absorption bands due to phonon-coupled electronic transitions from the valence to the conduction band. Microwave heating of solutions with initial Ca^{2+} to DMSO ratios larger than 10^{-3} and for longer periods of time results in the formation of CaS nanoparticles, as evidenced by the well-defined structure that results from phonon-coupled valence to conduction band electronic transitions.

Representative UV visible absorption spectra of the dispersions employed in the experiments described here are displayed on figure 6.1a. The absorption spectra of the dispersion with a 2.0×10^{-3} Ca^{2+} to DMSO mole ratio has a well defined band below 300 nm and well defined peaks at 320, 387 and 415 nm. Theoretical calculations on the optical properties of small CaS clusters predict a number of bands in the spectra of small CaS nanoclusters.²⁹ The number of bands between 250 and 400 nm is predicted to increase from 2 to 10 in going from the CaS monomer to the $(\text{CaS})_5$ cluster. The size of these clusters range from 2.7 Å for the monomer to about 1 nm for the $(\text{CaS})_8$ cluster. The absorption spectra of CaS NP obtained from the dispersion with the 2.0×10^{-3} Ca^{2+} to DMSO mole ratio, on the other hand, have a well-defined band that extends to 600 nm. This transition results from coupling phonon modes with electronic transitions from the valence to conduction band in CaS nanoparticles.^{29,30}

The absorption and emission spectra of dispersions prepared from the reaction of Na_2S and $\text{Ca}(\text{CH}_3\text{CO}_2)_2$ in DMSO and by dissolving $\text{CaS}_{(s)}$ mineral in DMSO as well as from the decomposition of DMSO in the presence of $\text{Ca}(\text{CH}_3\text{CO}_2)_2$ in a microwave are displayed on figure 6.1b. Emission spectra were obtained at an excitation wavelength of 405 nm. The

emission spectra of all these dispersions are dominated by a band between 400 and 700 nm centered at 500 nm. Absorption and emission of dispersions of CaS nanoparticles in this wavelength range has been reported independently by Wang, Jarman and Takano and co-workers.³¹⁻³³

Representative STM images of CaS nanoparticles prepared with an initial Ca^{2+} to DMSO ratio of 9.4×10^{-4} and 2.0×10^{-3} are illustrated on figure 6.1c and 6.1d, respectively. The particle size distribution with an initial Ca^{2+} to DMSO ratio of 1.4×10^{-3} is presented in figure 6.1e. The mean surface roughness increases from 130.12 pm on the clean graphite surface to 355.52 pm upon deposition of the CaS dispersion with a 3.0×10^{-4} Ca^{2+} to DMSO ratio. Islands containing the material can be distinguished in the image. The average island size is (1.8 ± 0.6) nm with a size range of 7 Angstroms to about 3 nm. The structures at the lower end of the size distribution, with diameters smaller than 1 nm, are too small to have the well defined electronic band structure found in semiconductors and are likely clusters of CaS. Well defined nanoparticles, on the other hand, are identified in the image of deposits prepared with a 2.0×10^{-3} Ca^{2+} to DMSO ratio, illustrated on figure 6.1d. The structures have an average diameter of (3.3 ± 0.7) nm and a size range of 1.8 to 5.2 nm.

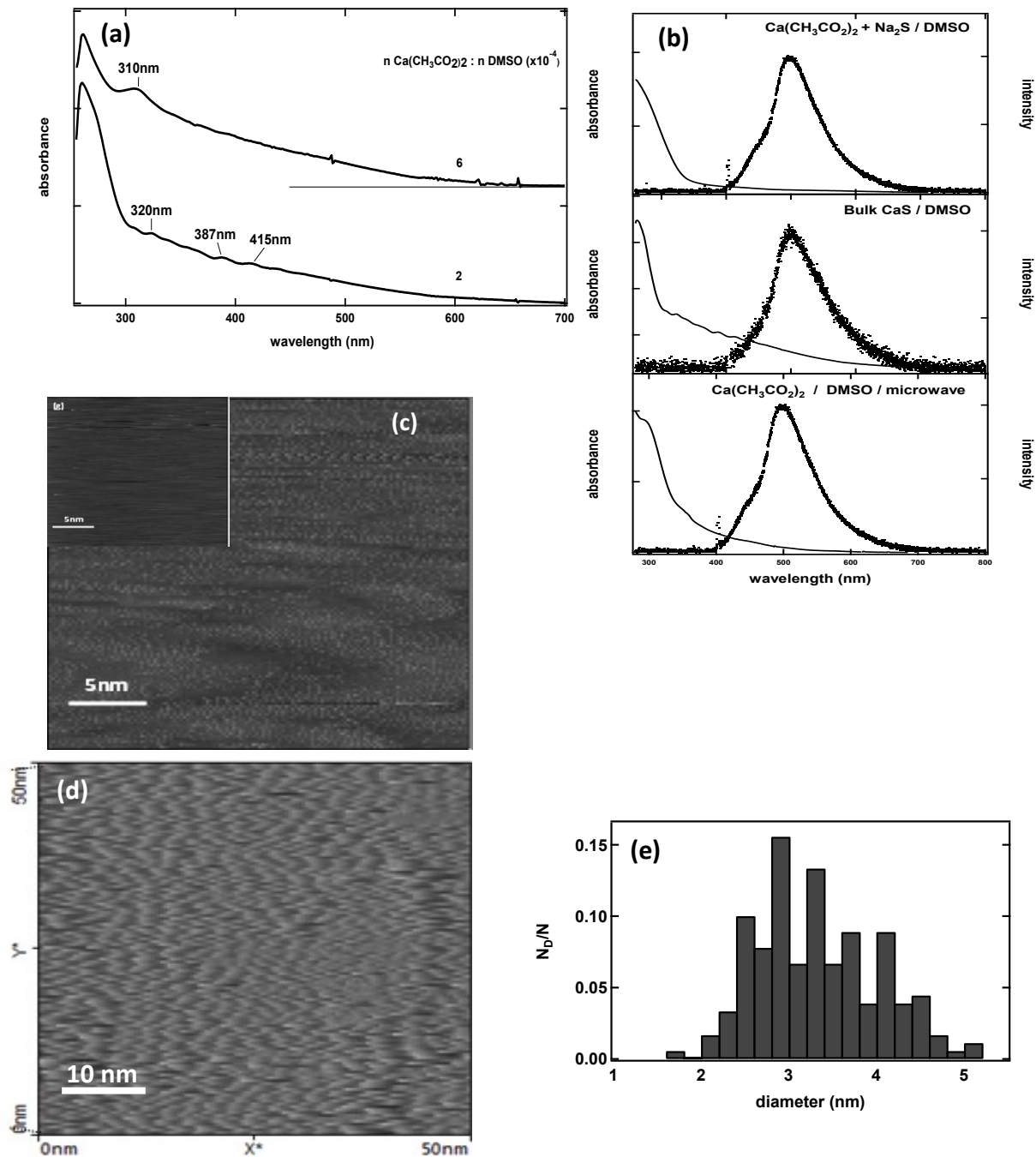


Figure 6.1: (a) UV-visible spectra of CaS nanostructures prepared from the microwave mediated decomposition of DMSO in the presence of $\text{Ca}(\text{CH}_3\text{CO}_2)_2$. The to DMSO ratios are 2 and 6×10^{-4} . (b) Absorption and emission spectra of CaS prepared from the double ion exchange reaction in DMSO (top), dissolution of bulk CaS in DMSO (middle) and microwave decomposition of $\text{Ca}(\text{CH}_3\text{CO}_2)_2$ in DMSO (bottom). Representative STM images of CaS deposits prepared from the microwave mediated decomposition of DMSO in the presence of $\text{Ca}(\text{CH}_3\text{CO}_2)_2$ with Ca^{2+} to DMSO ratios of (c) 2 and (d) 6×10^{-4} . (e) CaS particle size distribution obtained from image (d).

3.2 Effect of CaS clusters and nanoparticles in human adenocarcinoma cells.

New and emerging cutting edge technologies developed for cancer treatment requires *in-vitro* measurements for initial assesment. Two (2D) and three (3D) dimensional *in vitro* models can be used to test and examine the effectiveness and toxicology of dispersions containing nanostructures.³⁴ Two dimensional models are generally recommended for initial assesment of new materials in a biological system. Fibroblasts are adherent cells and an excellent platform to test the effect of nanostructures in cell proliferation in 2D.

Images of carcinoma cells before a single CaS NP dose reveal elongated cells a few hundred microns long. Representative images of carcinoma cells obtained 96 hours after a single calcium sulfide dose as well as those not exposed to CaS are displayed in figure 6.2. The single CaS dose was prepared by adding 200 μL of a CaS dispersion to 12 mL of the media used to feed the cell culture. This corresponds to a total calcium content of 3.8×10^{-8} moles. The effect of adding CaS to the media reveals a sharp decrease in the density of cells 96 hours after the dose as compared to those cells not exposed to CaS. Images of adenocarcinoma cells before and a few hours after a single CaS dose containing a larger calcium content (16×10^{-8}) moles obtained at a higher magnification are displayed on the bottom of the figure. There is an evident change in the morphology of the elongated fibroblasts. We can spot the appearance of blebs and protuberances in many of the cells. These changes in morphology are generally associated with apoptotic events.

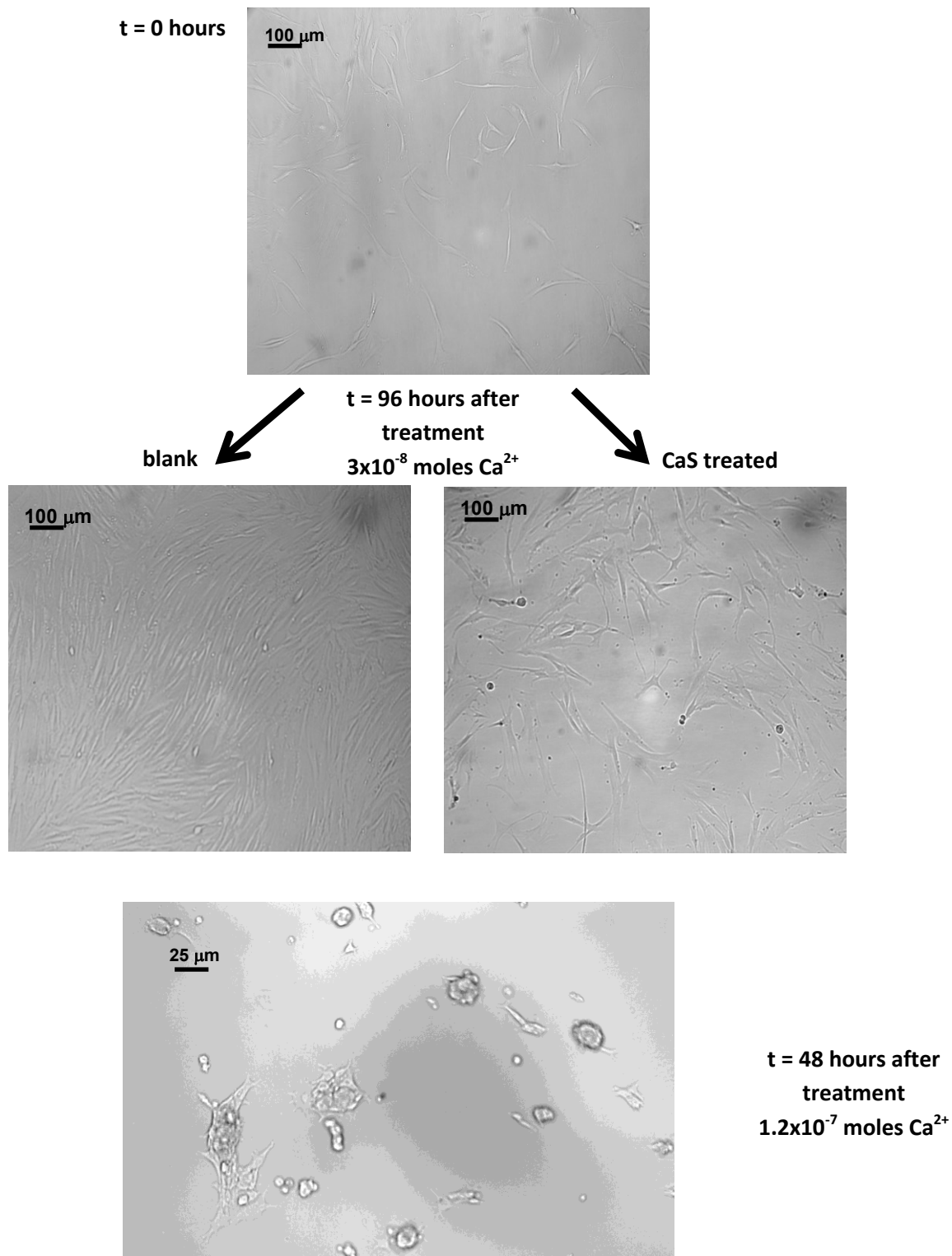


Figure 6.2: Images of adenocarcinoma cells obtained (a) 24 hours after inoculation, (b) the control 96 hours after preparing the culture and (c) 96 hours after adding a single dose of 4.0×10^{-8} moles of Ca^{2+} in the form of CaS NP. Representative image of adenocarcinoma cells 48 hours following a CaS dose of 1.6×10^{-7} moles is indicated on the bottom of the figure.

3.3 Effect of CaS clusters in human adenocarcinoma cells

We studied the effect of CaS clusters on the growth and survival rate of carcinoma cancer cell cultures. The effect of a single dose of a dispersion containing CaS on the density of carcinoma cells and normal fibroblasts as a function of time is summarized on Figure 6.3. The single CaS dose was prepared by adding 200 μL of a CaS dispersion to 12 mL of the media used to feed the cell culture. This corresponds to a total calcium content of 3.8×10^{-8} moles. The optical absorption spectrum of the CaS dispersion employed is displayed in the insert. The optical absorption spectrum is characterized by bands around 280 nm and a long wavelength tail that extends to 600 nm. The optical absorption of CaS monomers in the gas phase has transitions at 300, 500 and 1200 nm while only transitions in the UV are predicted in dispersions that use DMSO as a solvent. The CaS dose is added to the media at time $t = 0$ hours. Adenocarcinoma cells exposed to the CaS dispersion do not exhibit a significant growth with time compared to carcinoma cells not exposed to the CaS dispersion. Indeed, there is a monotonic decrease in the density of carcinoma cells exposed to CaS from 90 cells/ mm^2 to less than 80 cells/ mm^2 in the first 72 hours following the dose: the density of cells decreases at a rate of (0.10 ± 0.1) cells per mm^2 per hour. Carcinoma cells not exposed to the CaS dispersion, on the other hand, exhibit a growth from 70 cells/ mm^2 to about 120 cells/ mm^2 in the first 72 hours: the rate of increase in the cell density is (48 ± 2) cells per hour per mm^2 . We conclude that the dose of CaS reduces adenocarcinoma cell proliferation.

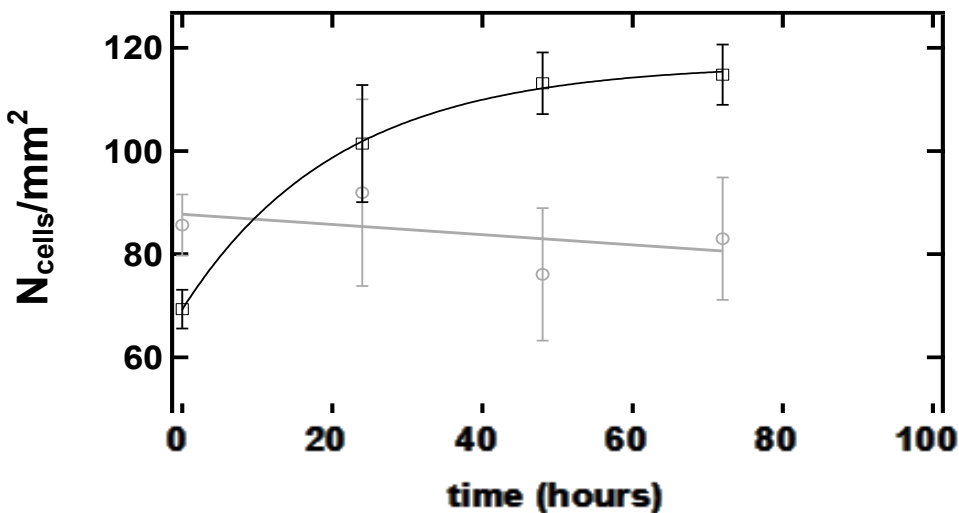


Figure 6.3: The open squares and circles represent the dependence of carcinoma cell density fed with normal media and media mixed with 4.0×10^{-8} moles of Ca^{2+} in the form of CaS monomers and clusters, respectively, on time.

3.4 Effect of CaS nanoparticles in human adenocarcinoma cells

The effect of 3 nm CaS NP on adenocarcinoma cell proliferation was studied in three different samples. The insert in figure 6.4 presents the results of measurements of adenocarcinoma cell density at different times following a single CaS NP dose. The total calcium content in the dose is 3.8×10^{-8} moles. The plots labeled S₁, S₂ and S₃ represent the average adenocarcinoma cell density on each sample at the indicated times following the dose of CaS NP in a DMSO dispersion. Results from two independent controls, labeled C₁ and C₂, are also included in the figure. One of the control samples, C₁, was fed with equal volumes of DMSO in the media as the S₁, S₂ and S₃ samples, while the other control sample, C₂, was fed with normal media. The general trend found in each flask is an increase in adenocarcinoma cell density in the first 24 hours. The density of cells starts to decrease about 48 to 72 hours

following the CaS NP dose. The density of cells in the two controls increases in this period of time. We conclude that CaS NP also reduce adenocarcinoma cell proliferation.

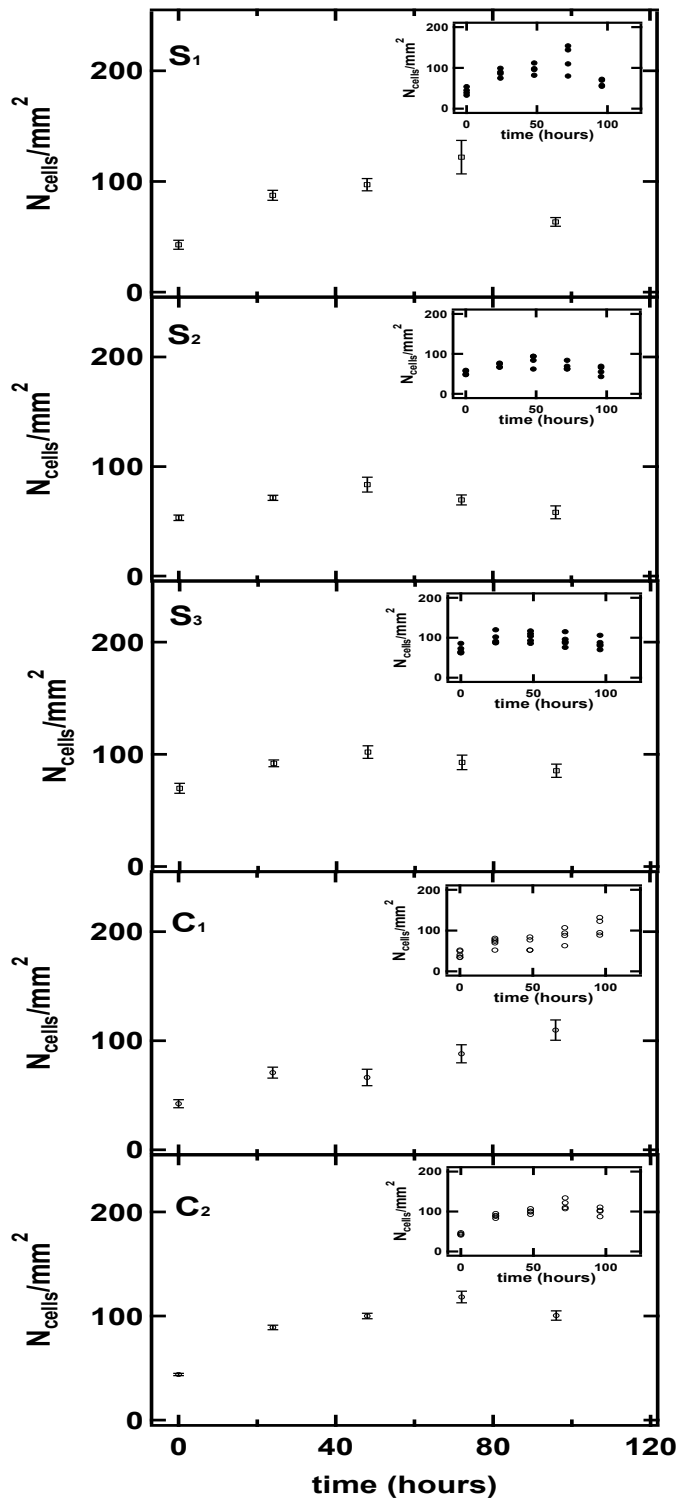


Figure 6.4: The density of adenocarcinoma cells following a single dose of 4.0×10^{-8} moles of Ca^{2+} in the form of CaS NP (S_1 , S_2 , S_3) and controls (C_1 and C_2). The error bars represent the standard deviation of the measurements. The individual measurements performed are indicated in the insert on the upper right corner of each graph.

The gray bars in the upper and lower panel of figure 6.5 summarize the effect of a single CaS NP dose on the average density of carcinoma cells and the number of dead carcinoma cells, respectively, as a function of time. The white bars in the upper and lower panel of figure 6.5 represent the average density of cells and number of dead carcinoma cells in the controls. Each reported value represents the average of the 15 independent measurements performed each day on different regions of samples S₁, S₂ and S₃. The error bars represent the standard error of the measurements.

The average density of carcinoma cells increased monotonically in the first 48 hours following the CaS NP dose. The density of cells fed with CaS in the media starts to decrease at about 48 hours following the CaS NP dose. The rate of increase of the density of cells in the first 72 hours is about (0.4 ± 0.1) (cells/mm²) per hour, slightly lower than the rate of growth of carcinoma cells in the control, which is estimated to be (0.50 ± 0.04) cells per mm² per hour in the same time range.

There is a well defined decrease in the density of cells between 48 and 72 hours following the dose. The number of dead cells in this group, on the other hand, increases from 100,000 to 150,000 to over 400,000 in the first 48, 72 and 96 hours, respectively, following the single dose of CaS. The rate of increase in the number of dead cells is $(3.8 \pm 0.8) \times 10^3$ cells/hour. The marked decrease in the density of cells and sharp increase in the number of dead cells is not observed in the carcinoma cells used as a control. We conclude that CaS NP induce cell death within 48 hours following a single dose.

The density of cells as a function of hours following a second dose of CaS NP is illustrated on the insert in figure 6.5. The gray and light colored bar represent the density cells exposed to a second dose of CaS NP and control, respectively. Both cells samples were sub cultivated from cells exposed to a single dose, as described in the previous paragraphs. Cell growth was followed for a period of 48 hour. The number of control cells increased to about 100 cells/mm² in the first 48 hours. The number of cells exposed to a second dose did not reach this cell density in this time period.

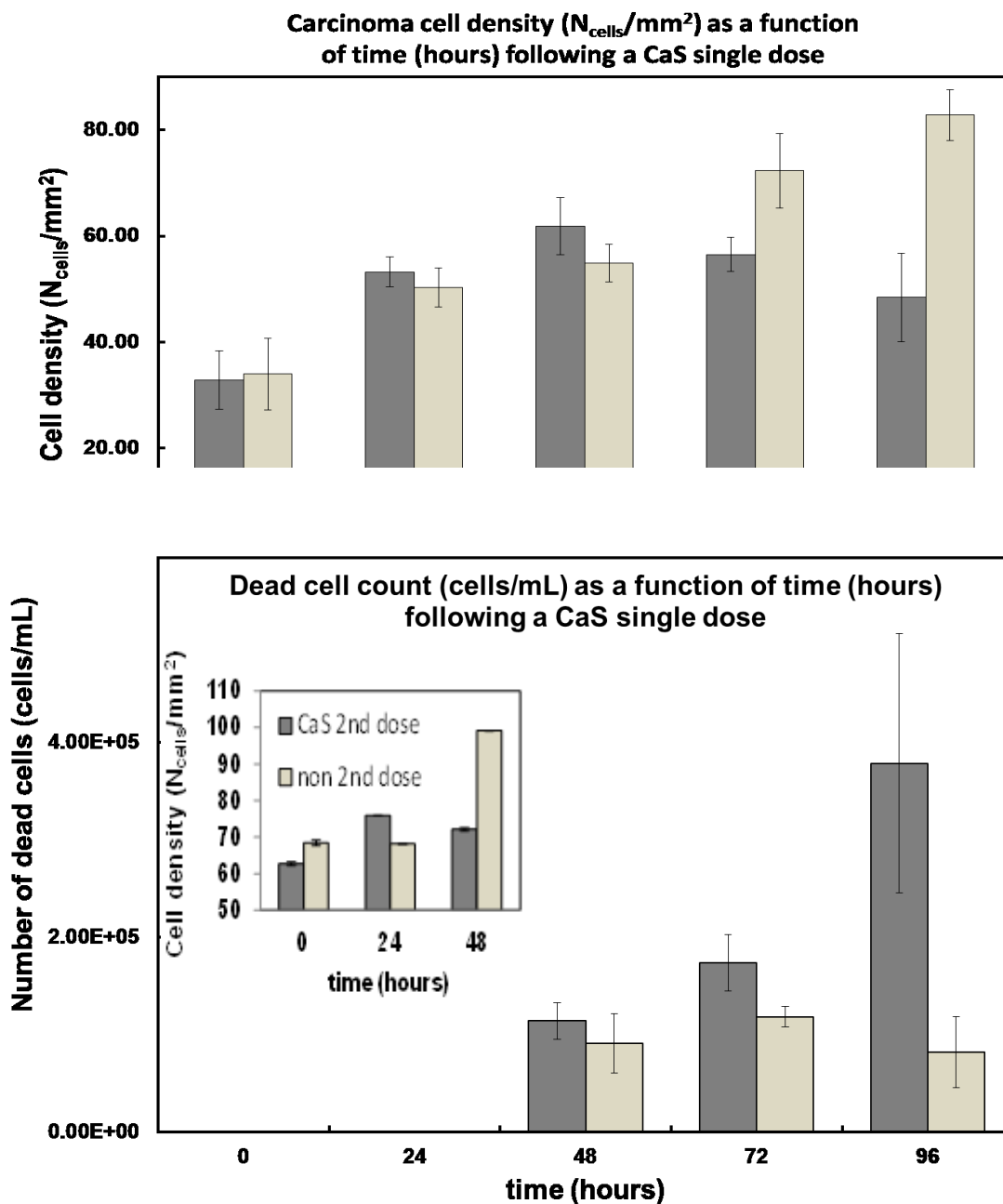


Figure 6.5: The gray bars in the upper and lower panel summarize the effect of a single dose of 3.8×10^{-8} moles of Ca^{2+} in the form of CaS NP on the density of carcinoma cells and the number of dead carcinoma cells, respectively, as a function of time. The light gray bars in the upper and lower panel represent the density of adenocarcinoma cells and number of dead carcinoma cells in cell cultures fed with media not containing the CaS nanostructures, respectively. The values reported represent the average of 15 measurements performed on different regions of three different flasks. The error bars represent the standard error of the measurements. The dark and light gray bars in the insert represent the dependence of the density of adenocarcinoma cells exposed to a second dose of 3.8×10^{-8} moles of Ca^{2+} in the form of CaS NP and exposed to one dose, respectively, on time.

3.5 Effect of CaS monomers and clusters in normal human fibroblasts

The dependence of the density of normal fibroblast exposed with to CaS clusters in the media on time is summarized on figure 6.6. The single CaS dose was prepared by adding 200 μL of a CaS dispersion to 12 mL of the media used to feed the cell culture. This corresponds to a total calcium content of the order of 10^{-8} moles. The density of normal fibroblasts exposed to media not containing the CaS dispersion is also indicated in figure 6.3b. The density of cells increases with time in both cell. Within the experimental uncertainty we cannot differentiate the rate of increase of cell density in either cell line. The density of cells increases from about 50 cells/ mm^2 to over 110 cells/ mm^2 in a 72 hour period. We conclude that CaS does not have any effect on the proliferation of normal fibroblasts.

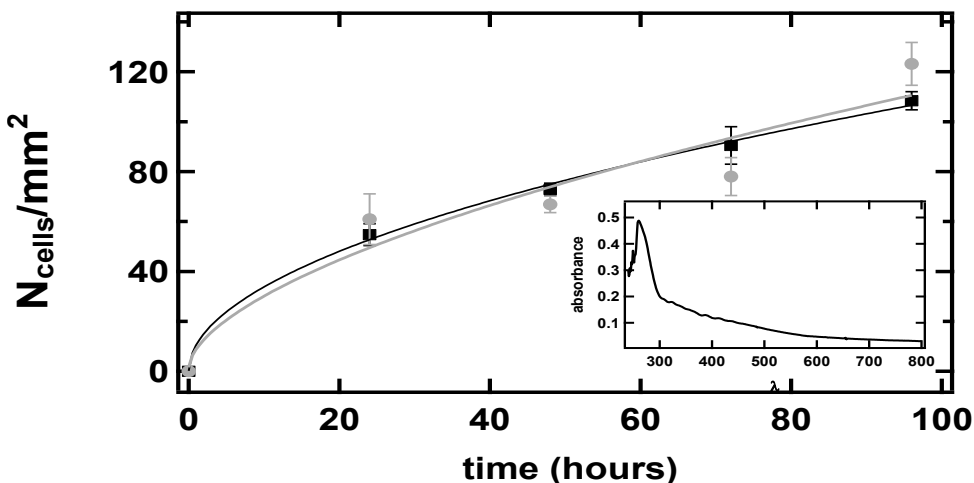
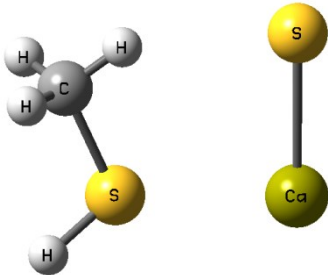
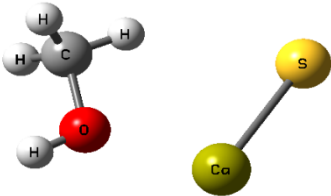
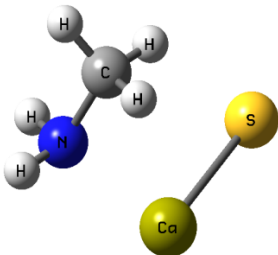


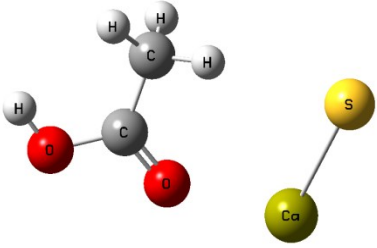
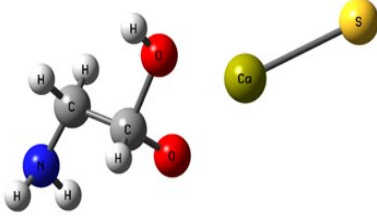
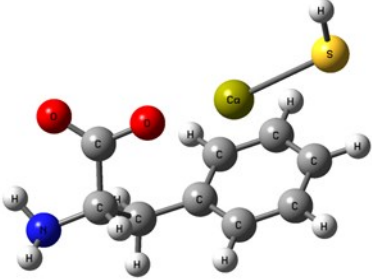
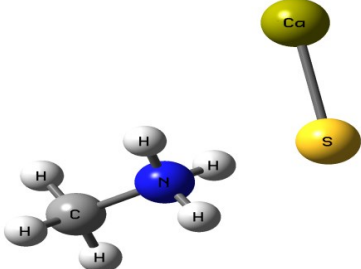
Figure 6.6: The closed squares and circles represent the dependence of normal fibroblasts cell density fed with normal media and media mixed with 4.0×10^{-8} moles of Ca^{2+} in the form of CaS monomers and clusters, respectively. The insert in the right hand side of the lower panel represents the spectrum of the dispersion containing the CaS nanostructures used for the measurements.

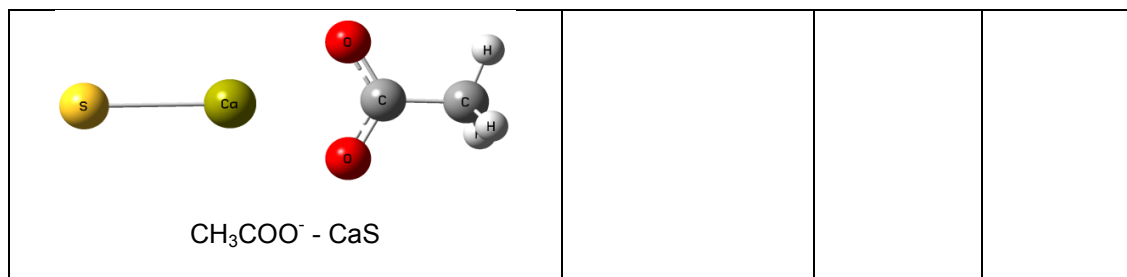
3.6. Interaction of CaS with relevant biological functional groups

We have performed theoretical calculations at the DFT/B3LYP/6-311G level of theory to learn about favorable interactions of CaS with functional groups relevant to the cell environment. We seek to identify those interactions that can result in the dissociation of CaS. The results on optimized structures are summarized on Table 6.2. None of these structures exhibited negative frequencies. The bond length of CaS is found to be 2.58 Å. This distance is short enough to consider localized interactions of CaS with relevant functional groups that may be found in macromolecules useful in the interpretation of results. The optimization process was performed by placing CaS at about 2.7 Å from a given functional group. Two calculations were performed for each functional group interacting with CaS. These calculations differed only in the initial orientation of CaS with respect to the functional group. In one calculation, CaS is oriented with the calcium end pointing toward the functional group of interest while the sulfur end points toward the functional group in the other calculation. We found that the optimized structures are independent of the initial orientation of CaS with respect to the functional group. Distances between the closest atom in the functional group and CaS are also indicated on table 6.2. These distances ranged from about 2 to 3 Å. All interactions resulted were found to be exergonic. The interaction of CaS is found to interact with the thiol (R-SH), alcoholic (R-OH) and amino (R-NH₂) functional groups by the calcium end. The oxygen atoms in the carboxylic acid functional group also exhibited a strong interaction with the calcium end of CaS. Proton transfer from the carboxylic acid group to the sulfur end was found only in phenylalanine.

Table 6.1: Optimized structures and interaction energies of CaS with several functional groups of interest in a cell. The smaller CaS to functional group minimum distance and Ca-S bond length are also indicated on the table.

| System | Interaction energy (kJ/mol) | CaS – functional group minimum distance (Å) | Ca-S bond length (Å) |
|---|-----------------------------|---|----------------------|
|  <p>CH₃SH – CaS</p> | -54.24167478 | 3.07175 | 2.59163 |
|  <p>CH₃OH – CaS</p> | -122.8815391 | 2.31069 | 2.59771 |
|  <p>CH₃NH₂ – CaS</p> | -120.4922772 | 2.47496 | 2.59496 |

| | | | |
|---|--------------|--|---------|
|  <p>CH₃COOH – CaS</p> | -133.5407041 | 2.28822 | 2.60250 |
|  <p>Glycine – CaS</p> | -415.7639143 | 2.25230 | 2.80005 |
|  <p>Phenylalanine – CaS</p> | -368.7580388 | carboxylic acid: 2.10608 aromatic ring: 3.17687 | 2.72777 |
|  <p>CH₃NH₃⁺ - CaS</p> | -199.9517525 | 3.00130 | 2.54327 |
| | -399.4134555 | 2.42681 | 2.65120 |



The relevant physiological pH is significantly higher than the pK_a of most organic carboxylic acids.³⁵ Functional groups containing NH_4^+ and COO^- are present at pH values between 6 and 7.45, which are typical values found in cancer and normal cells.⁵² The ammonium ($R-NH_3^+$) and carboxylate ($R-COO^-$) functional groups resulted in interactions with the sulfur and the calcium end of CaS, respectively. The interaction between the calcium with the carboxylate anion resulted in a lower energy and shorter distance than the interaction of the sulfur end with the ammonium functional group. None of these resulted in the dissociation of Ca-S into calcium and sulfide ions.

4. Discussion

The absorption and emission spectra of dispersions prepared from the decomposition of DMSO in the presence of $Ca(CH_3CO_2)_2$ is remarkably similar to the one obtained for dispersions prepared by dissolving $CaS_{(s)}$ mineral in DMSO or from the reaction of Na_2S and $Ca(CH_3CO_2)_2$ in DMSO. These dispersions absorb light from the UV to the visible. The observed emission is consistent with the fluorescence spectra of CaS nanoparticles obtained from the microwave mediated decomposition of other organic sulfides.²⁸

There are several models to describe cell proliferation discussed in the literature. The application of these models to specific cases depends on the complexity of the cell culture and its environment. One of the simplest mathematical models is a power law of the form:

$$N(t)/N(t=0) = At^\alpha \qquad \text{Equation 6.2}$$

Where $N(t)$ and $N(t=0)$ represent the number of cells at any time t and the initial number of cells after inoculation has been completed, respectively, In Equation 2, t is time and A and α are constants. Modeling the experimental data with a power law of the form described by equation 2 resulted in the values summarized on table 6.3. The values of α range for the adenocarcinoma and normal fibroblasts used as control in the experiments described in sections 3.4 and 3.5 fall between 0.2 and 0.5. These values are lower than the typical third power law found in tumors, likely the result of two dimensional growth, but fall within the power measured in several systems.⁵³ Significantly, the values of α found in the proliferation of adenocarcinoma and normal fibroblasts reflects an increase in cell density with time. The value of α for those adenocarcinoma cells exposed to a single dose of CaS, on the other hand, is negative and reflects a decrease in adenocarcinoma cell density. This marked difference in the proliferation of adenocarcinoma cells and normal fibroblasts lead us to conclude that CaS is cancer specific.

Table 6.2: Values of α obtained from that best fit to the experimental measurements on the proliferation of adenocarcinoma cells and normal fibroblasts according to a power model in time.

| Sample | α |
|----------------------|------------------------------|
| Carcinoma treated | -0.1 ± 0.1 |
| Carcinoma untreated | $0.2 \pm 2.6 \times 10^{-2}$ |
| Fibroblast treated | 0.5 ± 0.2 |
| Fibroblast untreated | 0.3 ± 0.1 |

Development of cancer specific chemotherapies has been the subject of basic and applied research for years. Major limitations in the application of nanotechnologies as targeted cell cancer and metastatic therapy include toxicology,³⁷⁻³⁹ lack of biodegradability,⁴⁰⁻⁴³ and size to facilitate access to the –normal and newly developed due to angiogenesis - small vasculature system in humans and elimination by the body.⁴⁴⁻⁴⁸ Structures with sizes that range from a few Angstroms up to 5 nm are small enough to enter the smallest vasculature in healthy humans and new vasculature developed by angiogenesis. Nanotechnologies in this size range can target metastatic cells that spread primary cancer tumors into the circulating system. The results presented here are encouraging to the use of CaS nanostructures as a target cell cancer and metastasis therapy. The results presented in Figures 6.3 and 6.4 indicates that CaS nanostructures smaller than 3 nm are capable of inhibiting the proliferation of cancer cells without affecting the survival and growth rate of normal cells and encourage further research *in*

in vivo. We hypothesize that the release of calcium and sulfide ions from CaS is favored in the acidic environment found in cancer cells as oppose to the basic media in normal cells. This is further supported by thermodynamic considerations discussed below.

Many apoptotic chemical processes are dependent on Ca^{2+} ion and H_2S concentration.^{49,50} We hypothesize that CaS releases Ca^{2+} and H_2S in cancer cells, but not in benign cells. In this regard, it is of interest to discuss possible pathways to release calcium from CaS. The Gibbs free energy of formation, ΔG_f , of $\text{H}_2\text{S}_{(aq)}$, $\text{S}^{2-}_{(aq)}$, $\text{Ca}^{2+}_{(aq)}$ and $\text{H}^+_{(aq)}$ and $\text{CaS}_{(s)}$, is summarized on Table 6.4. Gibbs free energies of formation were obtained from the literature.⁵¹ Using these values, we estimate that the dissolution of solid CaS(s) in water:



is an endergonic reaction with a Gibbs free energy (ΔG_{rxn}) = 9.62 kJ/mol and is not a spontaneous process.

Table 6.3: Standard Gibbs energy (ΔG_f°) of formation of probable species containing calcium and sulfide in aqueous solution.

| Species | ΔG_f° (kJ/mol) |
|----------------------|-----------------------------|
| Ca^{2+} | -553.58 |
| S^{2-} | 85.8 |
| H^+ | 0 |
| CaS | -477.4 |
| H_2S | -33.6 |

| | |
|--|-----------------------|
| Thermodynamics in water: | ΔG_f (kJ/mol) |
| $\text{CaS}_{(aq)} \rightarrow \text{Ca}^{2+}_{(aq)} + \text{S}^{2-}_{(aq)}$ | 9.62 |
| $\text{CaS}_{(s)} + 2\text{H}^+_{(aq)} \rightarrow \text{Ca}^{2+}_{(aq)} + \text{H}_2\text{S}_{(g)}$ | -109.74 |

The pH of normal and tumor cells depends on the tissue from where the sample is taken. The pH of normal cells is slightly basic and ranges from 7.35 to about 7.8.⁵² The pKa of H_2S and

HS⁻ are 7.04 and 11.96, respectively.⁵¹ Thus for pH values found in cancer cells, in the range of 6.2 to 7, we expect sulfide to exist predominantly as H₂S while for pH values between 7 and 11.96 we expect HS⁻ to be the dominant sulfide containing species. The reaction:



is exergonic with a ΔG_{rxn} of -109.7 kJ/mole and an equilibrium constant of the order of 10^{17} . The sign and magnitude of ΔG_{rxn} for this reaction indicates that the formation of free calcium ions and hydrogen sulfide from CaS is a spontaneous process that releases a significant amount of energy in acidic media. Thus the formation of Ca²⁺ and H₂S is both thermodynamically favored and consistent with the pH found in cancer cells.

Biochemical processes involving sulfides and calcium may account for the programmed cell death observed here. They can work independently or, together by different mechanisms. The investigation of cellular and molecular mechanisms underline physiological roles of calcium and sulfide ions dependent self-signaling has been clearly demonstrated in many cell types, including neurons, cardiomyocytes and endothelial cells that is associated with relevant biological processes such as cardiac contraction, inflammation, sensory transduction and angiogenesis. The most striking feature of this relationship is the ability of sulfide of either inhibiting or activating Ca²⁺ entry depending on the molecular nature of the Ca²⁺ entry pathway.⁵³⁻⁵⁵ In particular, we note that patients treated with calcium channel blockers hypertensive drugs are found to have higher risk of developing cancer.⁵⁷ Further speculation is unwarranted until experiments directed to establish the cellular chemistry of CaS nanostructures are performed.

6.1 References

- (1) Wang, R.; Billone, P. S.; Mullett, W. M. Nanomedicine in Action: An Overview of Cancer Nanomedicine on the Market and in Clinical Trials. *Journal of Nanomaterials* **2013**, *2013*, e629681.
- (2) Shapira, A.; Livney, Y. D.; Broxterman, H. J.; Assaraf, Y. G. Nanomedicine for Targeted Cancer Therapy: Towards the Overcoming of Drug Resistance. *Drug Resistance Updates* **2011**, *14*, 150–163.
- (3) Parhi, P.; Mohanty, C.; Sahoo, S. K. Nanotechnology-Based Combinational Drug Delivery: An Emerging Approach for Cancer Therapy. *Drug Discovery Today* **2012**, *17*, 1044–1052.
- (4) Hu, C.-M. J.; Aryal, S.; Zhang, L. Nanoparticle-Assisted Combination Therapies for Effective Cancer Treatment. *TherDeliv* **2010**, *1*, 323–334.
- (5) Bertrand, N.; Wu, J.; Xu, X.; Kamaly, N.; Farokhzad, O. C. Cancer Nanotechnology: The Impact of Passive and Active Targeting in the Era of Modern Cancer Biology. *Advanced Drug Delivery Reviews* **2014**, *66*, 2–25.
- (6) Choi, H. S.; Liu, W.; Misra, P.; Tanaka, E.; Zimmer, J. P.; Ipe, B. I.; Bawendi, M. G.; Frangioni, J. V. Renal Clearance of Nanoparticles. *Nat Biotechnol* **2007**, *25*, 1165–1170.
- (7) Van Lehn, R. C.; Atukorale, P. U.; Carney, R. P.; Yang, Y.-S.; Stellacci, F.; Irvine, D. J.; Alexander-Katz, A. Effect of Particle Diameter and Surface Composition on the Spontaneous Fusion of Monolayer-Protected Gold Nanoparticles with Lipid Bilayers. *NanoLett.* **2013**, *13*, 4060–4067.
- (8) Li YF, Xiao CS, Hui RT. Calcium sulfide (CaS), a donor of hydrogen sulfide (H₂S): a new antihypertensive drug? *Med Hypotheses*. 2009 Sep;73(3):445-7.
- (9) Calcium — QuickFacts <http://ods.od.nih.gov/factsheets/Calcium-QuickFacts/> (accessed Oct 10, 2013).
- (10) Shin, S.I., Masuda, H., Naohide, K. Bactericidal activity of wasabi (*Wasabia japonica*) against *Helicobacter pylori*. *International Journal of Food Microbiology*. Aug **2004**, *49* (3), 255.
- (11) Kashfi K, Olson KR. Biology and therapeutic potential of hydrogen sulfide and hydrogen sulfide-releasing chimeras. *Biochem Pharmacol*. 2013 Mar 1;85(5):689-703.
- (12) Szabó, C., Hydrogen sulphide and its therapeutic potential. *Nature Reviews Drug Discovery*. Nov **2007**, *6*, 917-35.
- (13) Arya, H.; Kaul, Z.; Wadhwa, R.; Taira, K.; Hirano, T.; Kaul, S. C. Quantum Dots in Bioimaging: Revolution by the Small. *Biochem.Biophys. Res. Commun.* **2005**, *329*, 1173–1177.
- (14) Hutter, E.; Maysinger, D. Gold Nanoparticles and Quantum Dots for Bioimaging. *Microsc. Res. Tech.* **2011**, *74*, 592–604.
- (15) Hutter, E.; Maysinger, D. Gold-nanoparticle-based Biosensors for Detection of Enzyme Activity. *Trends Pharmacol. Sci.* **2013**, *34*, 497–507.
- (16) Zrazhevskiy, P.; Sena, M.; Gao, X. Designing Multifunctional Quantum Dots for Bioimaging, Detection, and Drug Delivery. *ChemSoc Rev* **2010**, *39*, 4326–4354.
- (17) Zrazhevskiy, P.; Gao, X. Quantum Dot Imaging Platform for Single-cell Molecular Profiling. *Nat Commun* **2013**, *4*, 1619.
- (18) Zhang, Y.; Kaji, N.; Tokeshi, M.; Baba, Y. Nanobiotechnology: Quantum Dots in Bioimaging. *Expert Rev Proteomics* **2007**, *4*, 565–572.

- (19) Martínez Maestro, L.; Jacinto, C.; Rocha, U.; Carmen Iglesias-de la Cruz, M.; Sanz-Rodríguez, F.; Juarranz, A.; García Solé, J.; Jaque, D. Optimum Quantum Dot Size for Highly Efficient Fluorescence Bioimaging. *Journal of Applied Physics* **2012**, *111*, 023513.
- (20) Kirchner, C.; Liedl, T.; Kudera, S.; Pellegrino, T.; Muñoz Javier, A.; Gaub, H. E.; Stölzle, S.; Fertig, N.; Parak, W. J. Cytotoxicity of Colloidal CdSe and CdSe/ZnS Nanoparticles. *NanoLett.* **2005**, *5*, 331–338.
- (21) Resch-Genger, U.; Grabolle, M.; Cavaliere-Jaricot, S.; Nitschke, R.; Nann, T. Quantum Dots Versus Organic Dyes as Fluorescent Labels. *Nat. Methods* **2008**, *5*, 763–775.
- (22) Giraud, G.; Schulze, H.; Bachmann, T. T.; Campbell, C. J.; Mount, A. R.; Ghazal, P.; Khondoker, M. R.; Ross, A. J.; Ember, S. W. J.; Ciani, I.; et al. Fluorescence Lifetime Imaging of Quantum Dot Labeled DNA Microarrays. *International Journal of Molecular Sciences* **2009**, *10*, 1930–1941.
- (23) Tang, J.; Kemp, K. W.; Hoogland, S.; Jeong, K. S.; Liu, H.; Levina, L.; Furukawa, M.; Wang, X.; Debnath, R.; Cha, D.; et al. Colloidal-quantum-dot Photovoltaics Using Atomic-ligand Passivation. *Nat Mater* **2011**, *10*, 765–771.
- (24) Williams, G.; Kamat, P. V. Graphene–Semiconductor Nanocomposites: Excited-State Interactions Between ZnO Nanoparticles and Graphene Oxide †. *Langmuir* **2009**, *25*, 13869–13873.
- (25) Rizvi, S. B.; Yildirimer, L.; Ghaderi, S.; Ramesh, B.; Seifalian, A. M.; Keshtgar, M. A Novel POSS-coated Quantum Dot for Biological Application. *Int J Nanomedicine* **2012**, *7*, 3915–3927.
- (26) Ghaderi, S.; Ramesh, B.; Seifalian, A. M. Synthesis of Mercaptosuccinic acid/MercaptoPolyhedral Oligomeric Silsesquioxane Coated Cadmium Telluride Quantum Dots in Cell Labeling Applications. *J Nanosci Nanotechnol* **2012**, *12*, 4928–4935.
- (27) Ghaderi, S.; Ramesh, B.; Seifalian, A. M. Fluorescence Nanoparticles “Quantum Dots” as Drug Delivery System and Their Toxicity: a Review. *J Drug Target* **2011**, *19*, 475–486.
- (28) E. Ferrer, S. Nater, D. Rivera, J.M. Colon, F. Zayas, M. Gonzalez, et al., Turning “on” and “off” nucleation and growth: Microwave assisted synthesis of CdS clusters and nanoparticles, *Materials Research Bulletin*. *47* **2012** 3835–3843. doi:10.1016/j.materresbull.2011.02.019.
- (29) Rivera-Vazquez, D.; Santiago-Rodríguez, Y.; González, M.A.; Castro, M.E. Quantum Confinement Effects in Calcium Sulfide: The Role of Indirect Transitions in the Red Shift of the Band Edge in Semiconductor Nanoparticles. MRS proceedings Spring **2014**. [*in press*, doi: <http://dx.doi.org/10.1557/opl.2014.891>]
- (30) León-Velazquez, M.S.; Irizarry, R.; Castro-Rosario, M.E. Nucleation and Growth of Silver Sulfide Nanoparticles. *J. Phys. Chem. C* **2010**, *114(13)*, pp. 5839-5849
- (31) S. Takano, S. Yamamoto, S. Saito, Millimeter wave spectra of MgS and CaS, *Chemical Physics Letters*. *159* **1989**, 563–566. doi:10.1016/0009-2614(89)87533-5.
- (32) C.N. Jarman, R.A. Hailey, P.F. Bernath, A laser study of the blue electronic transitions of CaS, *The Journal of Chemical Physics*. *96* **1992**, 5571. doi:doi:10.1063/1.462698.
- (33) C. Wang, K. Tang, Q. Yang, C. An, B. Hai, G. Shen, et al., Blue-light emission of nanocrystalline CaS and SrS synthesized via a solvothermal route, *Chemical Physics Letters*. *351* **2002**, 385–390. doi:10.1016/S0009-2614(01)01413-0.
- (34) Rizvi, S. B.; Ghaderi, S.; Keshtgar, M.; Seifalian, A. M.; Muhammed, M. Semiconductor Quantum Dots as Fluorescent Probes for *in Vitro* and *in Vivo* Bio-Molecular and Cellular Imaging. *Nano Reviews* **2010**, *1*.

- (35) Lundblad, R.L. and MacDonald, F.M. Handbook of biochemistry and molecular biology. **2010**. 4th edition. CRC Press.
- (36) Griffiths, J.R. Are Cancer Cells Acidic? *Br. J. Cancer* **1991**, *64*, 425-427.
- (37) Ye, L.; Yong, K.-T.; Liu, L.; Roy, I.; Hu, R.; Zhu, J.; Cai, H.; Law, W.-C.; Liu, J.; Wang, K.; et al. A Pilot Study in Non-human Primates Shows No Adverse Response to Intravenous Injection of Quantum Dots. *Nature Nanotechnology* **2012**, *7*, 453–458.
- (38) Valizadeh, A.; Mikaeili, H.; Samiei, M.; Farkhani, S. M.; Zarghami, N.; Kouhi, M.; Akbarzadeh, A.; Davaran, S. Quantum Dots: Synthesis, Bioapplications, and Toxicity. *Nanoscale Res Lett* **2012**, *7*, 1–14.
- (39) Hardman, R. A Toxicologic Review of Quantum Dots: Toxicity Depends on Physicochemical and Environmental Factors. *Environ. Health Perspect.* **2006**, *114*, 165–172.
- (40) Roberts, J. R.; Antonini, J. M.; Porter, D. W.; Chapman, R. S.; Scabilloni, J. F.; Young, S.-H.; Schwegler-Berry, D.; Castranova, V.; Mercer, R. R. Lung Toxicity and Biodistribution of Cd/Se-ZnS Quantum Dots with Different Surface Functional Groups after Pulmonary Exposure in Rats. *Particle and Fibre Toxicology* **2013**, *10*, 5.
- (41) Kümmerer, K.; Menz, J.; Schubert, T.; Thielemans, W. Biodegradability of Organic Nanoparticles in the Aqueous Environment. *Chemosphere* **2011**, *82*, 1387–1392.
- (42) Chuev, M.; Cherepanov, V.; Nikitin, M. P.; Polikarpov, M. Biodegradation of Nanoparticles in a Body from Mössbauer and Magnetization Measurements. *Solid State Phenomena* **2012**, *190*, 725–728.
- (43) Chan, W.; Shiao, N. Cytotoxic Effect of CdSe Quantum Dots on Mouse Embryonic Development. *Acta Pharmacol Sin* **2008**, *29*, 259–266.
- (44) Choi, H. S.; Liu, W.; Misra, P.; Tanaka, E.; Zimmer, J. P.; Ipe, B. I.; Bawendi, M. G.; Frangioni, J. V. Renal Clearance of Nanoparticles. *Nat Biotechnol* **2007**, *25*, 1165–1170.
- (45) Li, S.-D.; Huang, L. Pharmacokinetics and Biodistribution of Nanoparticles. *Mol. Pharm.* **2008**, *5*, 496–504.
- (46) Ruiz, A.; Hernández, Y.; Cabal, C.; González, E.; Veintemillas-Verdaguer, S.; Martínez, E.; Morales, M. P. Biodistribution and Pharmacokinetics of Uniform Magnetite Nanoparticles Chemically Modified with Polyethylene Glycol. *Nanoscale* **2013**.
- (47) Yang, Z.; Leon, J.; Martin, M.; Harder, J. W.; Zhang, R.; Liang, D.; Lu, W.; Tian, M.; Gelovani, J. G.; Qiao, A.; et al. Pharmacokinetics and Biodistribution of Near-infrared Fluorescence Polymeric Nanoparticles. *Nanotechnology* **2009**, *20*, 165101.
- (48) Arvizo, R. R.; Miranda, O. R.; Moyano, D. F.; Walden, C. A.; Giri, K.; Bhattacharya, R.; Robertson, J. D.; Rotello, V. M.; Reid, J. M.; Mukherjee, P. Modulating Pharmacokinetics, Tumor Uptake and Biodistribution by Engineered Nanoparticles. *PLoS ONE* **2011**, *6*, e24374.
- (49) Mattson, M.P.; Chan, S.L. Calcium Orchestrates Apoptosis. *Nature Cell Biology*, **2003**, *5*, 1041-1043.
- (50) Pörn-Ares MI, Ares MP, Orrenius S. Calcium signalling and the regulation of apoptosis. *Toxicol In Vitro*. **1998** Oct;12(5):539-43. PubMed PMID: 20654437.
- (51) Wagman, D.D., et al. The NBS Tables of Chemical Thermodynamic Properties. **1982**, 11.
- (52) Gerweck, L.E. and Setharman. Cellular Ph Gradient in Tumor vs. Normal Tissue: Potential Exploitation for the Treatment of Cancer. *Cancer Res.* **1996**, *56*, 1194-1198.
- (53) Laird, A.K. Dynamics of Tumor Growth. Argonne National Laboratory, June, **1964**.

- (54) Li YF, Xiao CS, Hui RT. Calcium sulfide (CaS), a donor of hydrogen sulfide (H₂S): a new antihypertensive drug? *Med Hypotheses*. **2009** Sep;73(3):445-7. doi: 10.1016/j.mehy.2009.03.030. Epub 2009 Apr 28. PubMed PMID: 19403240.
- (55) Chen CH, Su SJ, Chang KL, Huang MW, Kuo SY. The garlic ingredient diallyl sulfide induces Ca(2+)mobilization in Madin-Darby canine kidney cells. *Food Chem Toxicol*. 2009 Sep;47(9):2344-50. doi:10.1016/j.fct.2009.06.028. Epub 2009 Jun 22. PubMed PMID: 19555733.
- (56) Markova, J.; Hudecova, S.; Soltysova, A.; Sirova, M.; Csaderova, L.; Lencesova, L.; Ondrias, K.; Krizanova, O. Sodium/calcium Exchanger Is Upregulated by Sulfide Signaling, Forms Complex with the β 1 and β 3 but Not β 2 Adrenergic Receptors, and Induces Apoptosis. *Pflugers Arch*. **2014**, 466, 1329–1342.
- (57) Rizzuto, R.; et al. Calcium and apoptosis: facts and hypotheses. *Oncogene*. **2003**. 8619-8627.

Chapter VII

Conclusions and Outlook

There is a need for the development of greener, heavy-metal free nanostructures with applications in energy and biomedical sciences. We have worked with the development of calcium based nanostructures that have a quantum yield similar to that of heavy-metal based counterparts.

We have synthesized and characterized calcium-based nanostructures, with sizes ranging from a few Angstrom up to 5 nm. The electronic and vibrational transitions that occur in CaS nanostructures and are responsible for both the direct and indirect band gap characteristic of CaS have been studied.

We have studied the nature of the chemical bond in calcium sulfide. We found that it has significant covalent character. This is important in explaining the stability of this molecule in the DMSO solvent, but not in water. Also, we found that the process by which CaS clusters are formed is consistent up to a certain point with classical, stepwise nucleation and growth theory. We propose that there are energy wells in which small clusters form spontaneously or by coupling reactions and are stable. The CaS dimer is predicted to be an important structure in DMSO. This helps explain the nature of cluster formation and contributes to the general understanding of nucleation processes.

Finally, we studied the effects of CaS nanostructures on the proliferation rate of adenocarcinoma cells. We found that CaS inhibits the proliferation and kills cancer cells without affecting normal fibroblasts. This is an important contribution with potential applications in cancer therapy. Cancer research has been deemed a top priority by the US government. This

gives cancer research and the search for alternative therapeutic agents without toxicological side effects an imperative task for the benefit of our society.

This dissertation has provided knowledge to better understand fundamental issues in science and in our society in general, such as the processes involved at the early stages of nucleation and growth, added to the experimental body of knowledge related to the use of microwave radiation to control nucleation processes, the nature of the Ca-S bond and the possibility of a new, calcium-based therapeutic agent for breast cancer treatment. Many questions remain unanswered, such as the possibility of extending our research into other types of cancer and the use of other non-heavy metals for the synthesis of environmentally friendly sulfides. Doping and functionalization of CaS nanostructures may open the possibilities for use of CaS nanostructures as a selective biosensing material, drug delivery and energy applications.